ISTANBUL TECHNICAL UNIVERSITY ★ GRADUATE SCHOOL

IMPLEMENTATION OF PROPULSION SYSTEM INTEGRATION LOSSES TO A SUPERSONIC MILITARY AIRCRAFT CONCEPTUAL DESIGN

M.Sc. THESIS

Emre KARASELVİ

Department of Aeronautics and Astronautics Engineering

Aeronautics and Astronautics Engineering Programme

SEPTEMBER 2021

ISTANBUL TECHNICAL UNIVERSITY ★ GRADUATE SCHOOL

IMPLEMENTATION OF PROPULSION SYSTEM INTEGRATION LOSSES TO A SUPERSONIC MILITARY AIRCRAFT CONCEPTUAL DESIGN

M.Sc. THESIS

Emre KARASELVİ
511171151

Department of Aeronautics and Astronautics Engineering

Aeronautics and Astronautics Engineering Programme

Thesis Advisor: Prof. Dr. Melike NİKBAY

SEPTEMBER 2021

ISTANBUL TEKNİK ÜNİVERSİTESİ ★ LİSANSÜSTÜ EĞİTİM ENSTİTÜSÜ

İTKİ SİSTEMİ ENTEGRASYONU KAYNAKLI KAYIPLARIN SÜPERSONİK ASKERİ UÇAK KAVRAMSAL TASARIMINA UYGULANMASI

YÜKSEK LİSANS TEZİ

Emre KARASELVİ
511171151

Uçak ve Uzay Mühendisliği Ana Bilim Dalı

Uçak ve Uzay Mühendisliği Programı

Tez Danışmanı: Prof. Dr. Melike NİKBAY

EYLÜL 2021

Emre Karaselvi, a M.Sc. student of İTU Graduate School student ID 511171151 successfully defended the thesis/dissertation entitled "IMPLEMENTATION OF PROPULSION SYSTEM INTEGRATION LOSSES TO A SUPERSONIC MILITARY AIRCRAFT CONCEPTUAL DESIGN", which he prepared after fulfilling the requirements specified in the associated legislations, before the jury whose signatures are below.

Thesis Advisor : **Prof. Dr. Melike NİKBAY** ....
Istanbul Technical University

Jury Members : **Prof. Dr. Konstantinos KONTIS** ....
University of Glasgow

Doç. Dr. Ayşe Gül GÜNGÖR ....
Istanbul Technical University

Date of Submission : 19 September 2021
Date of Defense : 07 October 2021

To my family,

FOREWORD

First, I want to express my deepest thanks to my advisor, Prof. Dr. Melike Nikbay, for her continuous encouragement during my master's studies and research, for her patience, inspiration, passion, and vast knowledge. Her advice aided me throughout the research and writing stages of this thesis.

Apart from my advisor, I would like to express my gratitude to the rest of my thesis committee: Prof. Dr. Konstantinos Kontis and Assoc. Prof. Dr. Ayşe Gül Güngör for their encouragement, insightful comments, and challenging questions.

Additionally, I would like to express my gratitude to Turkish Aerospace Industries and Propulsion Integration IPT.

September 2021 Emre KARASELVİ

CONTENTS

ABBREVIATIONS

AR	**:** Aspect Ratio
BPR	**:** Bypass Ratio
FPR	**:** Fan Pressure Ratio
GE	**:** General Electrics
HPT	**:** High Pressure Turbine
LPT	**:** Low Pressure Turbine
NASA	**:** National Administration of Space
NPSS	**:** Numerical Propulsion System Simulation
OEM	**:** Original Equipment Manufacturer
OPR	**:** Overall Pressure Ratio
PLA	**:** Power Lever Angle
PW	**:** Pratt &Withney
SFC	**:** Specific Fuel Consumption
STOL	**:** Short Take Off Landing
T/W	**:** Thrust to Weight Ratio
TurAF	**:** Turkish Air Force
USAF	**:** United States Air Force
VSTOL	**:** Vertical and Short Take Off Landing

SYMBOLS

$\boldsymbol{A}$	: Area
$\boldsymbol{A_c}$	: Capture area
$\boldsymbol{c}$	: Speed of sound
$\boldsymbol{c_d}$	: Drag coefficient
$\boldsymbol{D}$	: Diameter
$\boldsymbol{F}$	: Force
$\boldsymbol{F_D}$	: Drag force
$\boldsymbol{F_G}$	: Gross thrust
$\boldsymbol{F_N}$	: Net force
γ	: Specific heat ratio
$\boldsymbol{h}$	: Enthalpy
$\boldsymbol{K}$	: Correlation factor
$\boldsymbol{M}$	: Mach
$\boldsymbol{\dot{m}}$	: Mass flow
$\boldsymbol{PqP}$	: Pressure recovery
$\boldsymbol{q}$	: Dynamic pressure
$\boldsymbol{Q}$	: Heat
$\boldsymbol{R}$	: Specific gas constant
$\boldsymbol{R_e}$	: Reynold numbers
ρ	: Density
$\boldsymbol{S}$	: Entropy
$\boldsymbol{s}$	: Engine spacing
$\boldsymbol{T}$	: Temperature
$\boldsymbol{V}$	: Volume
$\boldsymbol{\vartheta}$	: Velocity

SUBSCRIPTS

$\boldsymbol{0}$	: Total
$\boldsymbol{Add}$	: Additive Drag
$\boldsymbol{amb}$	: Ambient
$\boldsymbol{B_m}$	: Maximum base drag
$\boldsymbol{BT}$	: Boattail
$\boldsymbol{BS}$	: Base
$\boldsymbol{corr}$	: Corrected
$\boldsymbol{IN}$	: Interference
$\boldsymbol{inlet}$	: Inlet
$\boldsymbol{j}$	: Jet
$\boldsymbol{large}$	: Larger dimension
$\boldsymbol{m}$	: Maximum, knuckle
$\boldsymbol{ref}$	: Reference
$\boldsymbol{s}$	: Static
$\boldsymbol{small}$	: Smaller dimension
$\boldsymbol{spill}$	: Spillage
$\boldsymbol{std}$	: Standard
$\boldsymbol{sub}$	: Subsonic
$\boldsymbol{sup}$	: Supersonic
$\boldsymbol{t}$	: Total
$\boldsymbol{\beta}$	: Boattail
∞	: Free stream

FIGURES

Page

IMPLEMENTATION OF PROPULSION SYSTEM INTEGRATION LOSSES TO A SUPERSONIC MILITARY AIRCRAFT CONCEPTUAL DESIGN

SUMMARY

Military aircraft technologies play an essential role in ensuring combat superiority from the past to the present. That is why the air forces of many countries constantly require the development and procurement of advanced aircraft technologies. A fifth-generation fighter aircraft is expected to have significant technologies such as stealth, low-probability of radar interception, agility with supercruise performance, advanced avionics, and computer systems for command, control, and communications.

As the propulsion system is a significant component of an aircraft platform, we focus on propulsion system and airframe integration concepts, especially in addressing integration losses during the early conceptual design phase. The approach is aimed to be appropriate for multidisciplinary design optimization practices.

Aircraft with jet engines were first employed during the Second World War, and the technology made a significant change in aviation history. Jet engine aircraft, which replaced propeller aircraft, had better manoeuvrability and flight performance. However, substituting a propeller engine with a jet engine required a new design approach. At first, engineers suggested that removing the propellers could simplify the integration of the propulsion system. However, with jet engines for fighter aircraft, new problems arose due to the full integration of the propulsion system and the aircraft's fuselage. These problems can be divided into two parts: designing air inlet, air intake integration, nozzle/afterbody design, and jet interaction with the tail. The primary function of the air intake is to supply the necessary air to the engine with the least amount of loss. However, the vast flight envelope of the fighter jets complicates the air intake design. Spillage drag, boundary layer formation, bypass air drag and air intake internal performance are primary considerations for intake system integration. The design and integration of the nozzle is a challenging engineering problem with the complex structure of the afterbody and the presence of jet and free-flow mix over control surfaces. The primary considerations for the nozzle system are for afterbody integration, boat-tail drag, jet flow interaction, engine spacing for twin-engine configuration, and nozzle base drag.

Each new generation of aircraft design has become a more challenging engineering problem to meet increasing military performances and operational capabilities. This increase is due to higher Mach speeds without afterburner, increased acceleration capability, high maneuvrability, and low visibility. Tradeoff analysis of numerous intake nozzle designs should be carried out to meet all these needs. It is essential to calculate the losses caused by different intakes and nozzles at the conceptual design of aircraft. Since the changes made after the design maturation delay the design calendar or changes needed in a matured design cause high costs, it is crucial to accurately present intake and nozzle losses while constructing the conceptual design of a fighter aircraft. This design exploration process needs to be automated using numerical tools to investigate all possible alternative design solutions simultaneously and efficiently.

Therefore, spillage drag, bypass drag, boundary layer losses due to intake design, boat-tail drag, nozzle base drag, and engine spacing losses due to nozzle integration are examined within the scope of this thesis. This study is divided into four main titles. The first section, "Introduction", summarizes previous studies on this topic and

presents the classification of aircraft engines. Then the problems encountered while integrating the selected aircraft engine into the fighter aircraft are described under the “Problem Statement”. In addition, the difficulties encountered in engine integration are divided into two zones. Problem areas are examined as inlet system and afterbody system.

The second main topic, “Background on Propulsion,” provides basic information about the propulsion system. Hence, the Brayton cycle is used in aviation engines. The working principle of aircraft engines is described under the Brayton Cycle subtitle. For the design of engines, numbers are used to standardize engine zone naming to present a common understanding. That is why the engine station numbers and the regions are shown before developing the methodology. The critical parameters used in engine performance comparisons are thrust, specific thrust and specific fuel consumption, and they are mathematically described. The Aerodynamics subtitle outlines the essential mathematical formulas to understand the additional drag forces caused by propulsion system integration. During the thesis, ideal gas and isentropic flow assumptions are made for the calculations. Definition of drag encountered in aircraft and engine integration are given because accurate definitions prevent double accounting in the calculation.

Calculation results with developed algorithms and assumptions are compared with the previous studies of Boeing company in the validation subtitle. For comparison, a model is created to represent the J79 engine with NPSS. The engine’s performance on the aircraft is calculated, and given definitions and algorithms add drag forces to the model. The results are converged to Boeing’s data with a 5% error margin.

After validation, developed algorithms are tested with 5th generation fighter aircraft F-22 Raptor to see how the validated approach would yield results in the design of next-generation fighter aircraft. Engine design parameters are selected, and the model is developed according to intake, nozzle, and afterbody design of the F-22 aircraft. A model equivalent to the F-119-PW-100 turbofan engine is modelled with NPSS by using the design parameters of the engine. Additional drag forces calculated with the help of algorithms are included in the engine performance results because the model is produced uninstalled engine performance data. Thus, the net propulsive force is compared with the F-22 Raptor drag force Brandtl for 40000 ft. The results show that the F-22 can fly at an altitude of 40000 ft, with 1.6M, meeting the aircraft requirements.

In the thesis, a 2D intake assumption is modelled for losses due to inlet geometry. The effects of the intake capture area, throat area, wedge angle and duct losses on motor performance are included. However, the modelling does not include bump intake structure similar to intake of the F-35 aircraft losses due to 3D effects. CFD can model losses related to the 3D intake structure, and test results and thesis studies can be developed.

Circular nozzle, nozzle outlet area, nozzle throat area and nozzle maximum area are used for modelling. The movement of the nozzle blades is included in the model depending on the boattail angle and base area. The works of McDonald & P. Hughest are used as a reference to represent the 2D sized nozzle.

The method described in this thesis is one way of accounting for installation effects in supersonic aircraft. Additionally, the concept works for aircraft with conventional shock inlets or oblique shock inlets flying at speeds up to 2.5 Mach. The equation implementation in NPSS enables aircraft manufacturers to calculate the influence of installation effects on engine performance. The study reveals the methodology for calculating additional drag caused by an engine-aircraft integration in the conceptual design phase of next-generation fighter aircraft. In this way, the losses caused by the propulsion system can be calculated accurately by the developed approach in projects where aircraft and engine design has not yet been matured. If presented, drag definitions are not included during conceptual design cause significant change needs at the design stage where aircraft design evolves. Making changes in the evolved design can bring enormous costs or extend the design calendar.

İTKİ SİSTEMİ ENTEGRASYONU KAYNAKLI KAYIPLARIN SÜPERSONİK ASKERİ UÇAK KAVRAMSAL TASARIMINA UYGULANMASI

ÖZET

Geçmişten günümüze askeri uçaklar, muharebe üstünlüğünün sağlanmasında önemli rol oynamıştır. Bu nedenle hava kuvvetleri sürekli olarak yeni uçak teknolojilerinin geliştirilmesine önem vermektedir. İlk olarak İkinci Dünya Savaşı sırasında kullanılan jet motoru teknolojisi, havacılık tarihinde önemli bir değişiklik yaptı. Pervaneli uçakların yerini alan jet motorlu uçaklar, daha iyi manevra kabiliyetine ve uçuş performansına sahipti. Ancak pervanelerin sökülmesi ve jet motorlarının uçağın gövdesine yerleştirilmesi yeni bir tasarım yaklaşımı gerektiriyordu. İlk başta tasarımcılar, pervanelerin çıkarılmasının itki sistemi entegrasyonunu basitleştirebileceğini düşündü. Ancak jet motorlarının savaş uçakları için kullanılmasıyla birlikte, itki sisteminin uçak gövdesine tam entegrasyonu sonucu yeni sorunlar ortaya çıktı. Bu sorunlar iki kısma ayrılabilir. Hava alığı tasarımı, hava alığı entegrasyonu ile lüle/arka gövde tasarımı ve kuyruk ile jet etkileşimi ile ilgili sorunlar.

Hava alığının birincil işlevi, gerekli havayı motora en az kayıpla aktarmaktır. Ancak savaş uçaklarının geniş uçuş zarfı, hava alığı tasarımını zorlaştırır. Saçılma sürüklemesi, sınır tabaka oluşumu, baypas havası momentum kaybı ve hava alığı iç performansı, hava alığı sistemi entegrasyonu için dikkat edilmesi gereken ana başlıklardır. Lüle tasarımı ve entegrasyonu, arka gövdenin karmaşık yapısı ve kontrol yüzeyleri üzerinde jet ile serbest akış karışımının varlığı nedeniyle zorlu bir mühendislik problemidir. Arka gövde entegrasyonu için, konik kuyruk yapısı, jet akış etkileşimi, ikili motor konfigürasyonu için motor aralığı ve lüle çıkış alanı kaynaklı sürükleme, lüle/arka gövde entegrasyonu için dikkat edilmesi gereken ana başlıklardır.

Her yeni nesil uçak tasarımı, hava kuvvetlerinin artan performans ve operasyonel ihtiyaçlarını karşılamak için daha zorlayıcı yeni mühendislik çözümleri gerektirdi. Bu performans isteri artışının nedenleri, art yakıcı olmadan daha yüksek Mach sayısında uçuş, artan hızlanma kabiliyeti, manevra kabiliyeti ve düşük görünür gerekliliğidir. Tüm bu ihtiyaçları karşılamak için çok sayıda hava alığı ve lüle tasarımının getiri götürü analizi yapılmalıdır. Uçakların kavramsal tasarımında farklı hava alığı ve lüle tasarımından kaynaklanan kayıpların doğru şekilde hesaplanması önemlidir. Çünkü, tasarım olgunlaşmasından sonra yapılan değişiklikler tasarım takvimini geciktirir ya da olgun tasarımdaki değişiklik yüksek maliyetlere neden olur. Bu nedenle, savaş uçaklarının kavramsal tasarımı sırasında hava alığı ve lüle sistemi kayıplarını doğru bir şekilde hesaplamak önemlidir. Ayrıca bir çok alternatif tasarım çözümlerini görmek için bu sürecin otomatikleştirilmesi gerekir.

Bu tez, itki sisteminin askeri uçaklara entegrasyonu ile ilgili kayıpları ortaya koymaktadır. Tez çalışması dört ana başlığı ayrılmıştır. Giriş bölümü, bu konuda yapılan önceki çalışmalara yer verir. Uçak motorları ve uçak motorlarının sınıflandırılması konusunu anlatır. Uçak motorlarının sınıflandırılması ve hangi tip uçak motoru üzerine çalışılacağı bu bölümde belirlenmiştir. Yeni nesil savaş uçağı için turbofan motor kullanımı uygundur. Daha sonra seçilen uçak motorunun savaş uçağına entegrasyonu sırasında karşılaşılan sorunlar ilgili başlık altında anlatılmıştır. Motor entegrasyonunda karşılaşılan sorunlar temelde iki bölgeye ayrılmıştır. Problem bölgeleri hava alığı sistemi ve arka gövde sistemi olarak incelenmiştir.

İkinci ana başlıkta, itki sistemi hakkında temel bilgilere yer verilmiştir. Havacılıkta kullanılan motorlarda Braython çevrimi kullanılmaktadır. Uçak tasarımı sırasında bölgeleri standartize etmek için numaralar kullanılır. Bu yüzden motor istasyon numaraları ve karşılığındaki bölgeler gösterilmiştir. Tez çalışması boyunca istasyon numaralarına uygun isimlendirmeler kullanılmıştır. Motor performans karşılaştırmalarında kullanılan kritik parametreler, itki, özgül itki ve özgül yakıt tüketimi matematiksel olarak açıklanmıştır. Aerodinamik alt başlığında itki sistemi entegrasyonundan kaynaklı ek sürükleme kuvvetlerini anlamak için gerekli temel matematiksel formüller ortaya koyulmuştur. Tez boyunca hesaplamalar ideal gaz ve izentropik akış varsayımı ile yapılmıştır. Daha sonra uçak-motor entegrasyonunda karşılaşılan sürükleme tanımları verilmiştir. Bu tanımların doğru bir şekilde yapılması toplam sürüklemeyi hesaplarken iki kere hesaplamanın önüne geçer. Bu yüzden sürükleme tanımlarına detaylıca yer verilmiş ve hesaplama algoritmaları ortaya koyulmuştur.

Geliştirilen algoritma ve varsayımlara uygun yapılan hesaplar Boeing şirketinin daha önce yaptığı çalışmalar ile validasyon alt başlığında karşılaştırılmıştır. Karşılaştırma için NPSS ile J79 motorunu temsil edecek bir model oluşturulmuştur. Modele tanımları ve algoritmaları verilen sürükleme kuvvetleri eklenerek motorun uçak üstündeki performansı hesaplanmıştır. Sonuçlar Boeing'ın ortaya koyduğu verilere %5'lik hata payı ile yakınsamaktadır.

Valide edilen yaklaşımın yeni nesil savaş uçağı tasarımında nasıl sonuç verdiğini görmek için 5. Nesil savaş uçağı F-22 Raptor için uygulanmıştır. F-22 uçağının hava alığı, lüle ve arka gövde tasarımına uygun olarak parametreler seçilmiş ve geliştirilen algoritma ile sürükleme değerleri hesaplanmıştır. F-22 Raptor'un kullandığı F-119-PW-100 turbofan motorun itki seviyesine denk bir model, motorun tasarım parametrelerine uygun olarak NPSS ile modellenmiştir. Modellenen motor uçağa entegre olmadan önceki performans parametrelerini verdiği için algoritmalar yardımıyla hesaplanan ek sürükleme kuvvetleri motor performans sonuçlarına dahil edilmiştir. Böylece bulunan net itki kuvveti Brandtl'ın 40000 ft için ortaya koyduğu F-22 Raptor sürükleme kuvveti ile karşılaştırılmıştır. Sonuçlar F-22'nin 40000 ft irtifada, isterlere uygun olarak 1.6M hız ile uçabildiğini göstermektedir.

Bu tezde, hava alığı geometrisinden kaynaklanan kayıplar için 2 boyutlu bir hava alığı varsayımı modellenmiştir. Giriş alanı, hava alığı boğaz alanı, kama açısı ve hava alığı borusu kayıplarının motor performansı üzerindeki etkileri dahil edilmiştir. Ancak modelleme, F-35 uçaklarının hava alığına benzer yapıdaki 3D efektlerden kaynaklanan kayıpları içermemektedir. CFD, 3D hava alığı yapısı ile ilgili kayıpları modelleyebilir, test sonuçları ve tez çalışmaları gelecek çalışmalarda geliştirilebilir.

Modelleme için dairesel lüle, lüle çıkış alanı, lüle boğaz alanı ve lüle en büyük alanı kullanılmıştır. Lüle pallerinin hareketi, pal açısına ve lüle taban alanına bağlı olarak modele dahil edilmiştir. McDonald & P. Hughest'in çalışmaları, 2D boyutlu nozülü temsil etmek için referans olarak kullanılmıştır. Bu tezde açıklanan yöntem, süpersonik uçaklarda motor entegrasyon etkilerini hesaba katmanın bir yöntemini sunmuştur. Geliştirilen konsept, 2.5 Mach'a kadar hızlarda uçan normal şok girişleri veya eğik şok girişleri olan uçaklar için çalışır.

Ortaya koyulan çalışma yeni nesil bir savaş uçağının motor seçimininde motor-uçak kombinasyonundan kaynaklanan ek sürüklemelerin kavramsal tasarım aşamasında empirik formüllerle hesaplanmasını ortaya koyar. Bu sayede henüz uçak ve motor tasarımının dondurulmadığı projelerde bu yaklaşıma uygun olarak itki sistemi kaynaklı kayıplar doğru bir şekilde hesaplanabilir. Kavramsal tasarım sırasında dahil edilmeyen var sayımlar uçak tasarımının olgunlaştığı tasarım aşamasında büyük değişiklik ihtiyaçlarına neden olur. Olgunlaşmış tasarımda değişiklik yapmak çok büyük maliyetler çıkarabilir ya da tasarım takviminin uzamasına neden olabilir.

1. INTRODUCTION

Military aircraft manufacturers regularly research future aircraft designs to meet the increasing aircraft performance requirement of air forces. Aircraft design starts according to the demand from the customer. Customers such as TurAF decide the aircraft's characteristics, then used to assemble future aircraft requirements. The critical parameters for the aircraft and engine are fuel consumption, thrust force, and engine weight. These parameters are essential for starting aircraft design and fulfilling the requirements requested by the customer. In addition, these values should be defined and detailed at different cases throughout the flight envelope to cover flight altitudes and flight Mach numbers. These are used to build an engine performance model in NPSS that specifies the engine in critical parameters such as pressure, temperature, fuel flow, and gross thrust.

The drag force is defined as the force that opposes the aircraft's flight in the flow. The dimensions of the plane, the surface area, the interaction of the flow with the aircraft, and the flight Mach number play an essential role in forming this force (Anderson Jr., 2010). The drag force that represents the relationship between all of these parameters is expressed as

$$F_D = \ q * \ C_D * A \qquad (1.1)$$

Where A is the reference area, q is the dynamic pressure, and C_D represents the drag coefficient, which depends on the Mach number and Reynold number R_e (Munson B. R., 2013).

Aircrafts powered by turbofan engines have been in operation for a long time and are proven reliable. However, advancement in aircraft technology requires early optimizations for engine installed aircraft performance. There are two types of installation problems in modern combat aircraft: intake-related losses and nozzle/afterbody-related installation losses. New methods aim to predict propulsion characteristics in an aircraft to understand and reduce installation losses for future aircraft designs (Huenecke, 1987).

1.1. Literature Review

Fighter jets have been in service since the Second World War. Fighter aircraft have evolved continuously since that time, and modern military aircraft have arisen.

However, the experiments were not published during the years they were performed. It took several years to make it publicly available for the scientific literature.

Performance enhancement requirements for early fighter aircraft were typically straightforward. Although the aims were to enhance acceleration and speed, drag had to be considered to provide an extended range. The initial consideration for engine integration was only pressure losses at the intake and nozzle. The first examples of modern fighter jets lacked the criteria for low visibility, supersonic flight, and manoeuvrability necessary for air superiority (Sanders, 1946). Between 1945 and 1965, the thrust levels and inlet capture areas of the United States propulsion system increased to meet acceleration and maximum Mach number requirements. Expanding the fuselage boundary layer with increasing speed became more problematic, resulting in high deformation at the engine face when sucked by the inlet. Inlet characteristics are incorporated to meet the demand for efficient boundary layer management and compression of the captured airstream at the intake. Generally, there is a direct correlation between the highest Mach number and the intake system's design complexity. Some designers of single-engine jet aircraft incorporated a nose inlet, effectively encircling the propulsion stream. These installation corrections are used typically when turbine engines with afterburners and long engines. Although the nose inlet reduced forebody influences on the flow and resulted in a low diffusion rate design, it was heavier. Besides, the long duct generated a large amount of internal boundary layer.

Additionally, it depleted the aircraft's internal volume, which could have been used for fuel or payload. Another method of preventing ingestion of the inflow boundary layer was to create boundary layer diverters and side plates. The Northrop F-89C's installation was similar to the Bell XF-83, save for adding a diverter to lessen the likelihood of internal flow separation and high inlet flow distortion. The McDonnell F-101B supersonic interceptor included a side plate to avoid interaction between the inlet normal shock wave and the fuselage boundary layer, which would have been sufficiently unfavourable to spill low energy flow over the diverter into the inlet. While boundary layer diverters assisted in reducing low energy flow, they imposed significant drag and weight penalties (Schumacher & Trent, 1972). If a shock is strong enough, boundary layer build-up on the side plate can produce its own shock wave-boundary layer interaction problem. The transition from F-86D aircraft intake design to F-100D aircraft intake design indicates that a sharp cowl reduces intake dependent drag. Although the reduction in cowl lip radius was necessary for low supersonic drag, it often resulted in lip flow separation during subsonic manoeuvring flight (Cawthon & Truax, 1973).

Boeing Company introduced a method for measuring propulsion system installation losses in 1972. This method was used for preliminary studies of advanced aircraft configurations in the Fortran language. The work was divided into four volumes that detail the technique. The various volumes provide engineering descriptions of the calculation procedure, a programmer's manual, sample calculations and input data, accounting concepts and data correlations (Ball W. H., 1972). Ball's work was extended, and a final series of four volumes, co-authored with T. E. Hickcox, was published in 1978 under "Rapid Evaluation of Propulsion System Effects". The methods advanced in this study were converted into fully functioning software to uncover unusual designs by experimenting with additional alternatives during the conceptual design phase (Ball, W. H.; Hickcox, T. E., 1978). In the 1970s, work on this subject accelerated as the F-15 fighter aircraft was designed during those years and held an important place in modern aviation history.

The F-15 is a highly manoeuvrable aircraft capable of flying in subsonic to supersonic flow regimes. It also offers air superiority. NASA analyzed the static pressure coefficient distributions on the forebody, afterbody, and nozzles of a 1/12 scale F-15 propulsion model in the 1970s. NASA demonstrates the effect of nozzle power setting and horizontal tail deflection angle on the pressure coefficient distributions for the F-15 twin jet configuration (Pendergraft, 1979). These F-15 experiments were used to build a twin-engine fifth-generation F-22 aircraft capable of supersonic flight in low radar visibility. The F-22 fighter jet made its maiden flight on September 7, 1997, becoming aviation's first operational fifth-generation fighter aircraft. Even though the development of the F-22 ended in 2011, it remains the most successful aircraft in aviation history over the last 23 years (Gertler, 2013).

New concepts for superior tactical fighters are under development. Airframe configurations vary significantly due to modern technology and adapting to various operational requirements and threats. Future capabilities may include supersonic cruise efficiency combined with high transonic manoeuvrability, STOL and VSTOL capability, and battle survivability (LockheedMartin, 2020). All of these factors will have a substantial impact on the integration of aircraft propulsion.

Due to the problems described in the introduction and literature, the traditional aircraft design process is insufficient for a new fighter aircraft that requires a fully integrated propulsion system aircraft configuration. Conventional aircraft design, shown in Figure 1, optimizes systems in themselves. Therefore, optimized engine performance data at specific points are prepared in an interpolated tabular form throughout the flight envelope when checking whether aircraft performance requirements are met. Mission performance is checked according to the prepared table and tabulated aircraft aerodynamics and weights.

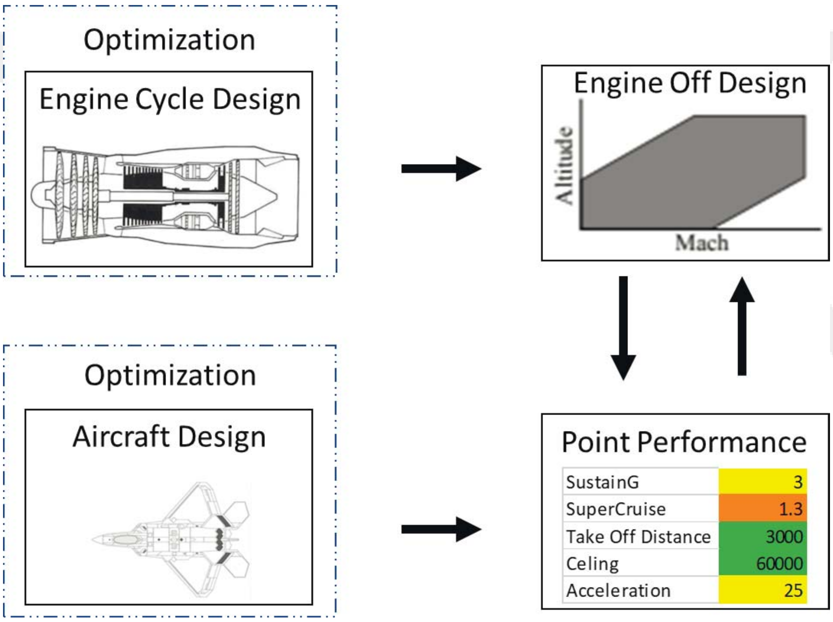

Figure 1 Traditional Engine and Aircraft Point Performance.

The aircraft systems, optimized independently, do not give the desired result when they come together; thus, the iteration continues. The engine performance results prepared throughout the flight envelope during the conceptual design phase should be computed by considering the aerodynamic and structural design to improve this process. It is used for many alternative trade-off studies, especially intake and nozzle, which affect engine performance at the early design stage. Therefore, calculating losses from intake and nozzle needs to be automated when preparing engine performance results.

The proposed optimization approach is illustrated in Figure 2. For the proposed optimization, it is necessary to accurately calculate the losses due to propulsion system integration at an early design stage. This thesis presents the necessary losses for the propulsion system-aircraft optimization together.

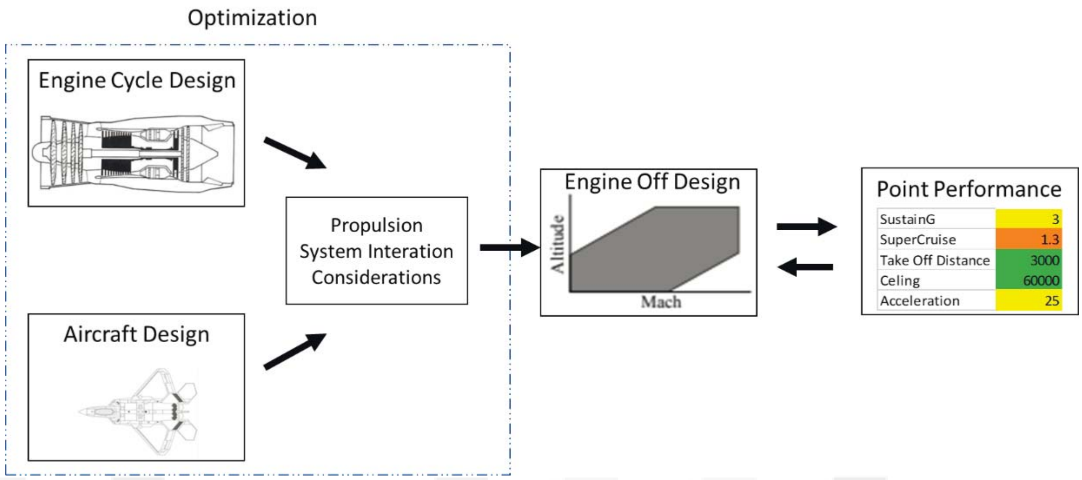

Figure 2 Proposed Engine and Aircraft Point Performance.

1.2. Aircraft Engine

Engines are critical subsystem in meeting the performance specifications of fighter jets. When comparing aero engines and choosing the best one for the aircraft's requirements, the engine's thrust/weight (T/W) ratio and specific fuel consumption (SFC) are critical parameters to consider. In addition, short takeoff distances, fast climbing speeds, supersonic flight, manoeuvrability, and low visibility become essential factors of military aircraft engine design. That is why the engine of a typical fighter aircraft is a gas turbine. However, military fighter aircraft engines are distinct from engines of passenger aircraft. To make this distinction, one must examine the engine classification system (Mattingly, Heiser, & Pratt, Aircraft engine design, 2002).

1.2.1. Classification of the aero engines

Recently, various gas turbine engines have been produced for a variety of civilian and military aircraft. When we look at these engines, we can see that the number of shafts, secondary bypass air ratio, compressor type, and hot gas use are different. As a starting point, gas turbine engines can be classified into four types: turbojet, turbofan, turboprop, and turboshaft (Huenecke, 1987). Figure 3 depicts the simple flow diagrams of these four engines.

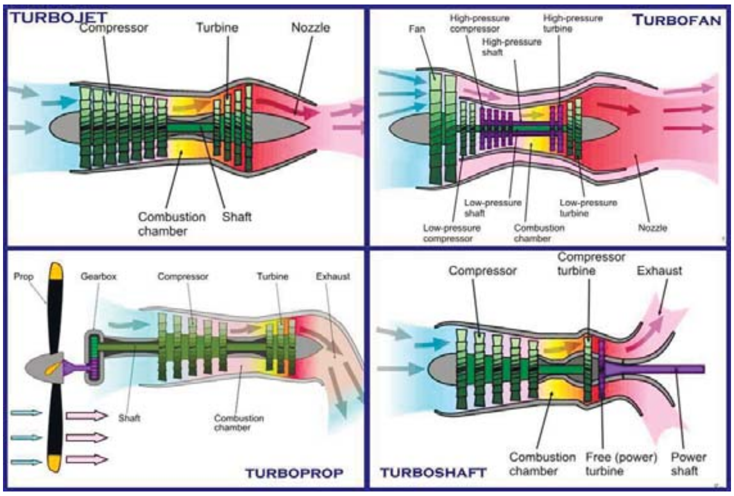

Figure 3 Classification of Engines (Kurzke, 2001)

When historical examples of fighter aircraft are examined, it is noted that turbojet and turbofan engines are often used in fighter aircraft. However, fuel savings are critical because modern fighter aircraft are attractive for their long-range operating capability. Additionally, low observability is an essential condition for fifth-generation fighter aircraft. In light of this, turbofan engines are used to power modern fighter aircraft. The bypass ratio of turbofan engines is rated (BPR). Low BPR is the reason why the thrust requirement is so high. Low fuel consumption and low observability are a product of a high BPR. The turbofan engine that will be used must meet all specifications simultaneously. Due to these conflicting conditions, it is essential to perform trade-off analyses during conceptual design.

1.3. Problem Statement

The improvement in the performance of fighter jets over time is a result of technological advancements in aerodynamics, materials science, engine technology, and a variety of other fields. Military aircraft envelopes have extended with increased performance, allowing them to fly in more than one-speed regime. Additionally, it is essential to include a design that can perform various air-land and air-air combat tasks when designing a military aircraft. Apart from these characteristics, manoeuvrability in the transonic speed regime has contributed to the preference for the supersonic cruise. As a result, it necessitated a more rigorous speed zone configuration. Modern military aircraft are supposed to be manoeuvrable, have a small turning circle, be capable of supersonic flight, and have low visibility to operate in all climatic conditions (Huenecke, 1987). As a result, significant changes in drag arise as a result of complex airflow issues. Aircraft-engine integration in this context aims to provide an interface capable of meeting high-performance requirements while posing the fewest possible problems in all flight conditions.

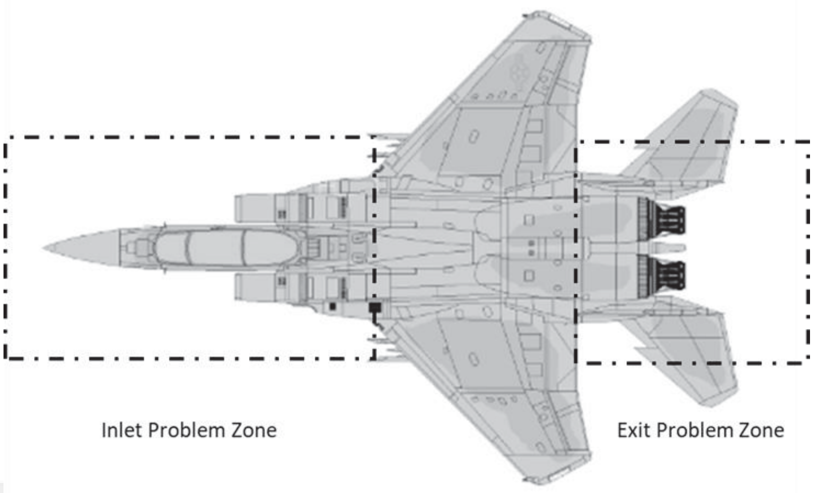

Figure 4 Installation Problem Zones for Propulsion System (Huenecke, 1987)

To meet aircraft performance design requirements, fighter aircraft uses a fully integrated propulsion system in the fuselage instead of the under-wing engine integration as commercial transport aircraft use. The issues resulting from this design can be broadly classified as intake and nozzle issues, as illustrated in Figure 4. The intake, which provides the engine with the air necessary to generate adequate thrust, is typically located near the fuselage. As a result of the front fuselage and nose configuration, the intake air is heavily influenced and is subject to turbulence in some flight envelope regions. In addition, the jet flow at the nozzle outlet interacts with the tail surfaces and afterbody configuration. The adjustment in the cross-sectional area of the nozzles during flight and the distance between two nozzles in twin-engine aircraft are the two most significant parameters influencing drag increases.

It is essential to understand all of the requirements for engine integration into the aircraft when it comes to propulsion system integration. It includes mechanical and structural contacts, the fuel system, the hydraulic system, the electrical system, and the engine starting system. However, the focus of this study is engine integration into aircraft and how intake and nozzle losses affect the engine performance. Hence, effective engine integration can result in the maximum thrust minus drag rather than the combined full thrust.

Figure 5 presents losses associated with propulsion system integration. Among the numerous drag contributions depicted in the figure, this thesis focuses on determining and implementing spillage drag, boundary layer bleed drag, boat-tail drag, and nozzle base drag because these are the leading installation losses due to propulsion system installation. This study used, Ball. M. H.'s methodologies as a baseline and in-house code is developed in Python.

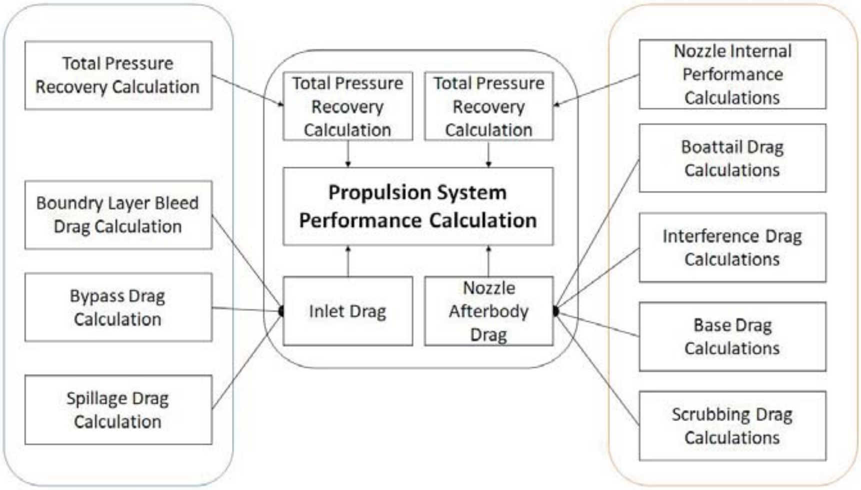

Figure 5 Drag contributions due to Propulsion System Installation

This master's thesis investigates significant installation effects at a supersonic aircraft's air intake and outlet with an integrated engine, such as the Lockheed F-22 Raptor, the Lockheed F-15 Eagle, and the Eurofighter. The study models and estimates installation effects at conceptual design and obtain installed engine performance data. This is achieved by creating and applying equations, formulas, and tables based on the assigned literature for the investigated installation effects and incorporating them into the engine output simulation method, NPSS.

1.3.1. Challenges in the inlet system integration

Typically, a fighter aircraft has one or two engines that are fully incorporated into the body. This is accomplished by using an air duct and intake system, enabling the engine to generate the required thrust. The inlet system consists of the duct and intake. The intake system of military aircraft F-16 Falcon integrated into the body is shown in Figure 6 (Huenecke, 1987). Which are the underbody or trunk sides of the vehicle are favoured in style. In contrast to F-16, Figure 6, where an underbody intake design is preferred, for F-4, Figure 7 depicts both the body and intake design.

Figure 6 Intake System for F-16 Falcon

Figure 7 Intake System for F-4 Phantom

Each intake design is unique because it is created in response to the needs of the specific fighter aircraft. Some methods have been proven to be successful through tests and flights. However, these are highly complex designs with unknowns about how they will operate in all speed modes. The intake design aims to deliver the air required to engine produce thrust while maintaining a uniform, stable flow and minimal pressure loss. However, these requirements are insufficient to meet aircraft performance conditions with a vast flight envelope and manoeuvres in the transonic speed regime.

Furthermore, during an intake design, the aircraft's requirements to take off and land on the runway should be considered. For example, the F-15 is an aircraft capable of flying at subsonic and supersonic speeds and air-to-air and air-to-land missions. This success is dependent on whether the intake design is intended to perform optimally in all flight conditions. The intake design of the F15 fighter aircraft successfully achieves take-off, landing, subsonic, supersonic, and transonic velocities.

The intake's function is to supply air to the engine to generate thrust. Therefore, the air intake's air must be of the quality and flatness that the engine accepts. The air through intake should slow down to the subsonic regime from free stream to the engine fan because the engine fan operates efficiently in the subsonic range. Additionally, the flow along the duct should be subsonic. That is why the intake flow of supersonic aircraft should be slowed to subsonic levels. The shock-slowed flow at the air intake's entrance is then diffused along the duct. As a result, the flow to the engine's inlet is further slowed. Additionally, when designing intakes, the aircraft's system requirements should be considered. Figure 8 shows the fundamental parameters used in the intake design.

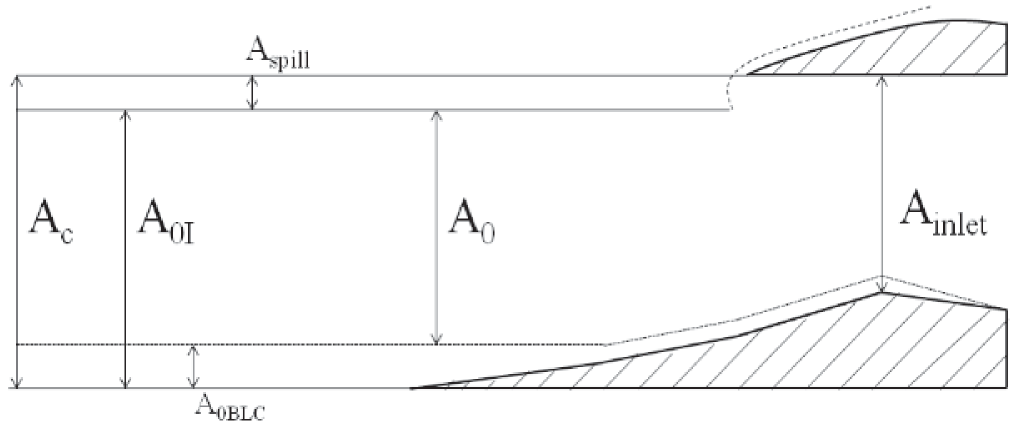

Figure 8 Intake and Related Parameters

For an oblique shock inlet, the capture area (A_c), the local stream tube area ahead of the inlet (A_0), the free-stream tube area of air entering the inlet (A_{0I}), and the aircraft throat inlet area (A_{inlet}) are all necessary. The distinction between A_{0I} and A_0 is caused by bleed air, which is defined as A_{0BLC}.

The intake system should be designed to deliver air to the engine face with the slightest total pressure loss because the more significant total pressure applied to the engine face, the greater the thrust produced by the engine. Therefore, boundary layer formation is a critical factor to consider when maintaining pressure. The boundary layer reduces the total pressure (Seddon & Goldsmith, 1999). Given these, the optimal intake design is sought; the result is a short, straight duct and a rounded-edged intake lip.

The optimal design approach used in passenger aircraft is not preferred in the design of fighter aircraft. For reasons of survivability and stealth, warplane engines are entirely integrated into the fuselage. Depending on this, a long duct design is preferable for supplying the engine with free-flow air. The crimped design of the duct satisfies stealth requirements. By rotating the free flow along the duct, the total energy of the air is reduced.

Additionally, when an over-curved structure is used to achieve stealth, flow separation occurs within the duct. This is undesired. As a result, when designing intakes, the aircraft's desires are considered.

1.3.2. Challenges in afterbody nozzle integration

When it comes to integrating nozzles, the subject is not limited to nozzles. Numerous issues arise during integration as a result of the aircraft's afterbody and tail. That is why nozzle integration is as tricky as the integration of the intake and airframe. The interaction of over plane flow and exhaust jet flow results in an unpredictable drag increase throughout the flight envelope.

Turbofans with afterburners are frequently preferred in the design of fighter aircraft. Turbofan engines have a variable cross-section area in their nozzles. That is why the exit area and the nozzle throat area vary significantly throughout the flight envelope. Changes in the nozzle's area produce a reversal of aerodynamic forces. That is why the fuselage's contour lines are less than optimal. Also, the location of the tail control surfaces is critical when implementing the engine integration. The hot jet flow from the nozzle can distort the flow in the tail and controllers, resulting in drag increases resulting from flow separations.

Additionally, the position of two engines in a twin-engine fighter aircraft becomes critical in determining how the jet flows interact. The base area of two-engine propulsion systems is quite large for twin-engine integration, making the tail's design complex. Therefore, NASA conducted in-depth studies on the F-15 fighter aircraft's nozzle integration problems. NASA's experimental study examined the effects of a two-engine fighter aircraft, afterbody separation, vertical and horizontal tail placement and interfacial effects, and boat-tail drag (Pendergraft, 1979).

While nozzle design should take high-speed flight into account, this results in a significant drag on low-speed flights. If the design is optimized for supersonic flight, the drag on the nozzle at undesirable low speeds can account for up to 30% of the total thrust (Huenecke, 1987). The increase in drag is unprompted because the same fighter design must operate in subsonic, transonic, and supersonic flight conditions and can manoeuvre flight at high speeds. Additionally, modern military aircraft are designed to move independently of the throat and exit areas to reduce drag. Due to the added weight, the mechanical system that allows for the independent movement of two areas is an undesirable solution.

Fuel savings during subsonic cruising or the speed at near the speed of sound are critical for aircraft with a longer operational radius. Thus, the design and optimization of the nozzle can be carried out at high speeds approaching the speed of sound. The most critical parameters affecting nozzle drag are the nozzle height, nozzle pressure ratio, jet velocity, and nozzle base area. The drag generated by the afterbody can be classified as base drag or boat-tail drag. Base drag equals the sum of the pressure forces acting on the aircraft's perpendicular sectional area, and moving surfaces cause boat-tail drag.

2. BACKGROUND ON PROPULSION SYSTEM

This chapter summarizes the theory applied to the project and the calculations used to achieve the results. In addition, aerodynamic fundamentals, jet engine theory, and installation configurations are discussed, as well as significant physical phenomena such as shock waves, isentropic flow, and drag.

2.1. Design of Aircraft Engines

In 1937, Hans von Ohain and Frank Whittle independently invented the first functional jet engine based on the Brayton cycle principle (Cengel & Boles, 2007). Today's jet engines are based on the same architecture but have been enhanced in efficiency and design. The two spools mixed-flow enhanced turbofan is the most frequently used engine design for supersonic aircraft in operation today. The engine's various components and processes can be classified into a variety of thermodynamic stations. The Brayton Cycle is shown in Figure 9.

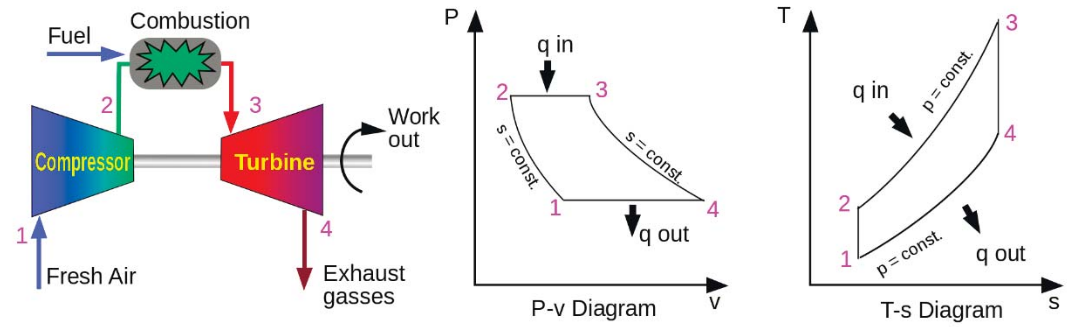

Figure 9 Ideal Brayton Cycle (Cengel & Boles, 2007)

The idealized Brayton cycle, in which P is pressure, V is volume, T is temperature, S is entropy, and Q is the amount of heat added or rejected by the system, is shown in Figure 9.

2.1.1. Aero engines and station numbering

There are several types of aero engines, but they all share nearly identical components. Figure 10 presents station numbering of low bypass turbofan engine with afterburner. The first component of a propulsion system is the intake, integrated into the aircraft's fuselage for military aircraft. The primary function of intakes is to supply the engine with the necessary air and compress it from supersonic to subsonic conditions with the minor total pressure loss possible while reducing flow distortion entering the compressor. The inlet system directs the air through the intake to the fan, which is the second part of a turbofan and is essentially a specialized compressor. The massive spinning fan suctions in copious amounts of air. Then the air is directed to the compressor, the first component in the jet engine. Compressors are composed of several bladed fans connected to a shaft. The compressor compresses the air that reaches it, increasing air pressure.

As a consequence, the potential energy of air is increased by compression. Then, compressed air is pushed into the combustion chamber. The combustor combines air and fuel and then ignites it. Fuel is sprayed into the airstream by using small nozzles with up to twenty. Then, the combination of air and fuel is ignited. It results in a high-energy, high-temperature airflow. Then the air is passed through the central engine to the afterburner or reheater, which is a highly efficient method of raising the thrust of a jet engine. Afterburners burn the remaining oxygen after the turbines shut down. Therefore, variable nozzles and other specifics are often used on engines designed for extended use with afterburners. The propelling nozzle is the final part because it transforms a gas turbine or gas generator into a jet engine. The nozzle converts the energy contained in the gas turbine exhaust into a high-speed propelling jet. In other words, the exhaust nozzle's job is to convert the remaining potential energy in the gas to kinetic energy. Acceleration of the gas is necessary for thrust generation, proportional to the exit velocity (Kurzke, 2001). The station numbering used as the industry standard is shown in the figure according to SAE ARP 755.

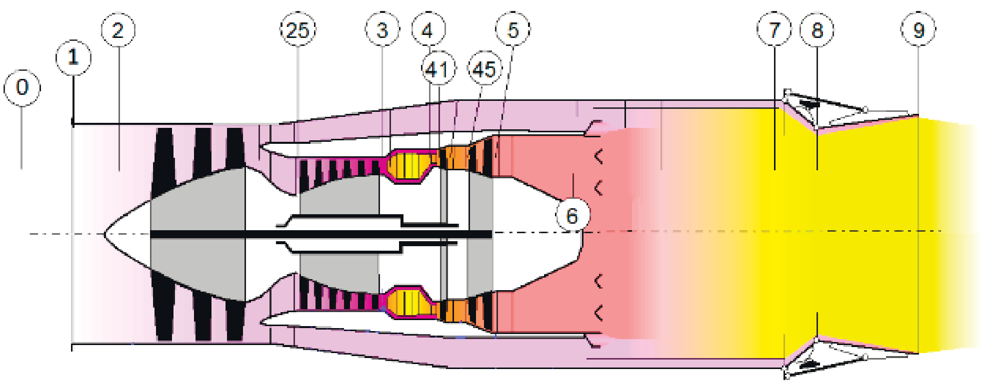

Figure 10 Station Numbering of Turbofan Engine (Kurzke, 2001)

The station numbers shown in Figure 10 are frequently used in thrust integration studies, and they are essential to provide a common use. The description of each station is shown in Figure 11.

0	Ambient
1	Aircraft-Engine Interface
2	First Compressor Inlet
25	High Pressure Compressor Inlet
3	Last Compressor Exit, Cold Side Heat Exchanger Inlet
4	Burner Exit
41	First Turbine Stator Exit
45	Low Pressure Turbine Inlet
5	Low Pressure Turbine Exit After Addition Of Cooling Air
6	Jet Pipe Inlet, Reheat Entry For Turbojet, Hot Side Heat Exchanger Inlet
7	Reheat Exit, Hot Side Heat Exchanger Exit
8	Nozzle Throat
9	Nozzle Exit

Figure 11 Station Number Definitions

2.1.2. Engine performance

Primarily three parameters determine engine performance: altitude, Mach number, and power lever angle (PLA) and additionally, numerous parameters such as the atmospheric model, the day conditions. Key engine performance parameters such as thrust, specific thrust and specific fuel consumption are presented in this section.

2.1.2.1. Thrust

Primarily three parameters determine engine performance: altitude, Mach number, and power lever angle (PLA) and additionally, numerous parameters such as the atmospheric model, the relative humidity, and the engine life decide engine efficiency. Therefore, to determine performance requirements to be satisfied by a fighter aircraft, it is necessary to know the thrust, fuel consumption, and airflow provided by altitude, Mach and PLA.

Thrust refers to the force that propels an aircraft forward. The general thrust equation is derived from Newton's second law and assumes that (Mattingly & Boyer, Elements of Propulsion: Gas Turbines and Rockets American Institute of Aeronautics and Astronautics, 2006);

$$\dot{m}_{fuel} \ll \dot{m}_{air} \quad (2.1)$$

$$F_N = \dot{m_{air}} * (V_9 - V_\infty) + A_9 * (P_{s9} - P_\infty) \quad (2.2)$$

Where $\dot{m_{air}}$ denotes the air mass flow through the engine, V_∞ denotes the air velocity, A_9 denotes the exit area, and P denotes the pressure at the specified station. Subscript ∞ represents the free stream properties, while station 9 represents the engine nozzle exit and s represents the static pressure.

Military supersonic aircraft usually employs afterburners to generate the additional thrust required under certain circumstances. Due to the high fuel consumption, afterburners are only used for short periods and supercruise capability without afterburner is favourable (Walsh & Fletcher, 2004). Engines with an afterburner must account for the additional fuel flow, which results in the reheat thrust equations (Mattingly, Heiser, & Pratt, Aircraft engine design, 2002).

$$F_N = \left(\dot{m}_{air} + \dot{m}_{fuel}\right) * V_9 - \dot{m}_{air} * V_\infty \quad (2.3)$$

Here, $\dot{m}_{air}$ denotes mass flow rate of air and $\dot{m}_{fuel}$ denotes mass flow rate of fuel. Generated thrust on a stationary testbed or aircraft is referred to as the gross thrust, which is described as

$$F_G = \left(\dot{m}_{air} + \dot{m}_{fuel}\right) * V_9 \quad (2.4)$$

The distinction between gross and net thrust is denoted by $\dot{m}_{air} * V_\infty$ which is also known as the ram drag or the inlet-momentum drag. Thus,

$$F_N = F_G - \dot{m}_{air} * V_\infty \quad (2.5)$$

Equation 2.4 ignored the drag on the outside and all losses associated with the engine's installation, which results in a ring of reduced relative velocity around the jet and a corresponding reduction in usable thrust. By tradition, the nacelle drag is considered a part of the airframe drag, and for the time being, it is disregarded. However, since the drag from the installation losses cannot be determined separately, its magnitude can cause severe disagreements between the engine and airframe manufacturers.

The engine's thrust requirements are determined by the aircraft's performance requirements, as the engine's thrust must exceed the drag forces exposed at the fuselage under specified conditions. Different engine types employ various techniques to achieve high net thrust values, which is the first term in Equation 2.3. However, turbojets have a low mass flow but maintain a high exit velocity, while turbofans have a high mass flow but a low exit velocity.

2.1.2.2. Specific thrust

The specific thrust is the thrust that is created by a gas mass flow rate of 1 kg per second (El-Sayed, 2016).

$$F_{sp} = \frac{F}{\dot{m}} \tag{2.6}$$

The primary thrust shows how the working medium is used. It is used to compare jet propulsion systems compared to one another. By simplifying assumptions such as disregarding the fuel flow rate, full nozzle expansion, and the stationary case, the following equation yields the thrust equation for specific thrust.

$$F_{sp} = V_9 \tag{2.7}$$

For modern low bypass engines, the nozzle exhaust velocity can be more than 1100 m/s with an afterburner and 700 m/s without an afterburner (Huenecke, 1987).

2.1.2.3. Specific fuel consumption

Specific fuel consumption (SFC) refers to the amount of fuel required to produce one horsepower for a specified period (Huenecke, 1987).

$$SFC = \frac{m_f}{F} \tag{2.8}$$

When evaluating an engine’s performance, the most critical characteristic variable is its particular fuel consumption. Afterburning consumes a disproportionate amount of carbon. Therefore, engines with high bypass ratios are less advantageous for afterburning than engines with low bypass ratios, where the BPR of a turbofan engine is the ratio of the mass flow rate of the bypass flow to the mass flow rate of the core. For military aircraft engines, fuel consumption values with afterburning are nearly four times those without afterburner.

2.1.3. Aerodynamics

This section discusses the aerodynamic terminology used and variables in propulsion system integration. These variables influence thrust loss due to propulsion system integration.

2.1.3.1. Speed of sound and Mach number

The air is composed of many molecules that move spontaneously with an instantaneous velocity and energy that change over time. These molecules define a mean value for the molecular velocity and energy-dependent ambient temperature for a perfect gas. For example, when considering a balloon burst, energy is emitted and absorbed by the nearest nearby molecules in the air, increasing their molecular velocity and causing them to collide with neighbouring molecules. Energy is exchanged between the molecules during the collision and propagates into space, forming an energy wave. Additionally, the increased energy in the wave generates a pressure shift, which the microphone detects and interprets as sound (Anderson, 2004). These waves are called sound waves, and the speed at which sound waves travel is the speed of sound. In dry and ideal weather at sea level, the speed of sound is 340 m/s.

As shown in Figure 12, the wave reaches the flow in front of it with velocity V_∞, pressure p_∞, density ρ_∞, and temperature T_∞, while the flow behind it moves with velocity V_1, pressure p_1, density ρ_1, and temperature T_1 (Anderson, 2004).Then, utilizing the continuity equation, velocity is calculated for two regions.

$$\dot{m}_\infty = \dot{m}_1 \tag{2.9}$$

$$\rho_\infty a = (\rho_0 + d\rho)(a_\infty + da); a = -\rho \frac{da}{d\rho} \tag{2.10}$$

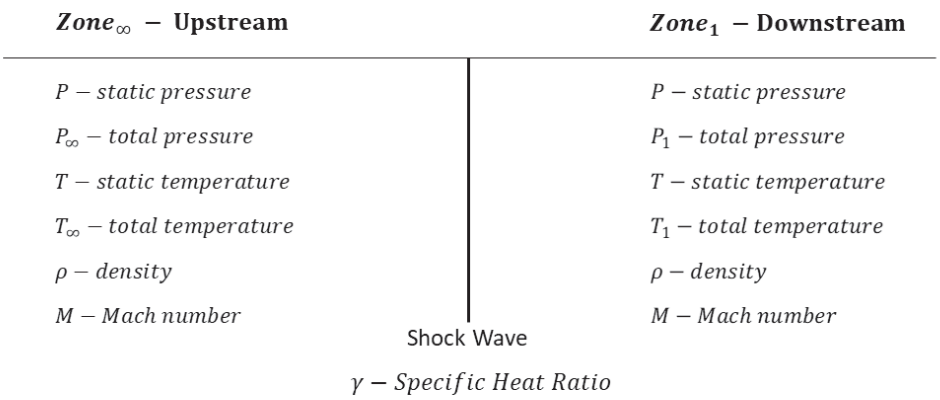

Figure 12 Flow Characteristic for Downstream and Upstream (NASA, Compressible Aerodynamics Index, 2021)

With momentum equation, the propagation of a sonic wave is assumed to be isentropic, and thermodynamic property relations, the speed of sound, a, in an ideal gas is defined as

$$a = \sqrt{\gamma RT} \tag{2.11}$$

where γ, is defined as the specific heat ratio of the air, R is the specific gas constant, and T is the temperature in degree Kelvin (Cengel & Boles, 2007). Hence, Mach number is defined as,

$$M = \frac{V}{a} \tag{2.12}$$

Flow can be classified into three types based on the Mach number. Subsonic if M is less than one, sonic if M equals one, and supersonic if M is greater than one.

2.1.3.2. Shock Wave

A sonic wave's propagation can be directly compared to the water rings on the surface, with the source of sound in the middle. Source moves at a subsonic rate. Thus, the waves appear "Subsonic" in Figure 13, while the source in front of the waves at sonic and supersonic speeds. When an object travels at sonic velocity, M=1, the waves are concentrated at the object's nose, as shown by the "Speed of Sound" case in Figure 13, and combine to form a more violent wave known as a shock wave. The flow in front of the moving object, also known as upstream flow, is unaware of the approaching object but changes direction and slows down as soon as it passes the shock. As the velocity decreases, the flow's static pressure, density, and temperature increase. At supersonic speeds, the waves are too slow to follow the object and spread behind it, resulting in an angled Mach wave, denoted by the case "Supersonic" in Figure 13, which can be observed as an infinitely weak oblique shock (Anderson, 2004).

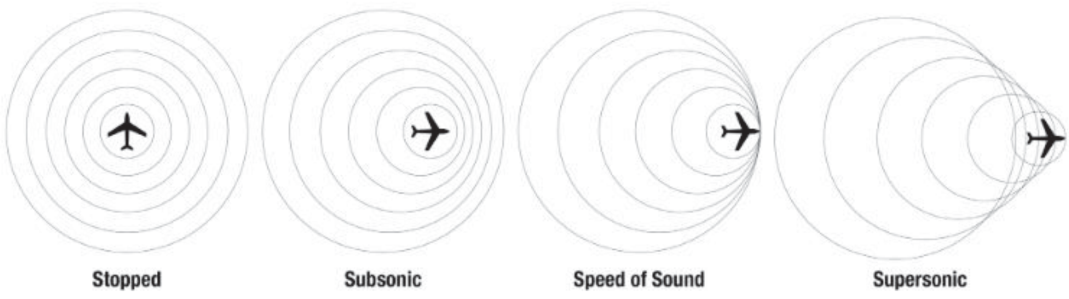

Figure 13 Pressure Waves of Air Flowing Off an Aircraft (NASA, The History of NASA's Sonic Boom Research, 2019)

The two types of shocks are referred to as normal shock waves and oblique shock waves. Normal shock waves are perpendicular to the plane of free flow. The flow is flowing through normal shock experiences substantial velocity losses, but the amount depends on the speed of the upstream flow (Anderson Jr., 2010). The relationship between the upstream flow Mach number, M_1, and the downstream flow Mach number, M_2, is developed and described as follows,

$$M_2^2 = \frac{M_1^2 + \frac{2}{\gamma - 1}}{\left(2 * M_1^2 * \frac{\gamma}{\gamma - 1}\right) - 1} \tag{2.13}$$

According to the equation (2.13) an upstream supersonic Mach number close to 1 results in a higher downstream subsonic Mach number and decreases velocity losses (Anderson, 2004).

In contrast to a typical shock wave, an oblique shock wave is angled about the incident upstream flow direction. It occurs when a supersonic flow reaches a corner that effectively compresses the flow. Following the shock wave, the upstream streamlines are evenly deflected. The most frequent generating an oblique shock wave is introducing a wedge into a supersonic compressible flow. As with a conventional shock wave, an oblique shock wave consists of a very tiny zone during which practically discontinuous changes in gas flow thermodynamic parameters occur. The downstream direction of the flow is deflected when passing through an oblique shock wave (Cengel & Boles, 2007) (Anderson, 2004).

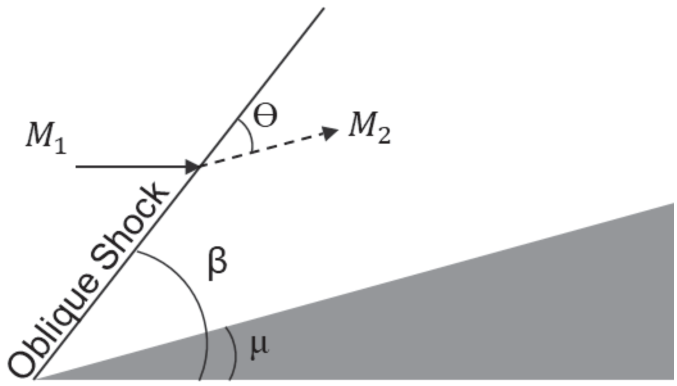

Figure 14 Oblique Shock and Parameters

Calculations of the oblique shock angle, beta, and downstream Mach number, M_2, can be calculated for a given Mach number, M_1 and a corner angle, θ. Unlike following a conventional normal shock, where M_2 must always be smaller than 1, following an oblique shock, M_2 can be supersonic, producing a weak shock wave, or subsonic, producing a strong shock wave. Weak solutions are frequently encountered in open flow geometries, such as outside of a flight vehicle. In constrained geometries, robust solutions can be observed, such as inside a nozzle intake. When the flow must match the downstream high-pressure situation, robust solutions are necessary. Additionally, discontinuous changes in pressure, density, and temperature occur downstream of the oblique shock wave.

Trigonometric relations eventually lead to the θ - β - M equation, which expresses θ as a function of M_1, β, and γ, where γ is the heat capacity ratio.

$$\tan\theta = 2\cot\beta\frac{M_1^2\sin^2\beta - 1}{M_1^2(\gamma + \cos 2\beta) + 2} \tag{2.14}$$

While it is more straightforward to solve for β as a function of M_1 and θ, this approach is more involved, with the solutions being included in tables or calculated numerically.

2.1.3.3. Isentropic flow, ideal gas

The flow-through a tube with a gradually decreasing area and subsequently an increasing area, commonly known as a Laval tube, is a reversible process in which the flow conditions revert to their initial level (Munson B. R., 2012). According to the second law of thermodynamics, reversible, adiabatic flows have constant entropy and are called isentropic flows (Cengel & Boles, 2007).

For high-speed flows, the stagnation enthalpy, h_0 , reflects the total energy contained in a flowing fluid stream and is described as

$$h_0 = h + \frac{v^2}{2} \tag{2.15}$$

The first term, h, represents the internal enthalpy. The second term represents kinetic energy per mass.

$$c_p T_0 = c_p T + \frac{v^2}{2} \tag{2.16}$$

$$\frac{T_0}{T} = 1 + \frac{v^2}{2c_p T} \tag{2.17}$$

The stagnation enthalpy of ideal gases with constant specific heat is denoted by h_0 in the entropy equations, where T_0 is the stagnation (total) temperature, T is the static temperature, and c_p is the specific heat capacity at constant pressure.

The following relations are constructed using state equations and speed of sound equations (NASA, Aerodynamics Index Glenn Research Center, 2021),

$$\frac{T_0}{T} = 1 + \left(\frac{\gamma - 1}{2}\right) M^2 \tag{2.18}$$

$$\frac{P_0}{P} = \left(1 + \left(\frac{\gamma - 1}{2}\right) M^2\right)^{\frac{\gamma}{\gamma-1}} \tag{2.19}$$

$$\frac{\rho_0}{\rho} = \left(1 + \left(\frac{\gamma - 1}{2}\right) M^2\right)^{\frac{\gamma}{\gamma-1}} \tag{2.20}$$

where P_0, T_0, and ρ_0 denote total quantities and are denoted by isentropic flow relations. P, T, and ρ are all static quantities, while M represents the Mach number and c_p represents the specific heat ratio (Anderson, 2004).

2.1.3.4. Viscosity and compressibility of flows

The viscosity and compressibility of air are affected by the Mach number and altered as the speed increases. The compressibility effects are negligible at speeds less than 320 km/h, incompressible flow. The dynamic pressure for incompressible fluids and mass flow is given as,

$$q = 0.5\rho V^2 \tag{2.21}$$

$$\dot{m} = \rho V A \tag{2.22}$$

where V denotes velocity, ρ denotes density, and A denotes cross-section area at a particular station. When the speed of the air exceeds 320 km/h, flow is considered to be compressible, and the mass flow is defined as,

$$\frac{\dot{m}\sqrt{T_0}}{AP_0} = \sqrt{\frac{\gamma}{R}} * M * \left(1 + \frac{\gamma - 1}{2} M^2\right)^{\left(-\frac{\gamma+1}{2(\gamma-1)}\right)} \tag{2.23}$$

$$\dot{m} = \frac{AP_0}{\sqrt{T_0}} * \sqrt{\frac{\gamma}{R}} * M * \left(1 + \frac{\gamma - 1}{2} M^2\right)^{\left(-\frac{\gamma+1}{2(\gamma-1)}\right)} \tag{2.24}$$

A is the cross-section area of each engine station, P_0 denotes the total pressure, and T_0 denotes the total temperature. R is the constant of a specific gas, equal to 287.074.

For high velocities, the dynamic pressure q is rewritten in terms of the Mach number, which is equivalent to Eq. 2.21 and is expressed as (Cengel & Boles, 2007) (Anderson, 2004),

$$q = \frac{\gamma}{2} * P_\infty * M_\infty^2 \tag{2.25}$$

where P_∞ denotes pressure of the free stream.

2.1.4. Drag Definitions

The critical value in determining aircraft performance is not calculating drag but the balance of thrust and drag. The operation of the propulsion system affects the drag of the aircraft, and care must be given to understand and specify these relationships. For example, the engine’s air consumption dictates the size of the stream tube entering the entrance. If the inlet does not suck all air in front of the inlet, a spilling drag occurs. Similarly, the drag of the boat-tail over the external portion of the nozzle is dependent on the nozzle setting (in the case of engines equipped with afterburners) and the nozzle flow pressure. Thrust-drag book-keeping is the process of appropriately accounting for aero-propulsion interactions when specifying thrust minus drag numbers.

2.1.4.1. Spillage drag

Spillage drag is described as airflow caught by the inlet but can not be sucked by the engine, which flows outside the inlet and generates spillage drag, as illustrated in Figure 15. The air inlet is intended for maximum engine airflow, which is unnecessary, and the amount of split air changes when the throttle is adjusted. The spilling drag is affected by two factors: the momentum loss in the free stream tube and the behaviour of the air as it passes the cowl lip (Ball W. H., 1972).

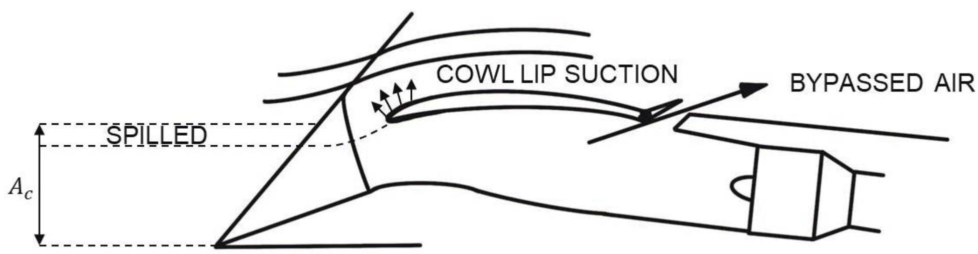

Figure 15 Additive Drag, Lip Suction and Bypass Drag (Ball W. H., 1972)

The first effect is called additive drag or pre-entry drag, and it is caused by airflow losses from the freestream tube to the inlet orifice. The additive drag is dependent on the arrangement of the inlet, the free-stream Mach number, and the shock geometry. The term additive drag refers to;

$$F_{D_{Add_{normal}}} = \int (P - P_\infty) dA = \dot{m}\, V_{inlet} + A_1 (P_{inlet} - P_\infty) - \dot{m} V_\infty \quad (2.26)$$

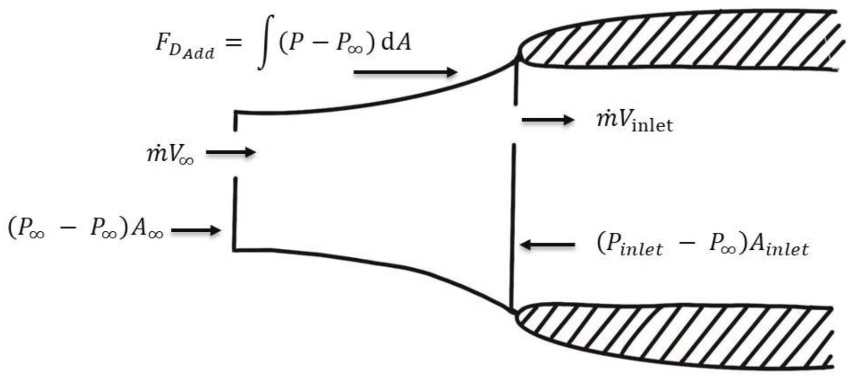

Figure 16 Additive Drag for Pitot Inlet (Ball W. H., 1972)

A normal shock inlet is referred to as a pitot inlet, where A_1 denotes the cross-sectional area at the inlet lip, V denotes the velocity, P denotes the static pressure at the inlet lip, showed with subscript inlet, and ∞ is the free stream. This equation holds for all Mach values for an external compression pitot inlet. The additive drag for oblique shock inlets is defined as;

$$F_{D_{Add_{oblique}}} = \int (P - P_\infty) dA = [\dot{m} v_{inlet} + A_{inlet} (P_{inlet} - P_\infty)] cos\alpha - \dot{m} v_\infty + A_R (P_R - P_\infty) \ (2.27)$$

For all flight Mach values with normal shock within and near the intake lip, where $P_R$is pressure on-ramp, A_R is ramp area, and $A_R(P_R - P_\infty)$ is described as ramp drag and determined from previous studies presented by Ball W.H., and the angle α is the angle of the slope depicted in Figure 17 (Ball W. H., 1972).

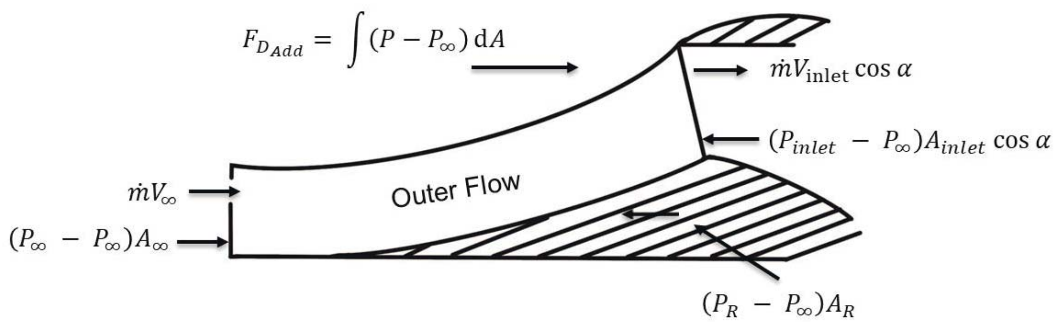

Figure 17 Additive Drag for Oblique Shock Inlet (Ball W. H., 1972)

The second phenomena are the lip suction effect, and it occurs as spilt air accelerates over the cowl lip, lowering pressure and producing a negative drag that partially cancels out the added drag. The lip suction effect is determined by the form of the cowl lip, bluntness, and side plate cutback and is represented as a correlation factor K_{add}, which is multiplied by the additive drag to obtain the total spillage drag.

$$F_{D_{spill}} = F_{D_{add}} * K_{add} \tag{2.28}$$

The correlation coefficients are determined experimentally and found in graphs and tables for various inlet configurations (Ball W. H., 1972). The coefficient of spillage drag is determined using the Eq. (1.1) and the capture area, A_C, as the reference area, which in this situation equals,

$$C_{D_{spill}} = \frac{F_{D_{spill}}}{q\ A_C} \tag{2.29}$$

q denotes the compressible flow's dynamic pressure, the capture area of a pitot inlet is equal to the area enclosed by the cowl lip, but the capture area of an oblique shock inlet is represented in Figure 17. When dealing with aircraft inlets, there are two other considerations. These two contribute to various mass flows and are known as the local stream tube area ahead of the inlet A_0 and the free-stream tube area of air entering the inlet A_{0I}. Because the density and velocity of the entering air remain constant, the ratios between the mass flow are represented by the ratios between the areas in Eq. 2.24. Figure 6 depicts the local stream tube area upstream of the entrance and the freestream tube area of air entering the entrance (Goldsmith & Seddon, 1993). Ratio between A_0 and A_{0I} defined as (Ball W. H., 1972);

$$\frac{A_{0I}}{A_0} = \frac{A_0}{A_C} + \frac{A_{0BLC}}{A_C} \tag{2.30}$$

where, ${A_{0BLC}}/{A_C}$ is bleed mass flow ratio. Although bleed at intake can reduce the boundary layer, it generates extra drag due to momentum loss. With a well-designed bleed system, these losses can be recovered at the end of the bleed outlet. In the conceptual design phase, it is a decent starting assumption to select 0.3 to 0.7 percentage bleed momentum loss that can be recovered (Ball W. H., 1972). Free stream tube area A_0, is defined concerning Mach number as (Ball W. H., 1972);

$$A_0 = \frac{\sqrt{R} \ * \sqrt{T_{02}} \ * \ \dot{m}_2 * \left(1 + \frac{\gamma - 1}{2} M^2\right)^{\left(-\frac{\gamma+1}{2(\gamma-1)}\right)}}{\sqrt{\gamma} \ * P_{02} * \ M} \tag{2.31}$$

where $\dot{m}_2$ is the required mass flow by the engine and corresponds to the area ratio. T_{02} and P_{02} denote the total temperature and pressure in the freestream, respectively. M denotes the flying Mach number, while γ is the surrounding air's specific heat ratio.

2.1.4.2. Boat-tail drag

Boat-tail drag is described as the drag caused at the engine nozzle by external airflow, varying in size depending on the exit and boat-tail area, where boat tail diameter is presented as D_9 in Figure 18 (Ball W. H., 1972). The nozzle opening is adjustable for various boat-tail angles, which are described as the angle formed by the straight line between the nozzle's knuckle outer diameter, D_m, the nozzle exit diameter D_9 and nozzle exit diameter, including nozzle base radius D_b and Figure 18 illustrates these definitions. Reduced area results in an increased boat-tail angle, which results in the separation of the external flow and the creation of pressure drag.

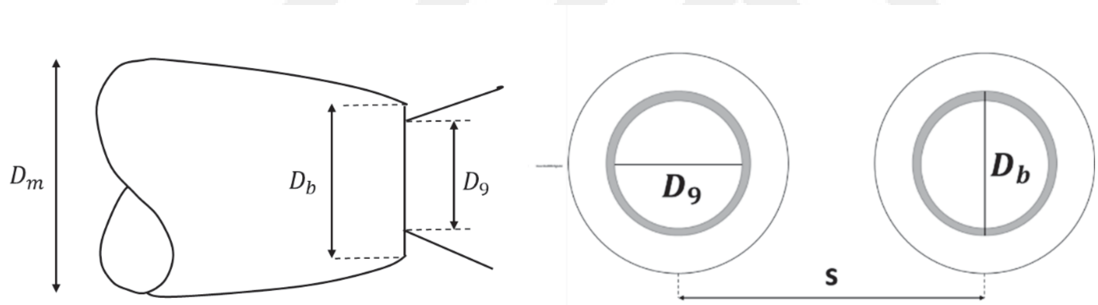

Figure 18 Nozzle Drag Parameters (Huenecke, 1987)

The boat-tail drag coefficient is defined as follows for circular arc nozzles (Ball W. H., 1972):

$$c_{D_\beta} = \frac{1 \cdot 4 \tan \beta}{M_\infty^{1.53}} \left[1 - \left(\frac{D_9}{D_m}\right)\right] \tag{2.32}$$

Eq. (2.32) is for supersonic speeds, which means $1.0 \leq M < 3.0$. For subsonic speeds, the boat-tail drag should be calculated according to nozzle shape. In addition, NASA's F-15 wind test tunnel results on a 1/12 scale are used for pressure distribution on afterbody and installation losses for twin-engine configuration. (Odis C. Pendergraft, 1979). The boat-tail drag coefficient for $\frac{D_9^2}{D_b Dm} > 0.25$, nozzle pressure ratio, is calculated using tabulated data and plotted in Appendix - E (Ball W. H., 1972). Appendix - F illustrates the coefficient of total boat-tail drag for 2.5 < NPR <8 at subsonic speeds.

Flying at supersonic speeds eliminates the negative drag created by the plume. The afterbody's flow field is complex due to the expansion waves generated by the afterbody and the shock pattern generated by the plume. For larger D_m, the impact of the propulsive jet results in a boat-tail drag coefficient between 2 and 7 as,

$$C_{D_{\beta_{sublarge}}} = C_{b_{\beta z}} + \frac{\partial C_{D_\beta}}{\partial C_{p_b}} * \Delta C_{p_b} \tag{2.33}$$

where $C_{b_{\beta z}}$ is the zero flow boat-tail drag as determined by the tables (McDonald & P. Hughest, 1965), and $\frac{\partial C_{D_\beta}}{\partial C_{p_b}}$ is the rate of change for the boat-tail drag according to the base pressure drag, as shown in Appendix E and F. ΔC_{p_b} denotes the base pressure increase;

$$\Delta C_{p_b} = \Delta C_{p_b}\left(\frac{D_9^2}{D_b D_m} = 0\right) + \frac{\partial \Delta C_p}{\partial\left(\frac{D_j^2}{D_b D_m}\right)} * \frac{D_j^2}{D_b D_m} \tag{2.34}$$

where, $\left(\frac{D_j^2}{D_b D_m} = 0\right)$ donates the zero jet diameter and second term, gradient, tabulated from past studies on nozzle drag (Ball W. H., 1972).

Eq (1.1) is used to calculate the boat-tail drag, with the knuckle area as the maximum reference area, which equals;

$$F_{D_{BT}} = C_{D_\beta} * q * A_{max} \tag{2.35}$$

where q denotes the dynamic pressure, incompressible flows, and A_{max} denotes the afterbody's knuckle area.

2.1.4.3. Base drag

The base area, A_{base} is defined as the small circular region formed by the diameter at the nozzle's end of the outer shell and the diameter of the jet. Figure 18 illustrates the fundamental drag parameters. Between the jet and the base, a tiny area of low pressure is generated. The jet's fast-moving air creates a pumping action, where the jet wishes to remove the air, resulting in decreased pressure over the base surface. The boundary layers near the nozzle exit affect the total drag and act as an insulator, lowering the outer flow's adequate dynamic pressure and reducing the jet pump effect (Hoerner, Aerodynamic Drag, 1951).

The base drag coefficient is the function of the pressure ratio between the jet and the outside flow, the boat-tail angle, the Mach number, and the nozzle geometry. For subsonic speeds, the propulsive jet impact must be accounted for utilising the technical paper method (Ball W. H., 1972) for specified nozzle geometries. With a larger base diameter, D_b, the jet plume has a higher impact. For smaller dimensions of D_b, the effect is ignored, and the base drag coefficient is specified as;

$$C_{D_{BS_{subsmall}}} = \frac{2A_{Base}}{\gamma M_\infty^2 A_{knuckle}}\left(1-\frac{p_b}{p_\infty}\right) = \frac{2\left(\left(\frac{D_b}{D_j}\right)-1\right)}{\gamma M_\infty^2 \left(\frac{D_m}{D_m}\right)^2}\left(1-\frac{p_b}{p_\infty}\right) \tag{2.36}$$

where A_{Base} denotes the circular base area, $A_{knuckle}$ denotes the nozzle's maximum outer area, knuckle area and $\frac{p_b}{p_\infty}$ denotes the base pressure ratio.

For the larger diameter, D_b, the effect of the propulsive jet results in the formation of the base drag coefficient, which is denoted by;

$$C_{D_{BS_{sublarge}}} = -\left(\frac{D_b^2 - b_j^2}{D_{max}^2}\right)\left(C_{p_{bz}} + \Delta C_{p_b}\right) \tag{2.37}$$

where $c_{p_{bz}}$ denotes the datum pressure, ΔC_{p_b} denotes the increase in the base pressure obtained from a report (McDonald & P. Hughest, 1965). To calculate the base drag for supersonic flight;

- Calculate the correlation parameter C that corresponds,

$$C = (0.37M_\infty + 0.62) * \left(M_{9_{design}} \frac{\left(2\frac{D_b}{D_9} - 1.5\right) * M_{9_{design}}}{10}\right) * \left(\frac{A_j}{A_j + A_{Base}}\right) * \left(\frac{p_9}{p_\infty}\right) \tag{2.38}$$

where $M_{9_{design}}$ is Mach number of jet velocity at station 9 for design case and p_9 is total pressure for the jet stream.

- Determine correlation parameter B that corresponds to tables in Appendix G.
- Calculate the coefficient of velocity decay, K for $\frac{p_{t9}}{p_\infty} > 1$

$$K = \frac{M_\infty O_B + M_j O_j}{O_e} \tag{2.39}$$

otherwise, K = M

- Find $\left(\frac{p_b}{p_\infty}\right)_K$ from the tables (Ball W. H., 1972). Appendix I

- Compute $\left(\frac{p_b}{p_\infty}\right)_M$ using B and $\left(\frac{p_b}{p_\infty}\right)_K$ with,

$$B = M_\infty ln^{-1}(0.81 - 1.15\, lnK) \left(\frac{p_b}{p_\infty}\right)_M \left(\frac{p_b}{p_\infty}\right)_K^{-1} \tag{2.40}$$

- Calculate the drag coefficient,

$$C_{D_B} = \frac{2A_{Base}}{\gamma M_\infty^2 A_M}\left(1 - \left(\frac{P_b}{p_\infty}\right)_m\right) = \frac{2\left(\left(\frac{D_b}{D_j}\right)^2 - 1\right)}{\gamma M_\infty^2 \left(\frac{D_{max}}{D_j}\right)^2}\left(1 - \left(\frac{p_b}{p_\infty}\right)_M\right) \tag{2.41}$$

Eq (1.1) is used to present the base drag, with the knuckle area as the maximum reference area, which equals;

$$F_{D_{BS}} = C_{D_{BS}} * q * A_{max} \tag{2.42}$$

where q denotes the dynamic pressure, incompressible flows, and A_{max} denotes the afterbody's knuckle area.

The upper limit on base drag is the highest pressure differential between the base pressure at the exit and the ambient pressure, which occurs when the base drag pressure equals vacuum. The maximum base drag coefficient is defined as the dynamic pressure multiplied by the maximum base drag coefficient (Hoerner, Base Drag and Thick Trailing Edges, 1950).

$$C_{DB_r} = -\left(\frac{\Delta p}{q}\right)_{max} = \left(\frac{p_{base} - p_{amb}}{q}\right)_{max} \tag{2.43}$$

Eq. 2.43 can be rewritten using the dynamic equation formula and the ideal gas assumption as follows,

$$C_{DBmax} = -\left(\frac{-p_{amb}}{0.5\gamma p_{amb} M^2}\right) = \frac{2}{\gamma M^2} \tag{2.44}$$

Hence, maximum base drag,

$$F_{D_{base_{max}}} = C_{DB_{max}} * q * A_{base} \tag{2.45}$$

where q denotes the dynamic pressure, incompressible flows, and A_{base} denotes the nozzle base area.

2.1.4.4. Interference drag

When two aircraft engines operate nearby, the combined drag is greater than the sum of the two independent free flow drags. Interference drag is the difference in drag due to engine spacing. Interference drag occurs when two bodies share an external airstream, and each body's flow field is affected by the other body. The distance between the two engines, the diameter of the nozzle exit, and the Mach number are all characteristics that affect the amplitude of the interference drag and are presented against the interference drag coefficient, $c_{D_{IN\,N_{eng}}}$, in Appendix I (Ball W. H., 1972), which is defined for N_{eng} engines as,

$$c_{D_{IN\,N_{eng}}} = \frac{F_{D\,IN_{eng}}}{2\left(F_{g,i}\right)_{\frac{p_t}{p_\infty}=2.5}} \tag{2.46}$$

The ideal gross thrust, $F_{g,i}$, is denoted by the following:

$$F_{g,i} = p_{amb} A_8 f\left(\frac{p_t}{p_\infty}, \gamma\right) \tag{2.47}$$

The interference drag for a single-engine, $F_{D\,IN}$, is computed by multiplying the engine spacing by

$$F_{D\,IN} = F_{D\,IN_{eng}}\left(\frac{N_{eng} - 1}{N_{eng}}\right) \tag{2.48}$$

The distance between engines is referred to as engine spacing, and it affects the magnitude of drag. Figure 19 presents engine spacing, whereas Figure 20 illustrates drag shift as a function of engine spacing (Huenecke, 1987).

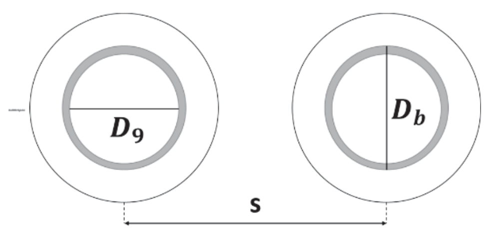

Figure 19 Engine Spacing (Huenecke, 1987)

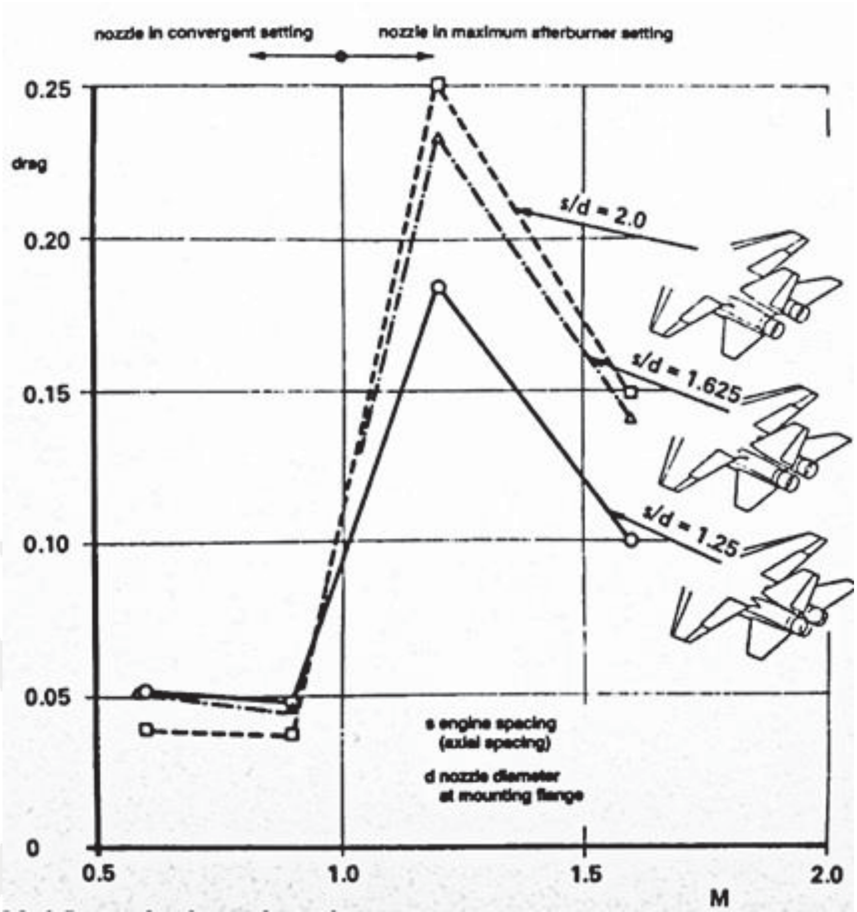

Figure 20 Influence of Engine Spacing on Nozzle Drag (Huenecke, 1987)

where, s is engine spacing, and d is nozzle diameter at knuckle area.

Definitions and calculation algorithms of drag forces caused by nozzle/afterbody integration are given separately in sections 2.1.4.2 Boattail Drag, 2.1.4.3 Base Drag and 2.1.4.4 Interference Drag section. In Figure 21, the drag forces from the afterbody integration are given as a flowchart.

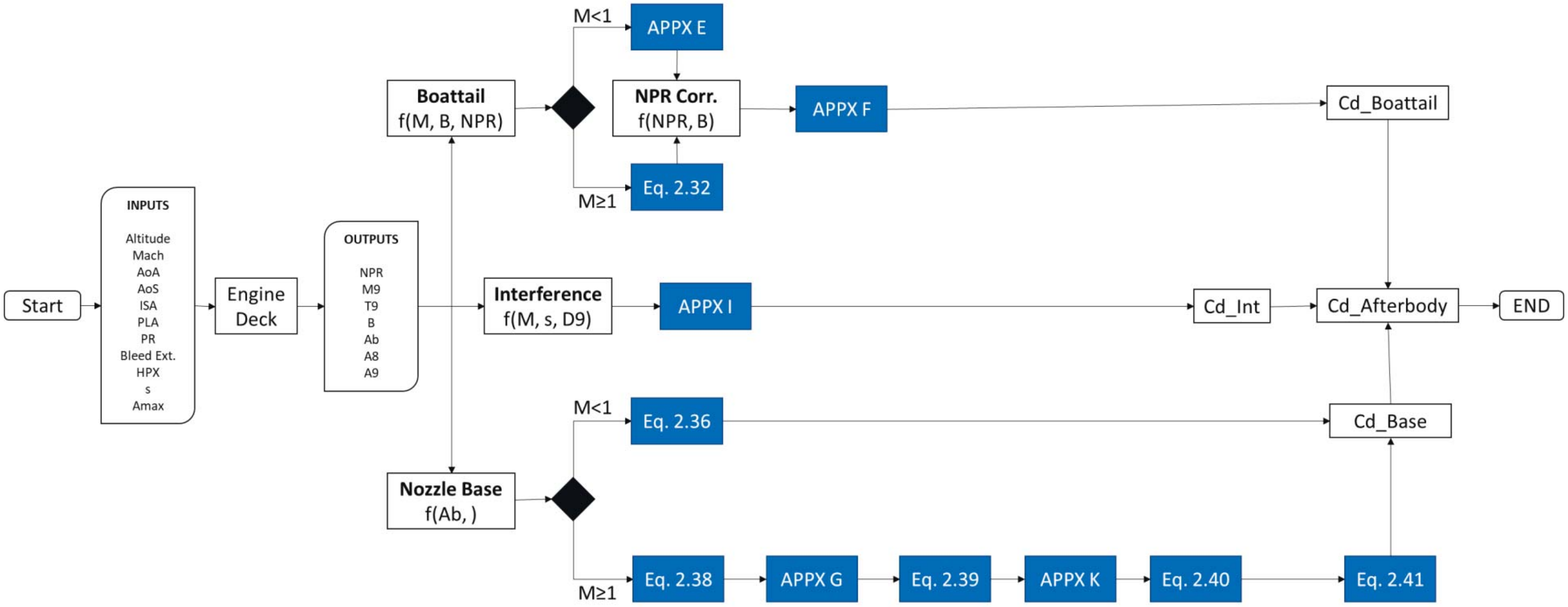

Figure 21 Flowchart of Nozzle/Afterbody Drag Calculations

3. VALIDATION

In a former study, the engine model utilized in NPSS was nearly identical to a J79-GE-8 engine, with some variations in the input data at various Mach numbers (Karaselvi, 2018). This created issues in validating the experimental performance data obtained from GE's documentation against the results from the NPSS equations, as the results would not be equal. They are allowing for validation of the outcomes of the in-house Python code for each installation effect made. These codes allow the tables presented in Appendix A, B, and C to be integrated into NPSS. Thus, the validation of the implemented equations in NPSS was performed in two parts for each installation effect. First, validation of the Python code using data from The Boeing Company's experimental performance data. Furthermore, the second validation of the equations implemented in NPSS against the Python code used in the validation phase.

The validation phase suggested that the in-house Python code used the same input parameters as the Boeing documentation. Six distinct operational points with varying Mach values and flight altitudes were defined for the input data. The validation results, the calculated drag coefficients for the Boeing content, and Python code calculation were shown in scatter plots, Figure 22 and Figure 23 . The verification phase employed the same Python code as the previous phase but with input parameters from the NPSS engine model.

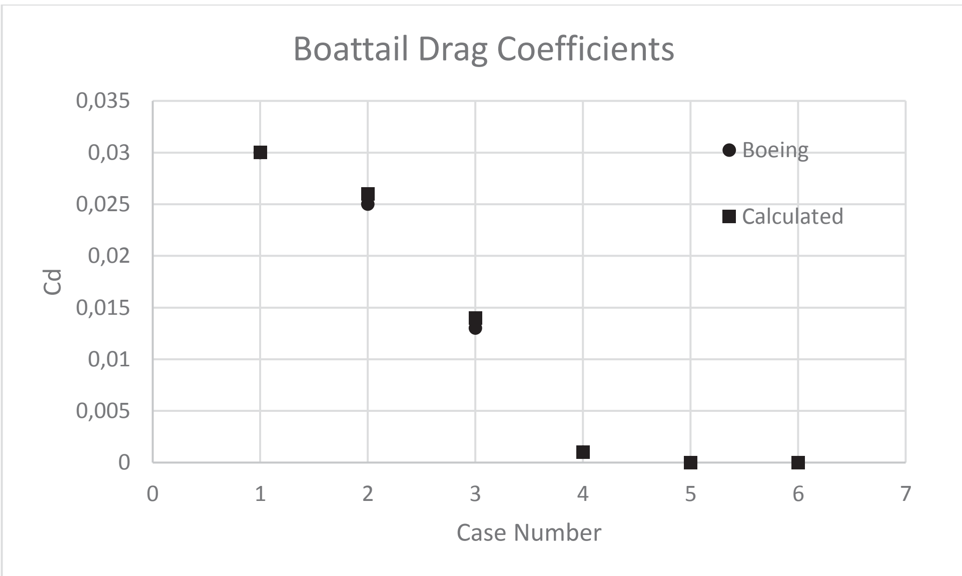

Figure 22 Comparison of Boattail Drag Coefficients

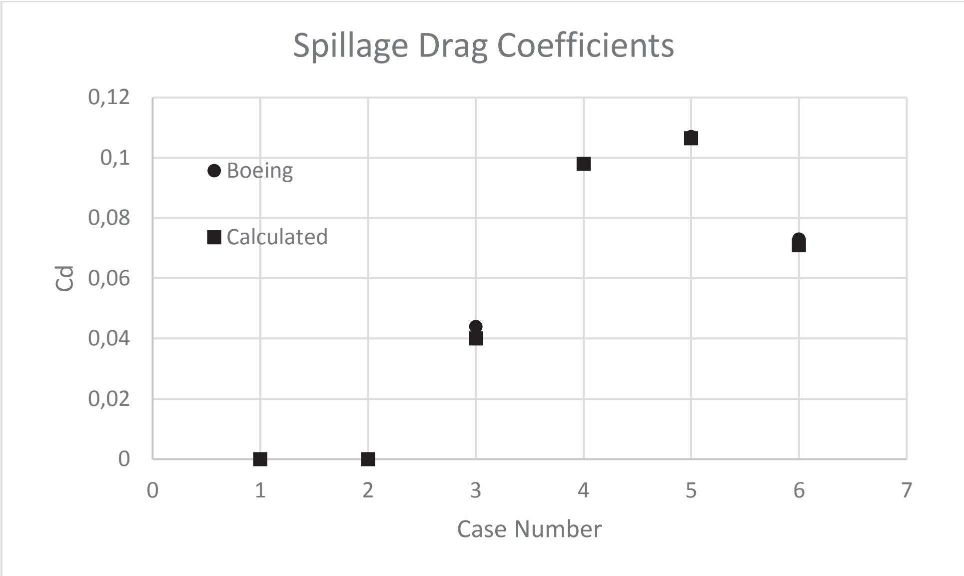

Figure 23 Comparison of Spillage Drag Coefficients

The calculations were carried out for the six matching operating points, and the resulting drag coefficients were presented in Figure 22 and Figure 23. If the output data from the two sources are consistent, the equations implemented in NPSS will be correct.

The Python routines are implemented to get values as user input from the graphs in reports prepared by Balls, and Figure 24 summarizes the six simulated operating locations (Ball W. H., 1972).

#	1	2	3	4	5	6
M	0.4	0.6	0.8	1.2	1.6	2
Alt [m]	4572	7620	10668	13716	10668	10668

Figure 24 Flight Conditions

3.1. Comparison

Figure 25 compares the values calculated using the methods with the Boeing Experimental Results.

	1			2			3		
VariableInput	INPUT	Experimental data	Calculated	INPUT	Experimental data	Calculated	INPUT	Experimental data	Calculated
M	0.4			0.6			0.8		
Alt [m]	4572			7620			10668		
Pamb [kPa]	57.1166			35.1324			23.7734		
Ac	0.633598733			0.633598733			0.633598733		
m_corr [kg/s]	82.369			85.704			81.132		
PqP	0.977			0.98			0.984		
Dmax [mm]	980.44			980.44			980.44		
S [mm]	1366.52			1366.52			1366.52		
L_nozzle [mm]	594.36			594.36			594.36		
A8 [m2]	0.447560395			0.469159707			0.49761965		
A9 [m2]	0.464266168			0.501803513			0.55846598		
Q [Pa]	6397			8977.8			10650.5		
Pt8P0	2.414			2.677			3.057		
B [deg]		10.084	10.093		8.654	8.663		6.573	6.584
Cd_B_2.5		-	0.0299		-	0.025		-	0.0141
Cd_B		0.03	0.03		0.025	0.026		0.013	0.014
F_bt [N]		144.9	145.7		172.66	175.93		106.27	111.86
Cd_int_n_eng		-	NaN		-	0.005		-	0.013
Cd_int		0.031	NaN		0.026	0.025		0.043	0.043
F_int [N]		148.8	NaN		176.23	168.11		346.56	341.43
Cd_spill		0	NaN		0	NaN		0.044	0.04
F_spill [N]		0	NaN		0	NaN		296.92	269.93
A0AC		0	0.837		0	NaN		0.547	0.551
A0AC1		0	0.837		0	0.6529		0.542	0.542

	4			5			6		
VariableInput	INPUT	Experimental data	Calculated	INPUT	Experimental data	Calculated	INPUT	Experimental data	Calculated
M	1.2			1.6			2		
Alt [m]	13716			10668			10668		
Pamb [kPa]	14.7998			23.7734			23.2946		
Ac	0.633598733			0.633598733			0.633598733		
m_corr [kg/s]	80.992			78.213			63.407		
PqP	0.984			0.935			0.904		
Dmax [mm]	980.44			980.44			980.44		
S [mm]	1366.52			1366.52			1366.52		
L_nozzle [mm]	594.36			594.36			594.36		
A8 [m2]	0.559949848			0.52423379			0.538814406		
A9 [m2]	0.715812762			0.754975264			0.754975264		
Q [Pa]	14918.2			42602			66565.6		
Pt8P0	4.09			6.466			8.241		
B [deg]		1.23	1.24		-0.012	-0.00004		-0.012	-0.00005
Cd_B_2.5		-	-		-	-		-	0
Cd_B		0.001	0.001		0	0		0	0
F_bt [N]		13.52	13.413		0	0		0	0
Cd_int_n_eng		-	0.019		-	0.0063		-	0.0046
Cd_int		0.03	0.03		0.0056	0.0053		0.0027	0.0025
F_int [N]		337.9	341.68		180.3	170.4		138.98	125.23
Cd_spill		0.098	0.098		0.107	0.1065		0.073	0.071
F_spill [N]		926.31	923.48		2888.2	2874.4		3078.8	2934.2
A0AC		0.55	0.5511		0.619	0.619		0.663	0.6638
A0AC1		0.537	0.537		0.598	0.598		0.632	0.6328

Figure 25 Comparison Table Between Experimental Data and Calculated Results

4. IMPLEMENTATION OF PROPULSION SYSTEM INTEGRATION LOSSES TO F22

F-22 Raptor is a single-seat, twin-engine, all-weather stealth tactical fighter aircraft explicitly built for the US Air Force (USAF) by Lockheed Martin. The aircraft is the culmination of the USAF's Advanced Tactical Fighter (ATF) programme. It is designed as an air superiority fighter and includes ground attack, electronic warfare, and signal intelligence. Lockheed Martin was the prime contractor and built most of the F-22's airframe and armament systems, while Boeing provided the wings, aft fuselage, avionics integration, and training systems.

The aircraft was formerly known as the F-22 and F/A-22 before entering service as the F-22A in December 2005. Despite the F-22's lengthy development and numerous operational challenges, USAF officials regard it as a crucial component of the service's tactical air force. Its unmatched air warfare capabilities are enabled by its stealth, aerodynamic performance, and avionics systems.

4.1. Design of Aircraft Engine

Engine decks are defined as computer programmes provided by the engine's original equipment manufacturer (OEM) to display engine performance data in a table format. The F-22 aircraft's engine performance is modelled using NPSS using an engine deck comparable to the F119-PW-100. NPSS schematic is presented in Figure 27.

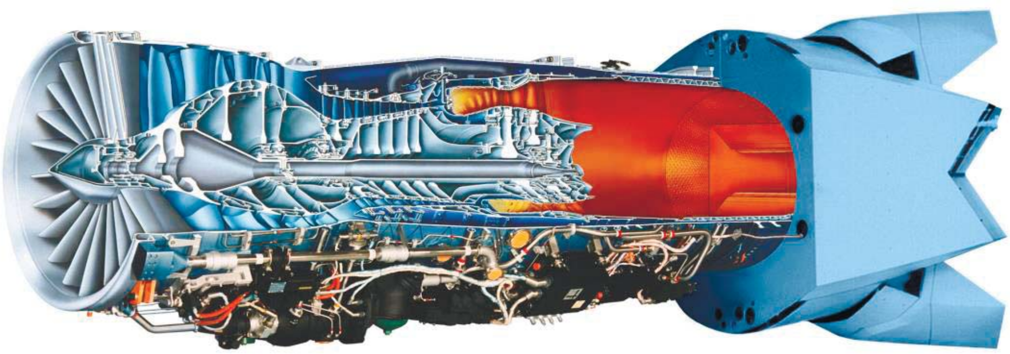

Figure 26 Cutaway of F119-PW-100 Engine (Mattingly & Boyer, Elements of Propulsion: Gas Turbines and Rockets American Institute of Aeronautics and Astronautics, 2006)

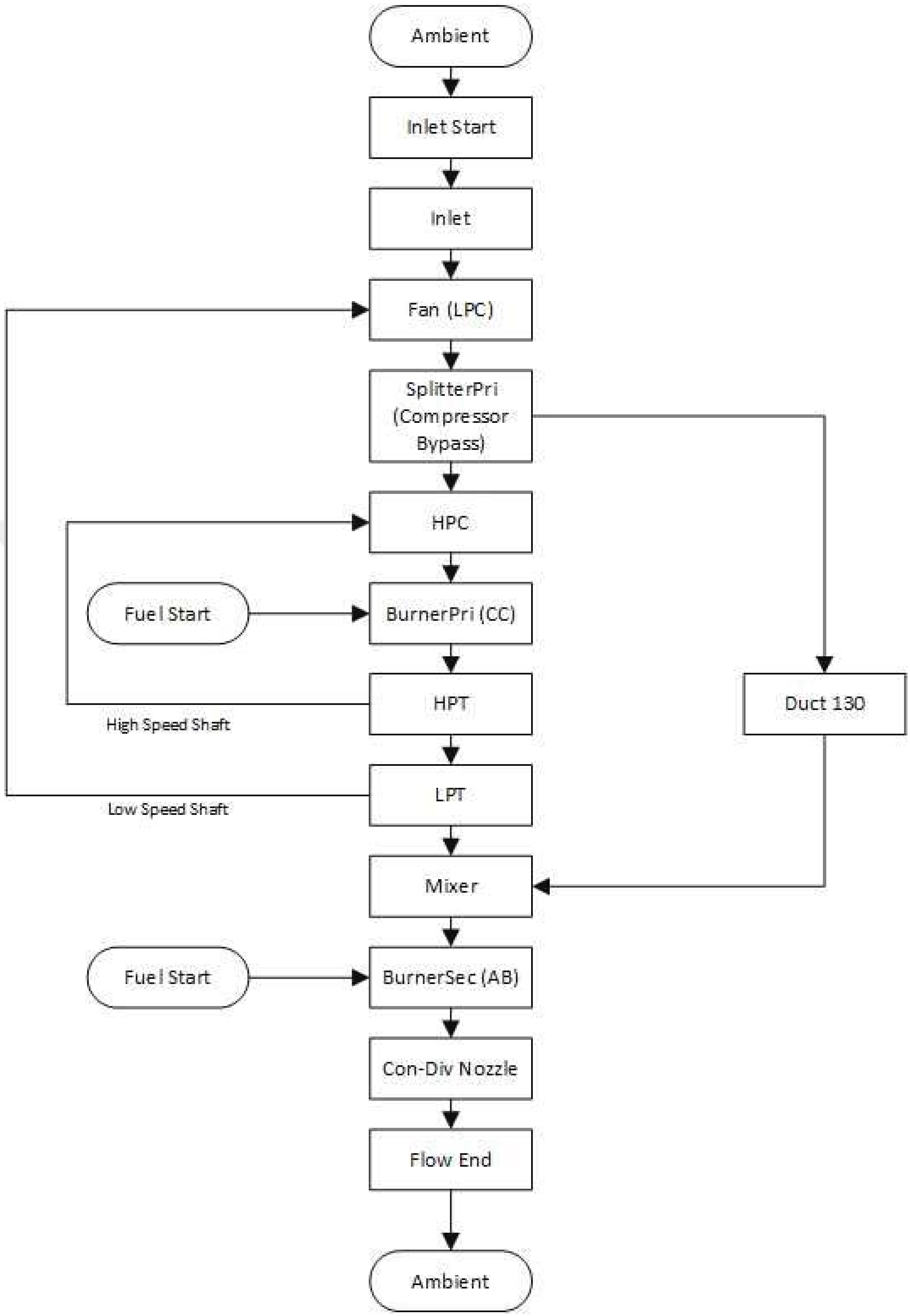

Figure 27 Mixed Flow Low Bypass Turbofan Engine NPSS Flowchart

The F-22 is the first operational fifth-generation aircraft with excellent manoeuvrability, supercruise, and stealth capabilities. Figure 26 depicts the F119-PW-100 cutaway. The overall installation of the propulsion system strives to maximize net propellant force while meeting compatibility requirements for both the intake and nozzle. An F119-PW-100 engine powers the F-22 aircraft, a twin-spool augmented turbofan with a thrust rating of 35000 lbs. The engine features are three-stage fan, a six-stage compressor, a single-stage HPT, and a single-stage LPT. The OPR value is 1:35, the BPR value is 0.3, and the FPR value is 5.0 (Mattingly, Heiser, & Pratt, Aircraft engine design, 2002).

4.2. Aircraft Aerodynamic Data

This study does not include the generation of aerodynamic data for the F-22 fighter. Instead, essential aerodynamic data is gathered from the literature (Brandt, 2018), which estimates the F-22's overall drag coefficient at an altitude of 40000 feet, as shown in Figure 28. This data is fed into an in-house tool that calculates the supercruise capability based on the installed engine performance results. To achieve Mach 1.6 supercruise at 40000 feet, the propulsion system must deliver at least 97.86 kN installed thrust without the need for an afterburner (Brandt, 2018). The above statistics and figures are used to approximate the drag of an F-22 aircraft at an altitude of 40000 feet. Nonetheless, this required thrust cannot be specified directly to engine OEMs without considering propulsion system integration losses.

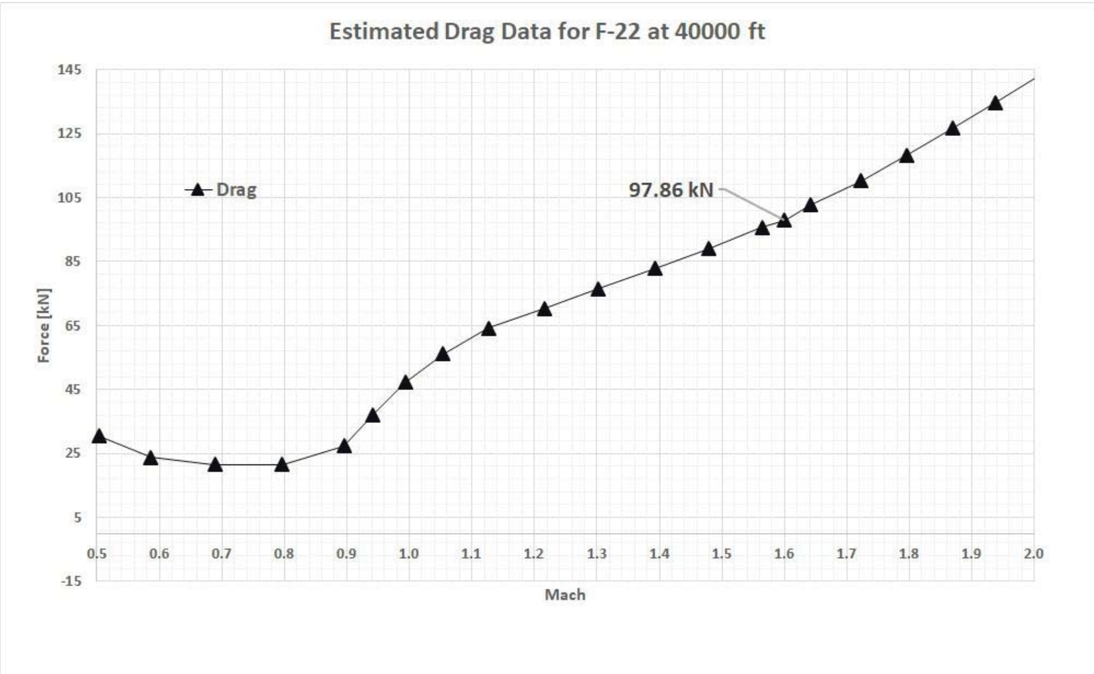

Figure 28 Estimated Drag for F-22 at 40000 ft

4.3. Inlet System Integration for F-22

The intake should deliver the engine's required mass flow rate with acceptable losses and efficiency. Additionally, it slows the free stream flow up to the engine face, owing to the engine fan's efficient operation at subsonic speeds.

Caret intake is preferred to supply enough amount of air for the F119-PW-100 engine. Figure 29 illustrates the components of the F-22's full-scale intake system (SAE, 2016). The inlet should be sized to deliver the modelled engine's maximum corrected air mass flow of 145 kg/s to attain comparable performance. Furthermore, as a design point, a high subsonic speed is chosen above a supercruise point to achieve the best engine performance across the flying envelope.

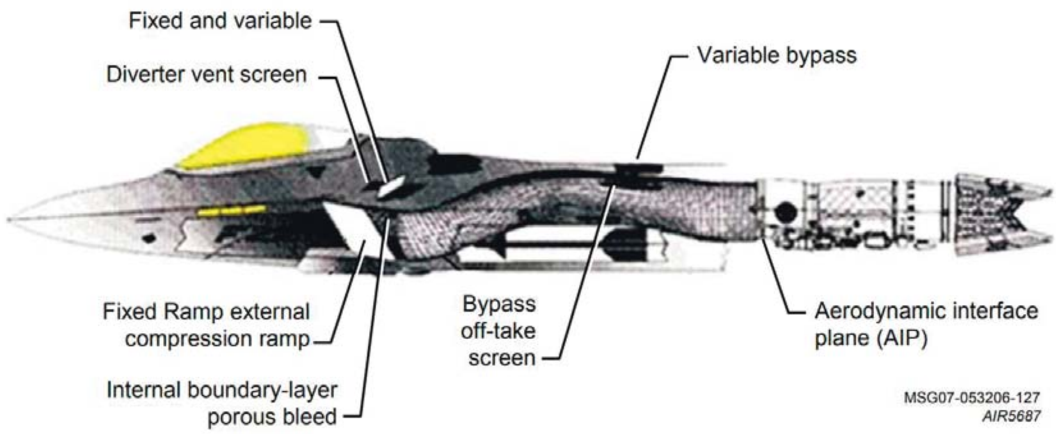

Figure 29 Full-Scale Intake Model of F-22 Aircraft (SAE, 2016)

For high intake performance, free stream air should attain the maximum possible total pressure at the engine face. Another critical consideration for supersonic intake is spillage drag. To reduce spillage drag, minimizing the throat area is the key design consideration. However, the intake throat should not choke in any flight conditions. Hence, critical throat Mach number is selected as 0.75 Mach, and maximum engine demand which is 145 kg/s maximum corrected air mass flow, taking into account to size intake as,

$$\left(\frac{W * T^{0.5}}{A * P}\right)_t = \left(\frac{W * T^{0.5}}{A * P}\right)_2 * \left(\frac{P_{T2}}{P_{Tt}}\right) * \left(\frac{A_2}{A_t}\right) \tag{4.1}$$

4.3.1. Pressure recovery

Typically, an air intake's internal efficiency is expressed in terms of its average total pressure recovery denoted as PqP, defined as the total-pressure ratio, $\frac{P_{02}}{P_{01}}$. In military aircraft, the standard for intake total-pressure recovery is the American Military Specification, MIL-E-5008. Some modern combat aircraft's pressure recovery tables and standard values are presented in Figure 30 (Cumpsty & Heyes, 2015).

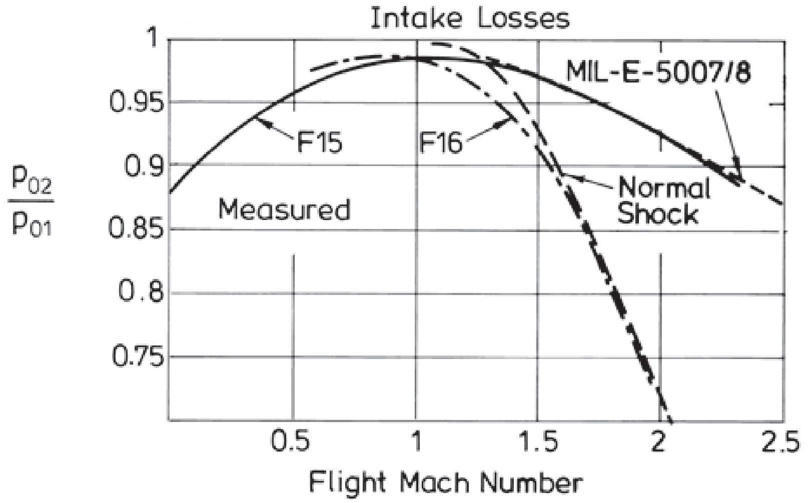

Figure 30 Inlet Pressure Recovery for F-15 and F-16 (Huenecke, 1987)

The intake pressure recovery table utilized in this study was developed by taking an aircraft such as the F-22 into the intake program. The table was applied to the NPPS, and the installed engine performance result was subtracted for all flight situations. Appendix A contains the table that was prepared.

4.3.2. Boundary Layer Bleed Drag

While bleeding at the intake can help mitigate the boundary layer, it also generates drag owing to momentum loss. With a well-designed bleed system, these losses can be recovered at the point of bleed outflow. A suitable starting point is to select 0.3 to 0.7 percent recoverable bleed momentum loss during the conceptual design phase.

$$D_{bleed} = 0.4 * \left(\frac{W_{bleed}}{W_{2corr}}\right) * W_{corr} * V_0 \tag{4.2}$$

Thus, 40% of bleed momentum loss is recovered at the bleed system's departure for this study and is included in Appendix A. For intake of F-22-like aircraft, the $\frac{W_{bleed}}{W_{2corr}}$ ratio should be between 0.01 and 0.07.

4.3.3. Spillage drag

Spillage drag is the additional drag caused by an engine producing more mass flow than the engine requires under given flight conditions. It is sometimes described as the total intake lip suction and additive drag, as discussed in Section 2.1.4. In general, engines require less air mass flow rate for sub military power lever angle operations; yet, the intake provides high mass flow rates due to the throat and capture area's design conditions. Bypass air before the engine fan can help to reduce this additional drag.

However, bypass air results in an additional loss of momentum. These two drags, spilling and bypass, are a function of PLA, and the engineer should design with the spillage drag and bypass drag trade-off in mind (Bowers, 1985). Figure 31 illustrates the characteristics of throttle-dependent drags.

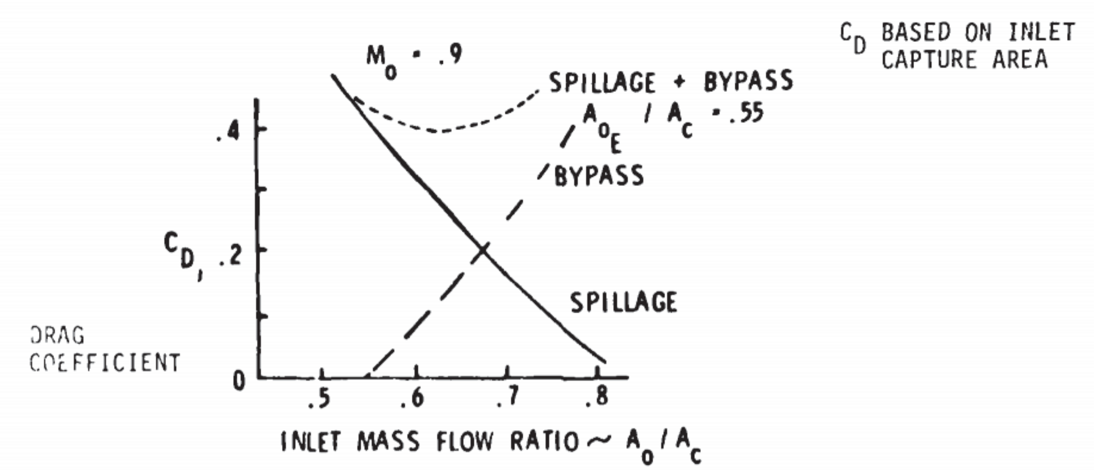

Figure 31 Trade-off Spillage and Bypass Drag (Bowers, 1985)

The drag caused by spillage is estimated as a function of the Mach number, the ratio of free stream tube area and capture area, A_0/A_c, and the corrected mass flow, Wc. The intake capture area is estimated using the throat area and a 145 kg/s air mass flow rate to meet engine demand. A_0/A_c presented in Appendix B as a function of Mach and mass flow rate and optimum spill drag table presented in Appendix C.

4.3.4. Nozzle System Integration for F-22

Although zero-lift drag is supposed to include no afterbody pressure drag for subsonic speeds, it also includes skin friction drag for the entire vehicle. The afterbody is defined as the 71.5 percentage length of the fuselage aft and the tail booms (Odis C. Pendergraft, 1979). Figure 32 depicts the area of the vehicle covered by the afterbody drag dataset.

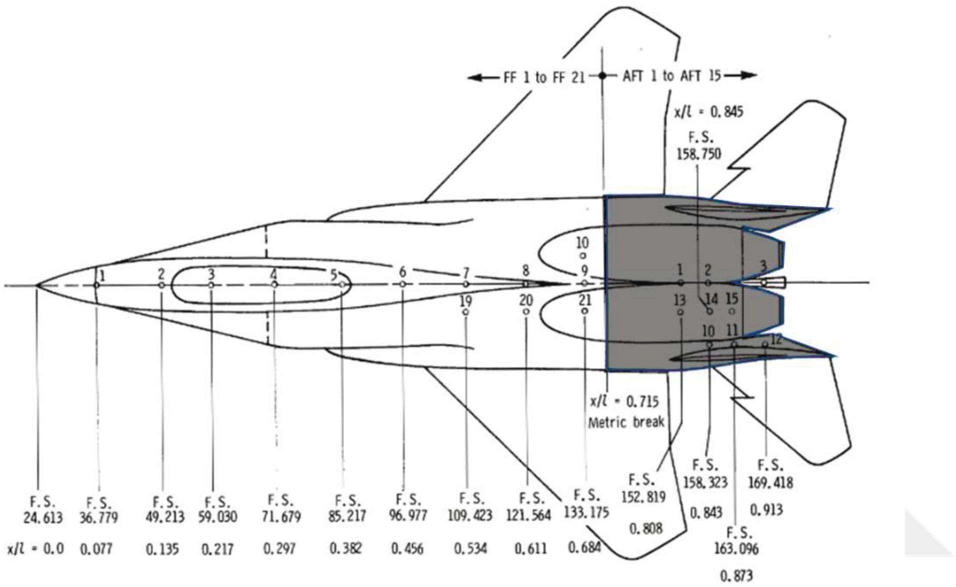

Figure 32 F-15 Subsonic Afterbody Drag Region (Pendergraft, 1979)

For supersonic speeds, zero-lift drag is considered to include no nozzle or annular base drag but includes drag of the afterbody front of the boattail nozzle interference plane and tail booms, which can be assumed to be independent of NPR at supersonic speeds (Odis C. Pendergraft, 1979). Figure 33 depicts the area of the vehicle covered by the afterbody drag dataset.

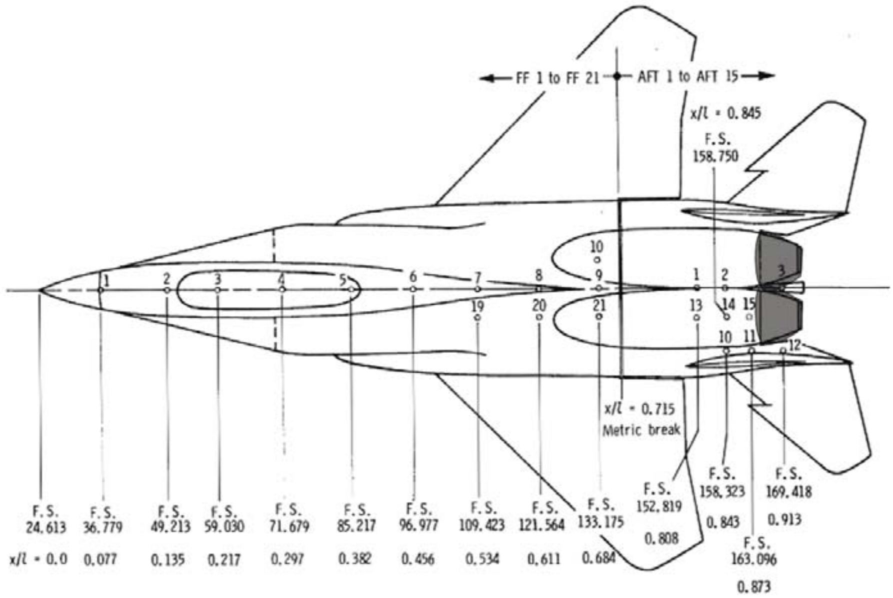

Figure 33 F-15 Supersonic Afterbody Drag Region (Odis C. Pendergraft, 1979)

Figure 34 presents the various nozzle configurations of F-15 aircraft. (Pendergraft, 1979). All linear measurements are in centimetres. The F-15 nozzle size values were scaled and made acceptable for the F22 nozzle. As a result, the drag contribution of the nozzle/afterbody in the study of "Fuselage and Nozzle Pressure Distributions on a 1/12-Scale F-15 Propulsion Model at Transonic Speed "was similarly scaled (Pendergraft, 1979).

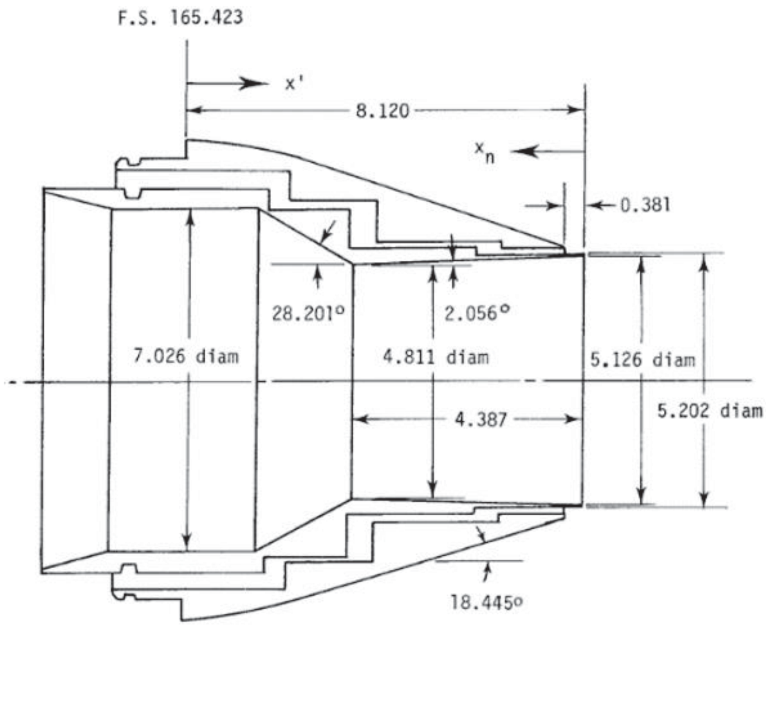

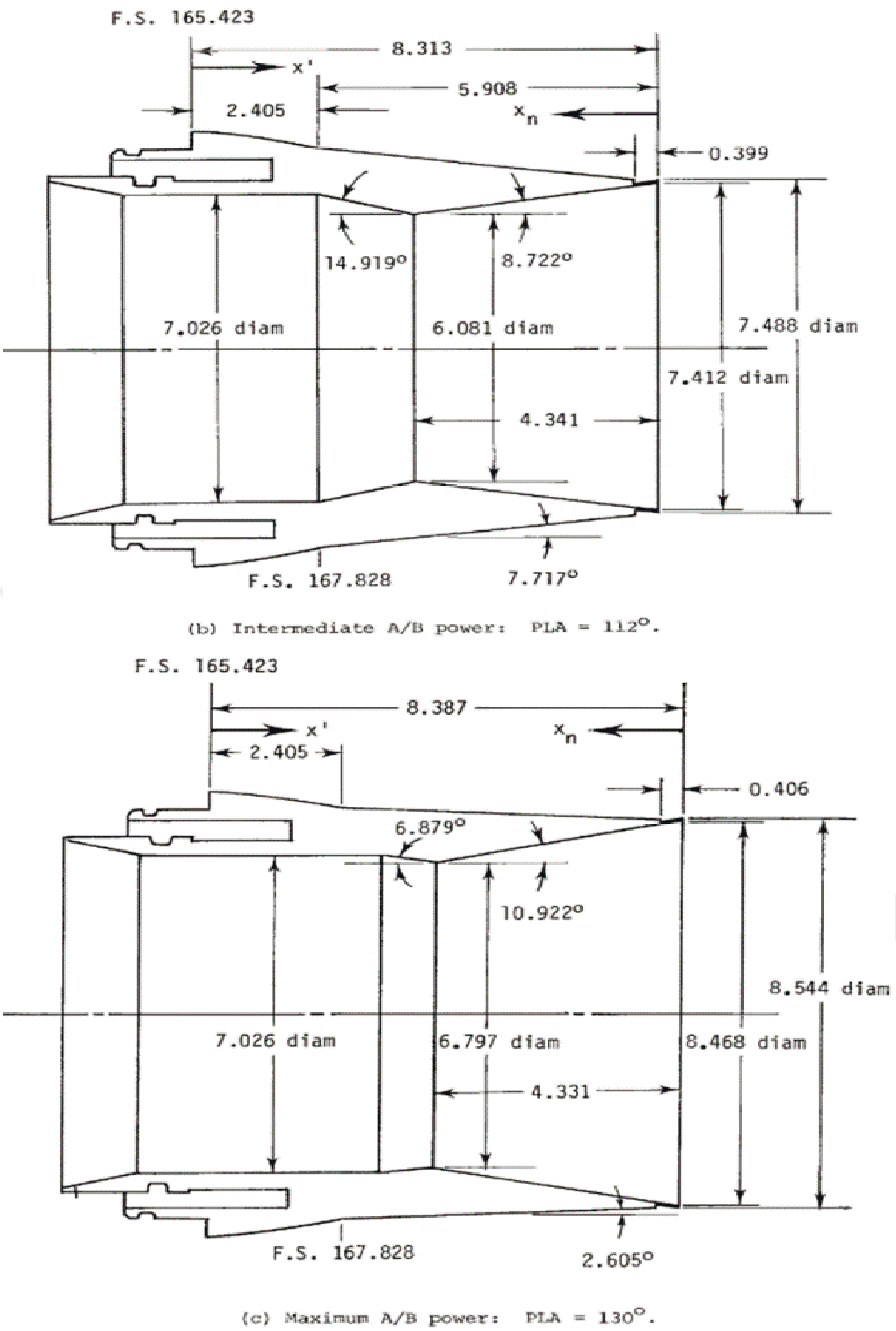

Figure 34 Schematic representations of the various nozzle configurations of F-15 aircraft (Pendergraft, 1979)

4.3.5. Boattail drag

The nozzle moving causes this drag increase during the flight as a function of the NPR, boattail angle, and Mach number. Figure 18 illustrates the boattail angle and other critical characteristics. In addition, during the flight, the nozzle throat and exit areas contract and expand to increase the exit velocity.

Boattail drag can be computed empirically. The boattail drag coefficients as a function of NPR and boattail angle were tabulated according to NASA's technical report and discussion in Section 2.1.4 and presented in Appendix D.

4.3.6. Base drag

This drag increase is caused by the nozzle moving during the flight due to the NPR, boattail angle, and Mach. It is a drag due to the small space between the nozzle exit's outer and inner diameters. The base drag coefficient is dependent on the NPR, the boattail angle, and the Mach number. Additionally, boundary layer characteristics affect base drag.

Devised correlation methodology to study the propulsive jet's impacts represents 2D nozzle drag (Hughes & McDonald, 1965). The methodology is designed for annular base nozzles; however, the same methodology is used for 2D nozzles for this thesis. Pendergraft's technical report (Pendergraft, 1979) results are matched with Figure 35 to calculate two-dimensional nozzle drag coefficients. Hence, it offers more precise two-dimensional nozzle drag coefficients (Hughes & McDonald, 1965).

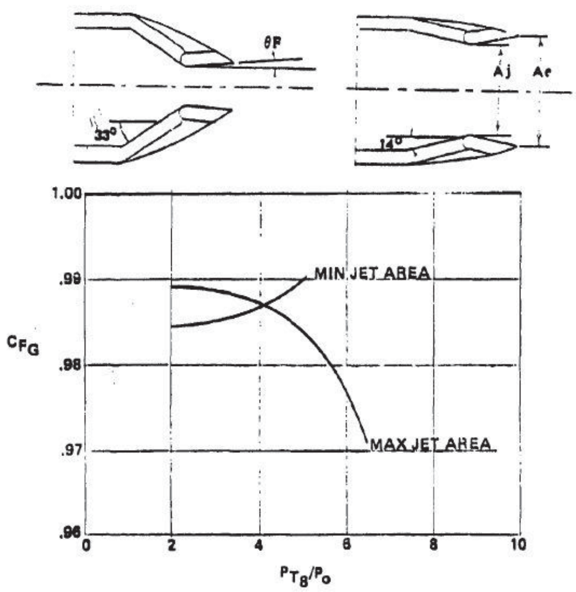

Figure 35 Effect of Aspect Ratio and Wedge Half-Angle on Base Drag of a 2D (McDonald & P. Hughest, 1965)

4.3.7. Interference drag

Two-engine aircraft, such as the F-22, generates more drag than a single-engine aircraft. This additional drag is caused by the interaction of two bodies in a single stream. Interference drag is proportional to the engine's diameter and the engine spacing between its centre to centre distances. Engine separation has a distinct effect on the afterbody in subsonic and supersonic flow regimes. Figure 20 illustrates drag shifts caused by engine spacing, a critical design parameter for twin-jet aircraft. The NASA technical report carried out the computations. Additionally, the engine spacing correlation shown in Figure 20 was used to perform the calculations (Pendergraft, 1979).

4.4. Result

The approaches developed for aircraft and engine integration have been used for an NPSS-based F119-PW-100 engine. The drag forces created by the engine's integration with the intake and nozzle selected for the F-22 aircraft were reduced from the engine's net force during the conceptual design phase. Thus, the force acting on the aircraft was calculated very early in the design process to provide accurate installed engine performance data. Without using afterburners, the F-22 fighter can supercruise at an altitude of 40000 feet at a speed of Mach 1.6 (Brandt, 2018).

At the conceptual design stage, the results of this analysis indicate that the F-22 aircraft can supercruise at a speed of Mach 1.62 at 40000 feet altitude. At 40000 feet, Figure 36 provides computed intake and nozzle-related losses. Figure 37 depicts the F-22 aircraft's thrust and drag curves, which intersect at Mach 1.62.

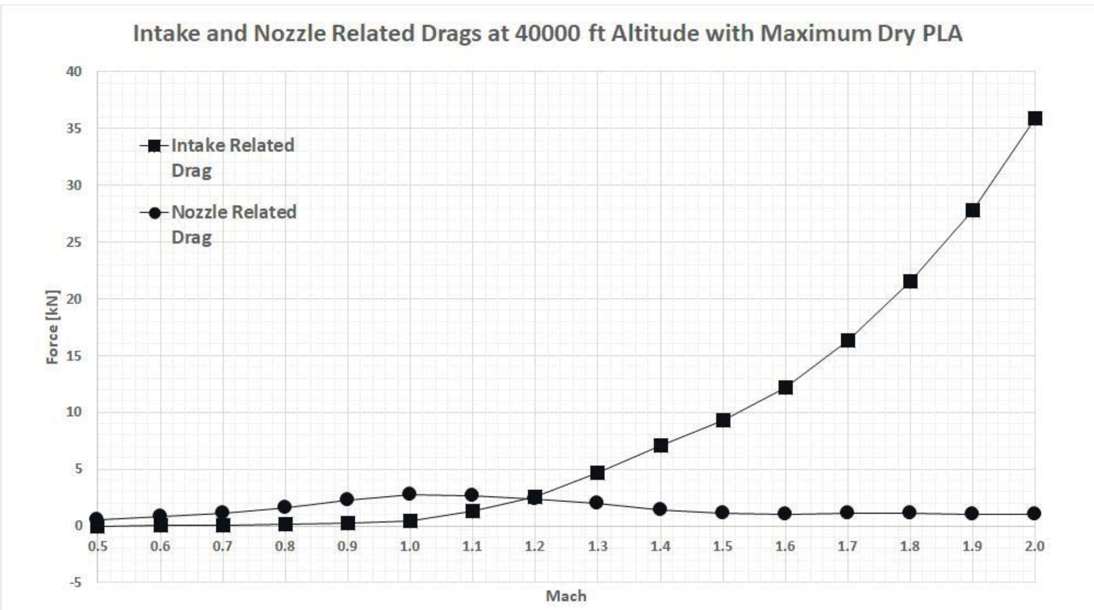

Figure 36 Intake and Nozzle Related Drags at 40000 ft Altitude with Maximum Dry PLA Setting

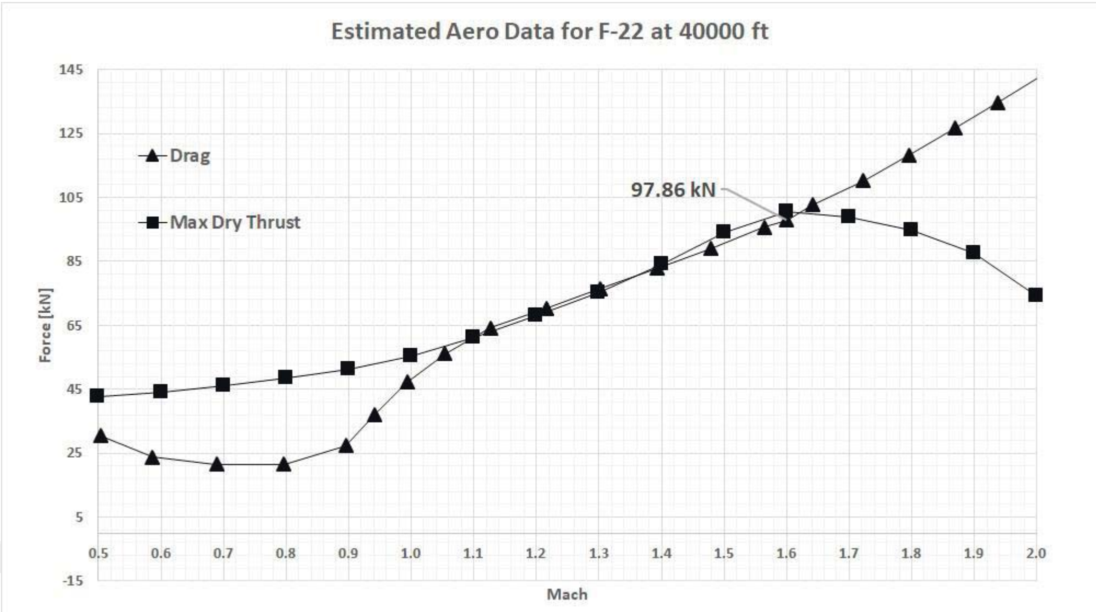

Figure 37 Net Propulsive Force and Drag Curves for F-22 Aircraft

5. CONCLUSION

The purpose of this study was to undertake a theoretical propulsion system integration research to develop accurate spillage drag, and boundary layer bleed drag, bypass drag, nozzle base drag, and boattail drag calculations. In-house code was developed in Python 3 to facilitate integration with existing MDAO tools. The tool enables early design phase exploration of a broad design space for aircraft-engine combination with precise loss estimates.

In this thesis, the external flow affecting the propulsion system and the aircraft is modelled to change by the altitude, Mach number and day conditions specified in ISA standards. However, it is assumed that the aircraft always flew with zero degrees AoA and AoS. Even if this situation represents the straight flight of the plane well, when the manoeuvres are examined in detail, deviations from the actual values are observed. A model should be developed with CFD and test data suitable for different angle of attack (AoA) and angle of sideslip (AoS) values. Total pressure variation and jet velocity are taken into account for intake and nozzle internal flow. However, the jet temperature must also be taken into account to meet the low visibility demands of new generation military aircraft and incorporate this into the optimization process.

Aircraft geometry is an important parameter that affects engine integration and related losses. However, aircraft geometry is not included during the thesis work, as it was based on the assumption of a design phase whose aircraft geometry has not yet been clarified. In particular, a detailed rear body design is required to reveal the effects of rear body integration and scrubbing drag. Therefore, the interaction of the rear fuselage and the jet flow is not included in this study.

In the thesis, a 2D intake assumption is modelled for losses due to inlet geometry. The effects of the intake capture area, throat area, wedge angle and duct losses on motor performance are included. However, the modelling does not include bump intake structure similar to intake of the F-35 aircraft losses due to 3D effects. CFD can model losses related to the 3D intake structure, and test results and thesis studies can be developed.

Circular nozzle, nozzle outlet area, nozzle throat area and nozzle maximum area are used for modelling. The movement of the nozzle blades is included in the model depending on the boattail angle and base area. The works of McDonald & P. Hughest are used as a reference to represent the 2D sized nozzle. In general, the inclusion of the described parameters in the thesis study is presented in Figure 38.

		Parameter	Unit	Abrreviation	Calculations
FLOW	External Flow	Altitude	m	Alt	Yes
		Mach Number	-	M	Yes
		Angle of Attack	deg	AoA	No
		Angle of Sideslip	deg	AoS	No
		Reynold Number	-	Re	No
		ISA Day Conditions	K	ISA	Yes
	Internal Flow	Inlet Fan Cooling	K	-	No
		Pressure Recovery	-	PqP	Yes
		Nozzle Pressure Ratio	-	NPR	Yes
		Jet Mach Number	-	M9	Yes
		Jet Temperature	K	T9	No
GEOMETRY	Aircraft Geometry	Afterbody Geometry	-	-	No
		Cross Section Area Distribution	-	-	No
		Tail Deflection	-	-	No
	Inlet Geometry	Capture Area	m^2	Ac	Yes
		Intake Throat Area	m^2	At	Yes
		Wedge Angle	deg	alpha	Yes
		3D Effects	-	-	No
		Duct Friction	-	-	Yes
		Duct Bending	deg	-	No
	Nozzle Geometry	Boattail Angle	deg	B	Yes
		Base Area	m^2	Ab	Yes
		Base Thickness	m	Tb	Yes
		Nozzle Throat Area	m^2	A8	Yes
		Nozzle Exit Area	m^2	A9	Yes
		Nozzle Spacing	m	s	Yes
		Nozzle Maximum Area	m^2	Amax	Yes

Figure 38 Parameters considered in the thesis study

The method described in this thesis is one way of accounting for installation effects in supersonic aircraft. Additionally, the concept works for aircraft with conventional shock inlets or oblique shock inlets flying at speeds up to 2.5 Mach. The equation implementation in NPSS enables aircraft manufacturers to calculate the influence of installation effects on engine performance. The verification phase demonstrates that the Python code outputs appropriately correspond to the NPSS outputs. In conjunction with the validation results, the acceptance of a correct implementation into NPSS might be declared. By simulating a defined aircraft engine model in NPSS using the developed approach, the magnitudes of the external drags will be represented as intended. This permits additional research into how these drags might be reduced, hence increasing the total net thrust.

This thesis reveals the losses of propulsion system integration during the conceptual design of a fighter jet. Losses due to propulsion system integration need to be accurately incorporated into the early design stage to meet the increasing performance needs of military aircraft. During the thesis, losses caused by intake and nozzles were theoretically revealed. By the theories, these losses were implemented in the Python language. Boeing's work validated the calculations for the F4 fighter aircraft. The 5th generation fighter aircraft engine F119-PW-100 was modelled with NPSS. Installed thrust was produced by adding intake and nozzle losses to the modelled turbofan engine. Thrust-drag curve is generated by comparing the installed thrust values with the F-22 drag curve. The results adequately represented in the service the F-22 results.

Future studies will augment this tool with computational fluid dynamics (CFD) simulations to represent various intake and nozzle configurations. Additionally, the tool will be connected with MDAO tools to produce a more accurate conceptual design outcome.

REFERENCES

Anderson, J. D. (2010). *Fundamentals of aerodynamics.* Tata McGraw-Hill Education.

Anderson, J. D. (2004). *Modern Compressible Flow With Historical Perspective, 3rd ed.* New York, USA: McGraw-Hill Education.

Ball, W. H. (1972). *Volume 1. Engineers Manual Propulsion System Installation Corrections,* . 1972.: The Boeing Company.

Ball, W. H. (1972). *Volume 2. Programmers Manual Propulsion System Installation Corrections.* . Ohia: The Boeing Company.

Ball, W. H. (1972). *Volume 3 Sample Cases Propulsion System Installation Corrections.* . Ohio: The Boeing Company.

Ball, W. H. (1972). *Volume 4. Bookkeeping Definition Propulsion System Installation Corrections.* . Ohio: The Boeing Company.

Ball, W. H. Hickcox, T. E. (1978). *Rapid Evaluation of Propulsion System Effects.* Ohio: Air Force Wright Aeronautical Laboratories.

Ball, W., & Hickcox, T. (1978). *Rapid Evaluation of Propulsion System Effects. Volume I.* Seattle, WA: Boeing Aerospace.

Bowers, D. L. (1985). *Throttle Dependent Forces-A Primer Tech.* Air Force Wright Aeronautical Labs.

Brandt, S. A. (2018). *The Effect of Initial Engine Sizing on Fighter Aircraft Final Optimized Size and Cost.* Aviation Technology.

Cawthon, J., & Truax, P. (1973). *Supersonic Inlet Design and Airframe-Inlet Integration.* AFFDL.

Cengel, Y. A., & Boles, M. A. (2007). *Thermodynamics: An Engineering Approach 6th Editon (SI Units).* New York: The McGraw-Hill Companies, Inc.

Cumpsty, N., & Heyes, A. (2015). *Jet propulsion.* Cambridge University Press.

El-Sayed, A. F. (2016). *Fundamentals of aircraft and rocket propulsion.* Springer.

Gertler, J. (2013). *Air Force F-22 Fighter Program.* Congressional Research Service.

Goldsmith, E., & Seddon, J. (1993). *,Practical Intake Aerodynamic Design.* AIAA Education Series.

Hoerner, S. F. (1950). Base Drag and Thick Trailing Edges. *Journal of the Aeronautical*, 622-628.

Hoerner, S. F. (1951). *Aerodynamic Drag.* Dayton, USA: The Otterbein Press.

Huenecke, K. (1987). *Modern combat aircraft design.* Naval Inst Press.

Hughes, P., & McDonald, H. (1965). A correlation of high subsonic afterbody drag in the presence of a propulsive jet or support sting. *Journal of Aircraft*, 202-207.

Karaselvi, E. (2018). *Modeling of Propulsion And Thermal Systems Of Military Vehicles For Conceptual Design.* 2018: Istanbul Technical University.

Kurzke, J. (2001). GasTurb 9 Users Manual. *A Program to Calculate Design and Off-Design Performance of Gas Turbines}.*

Lockheed Martin (2020). *F35 Lightning II*. Retrieved from https://www.f35.com/f35/index.html

Mattingly, J. D., & Boyer, K. M. (2006). *Elements of Propulsion: Gas Turbines and Rockets American Institute of Aeronautics and Astronautics.* VA.

Mattingly, J. D., Heiser, W. H., & Pratt, D. T. (2002). Aircraft engine design. *American Institute of Aeronautics and Astronautics*.

McDonald, H., & P. Hughest (1965). A Correlation of High Subsonic Afterbody Drag in the Presence of a Propulsive Jet or Support Sting. *Journal of Aircraft*, 202-207.

Munson, B. R. (2012). *Fundamentals of Fluid Mechanics.* Wiley-Blackwell.

Munson, B. R. (2013). *Fluid mechanics.* Singapore: Wiley .

NASA (2019). *The History of NASA's Sonic Boom Research*. Retrieved from www.nasa.gov: https://www.nasa.gov/sites/default/files/atoms/files/supersonic-student.pdf

NASA (2021). *Aerodynamics Index Glenn Research Center*. Retrieved from Isentropic Flow: https://www.grc.nasa.gov/www/k-12/airplane/isentrop.html

NASA (2021). *Compressible Aerodynamics Index*. Retrieved from Normal Shock Wave: https://www.grc.nasa.gov/www/k-12/airplane/shortc.html

Odis C. Pendergraft, J. (1979). *Fuselage and Nozzle Pressure Distributions on a 1/12-Scale F-15 Propulsion Model at Transonic Speed.* Virginia: NASA.

Pendergraft, O. C. (1979). *Fuselage and nozzle pressure distributions on a 1/12-scale F-15 propulsion model at transonic speeds.* Hampton, VA, United States: NASA Langley Research Center .

Rooney, E. (1985). *Thrust-Drag Accounting Methodology," in Thrust and Drag: Its Predictionand Verification.* New York: AIAA.

SAE (2016). *Inlet Engine Compatibility – From Model to Full Scale Development.* Aerospace Information Report 5687, Rev. A, SAE.

Sanders, N. D. (1946). *Performance Parameters for Jet Propulsion Engines.* Ohio: Aircraft Engine Research Laboratory.

Schumacher, H., & Trent, W. (1972). *Significant Considerations in the Development of Engine/Airframe Systems for High Performance Aircraft.* AIAA.

Seddon, J., & Goldsmith, E. L. (1999). *Intake aerodynamics.* Boston: Blackwell science .

Walsh, P. P., & Fletcher, P. (2004). Design Point Performance and Engine Concept Design. *Gas Turbine Performance, 2nd ed.; Blackwell Science Ltd.: Oxford, UK.*

APPENDICES

APPENDIX A: Intake + Duct Pressure Recovery (PT2/PTo)

APPENDIX B: A0/AC as a function of Mach and Mass Flow Rate

APPENDIX C: Cdspill as a function of Mach and A0AC

APPENDIX D: Afterbody Drag Coefficients as a function of Mach and NPR

APPENDIX E: Drag coefficient of the boattail at NPR = 2.5 for subsonic speeds

APPENDIX F: Correction for boattail drag when NPR ≠ 2.5

APPENDIX G: Correlation of circular nozzle base pressures at supersonic speeds

APPENDIX H: Ratio of reference base pressures

APPENDIX I: Drag coefficient for engine interfrence

APPENDIX J: Spillage drag coefficient for A0AC ratio, J79 Engine

APPENDIX K: Spillage drag coefficient for A0AC ratio, Normal Shock Intake

APPENDIX L: Spillage drag coefficient for A0AC ratio, Normal Shock Intake

APPENDIX M: Bleed Mass Flow Ratio, External Compression Inlet

APPENDIX N: Bleed Mass Flow Ratio, J-79 Engine

APPENDIX O: F15 Based Drag Assumption

APPENDIX P: F15 Based Drag Calculation

APPENDIX R: Spill Drag Calculation

APPENDIX S: Boattail Drag Calculation

APPENDIX T: Interference Drag Calculation

APPENDIX A: Intake + Duct Pressure Recovery (PT2/PT0)

		Mass flow (kg/s)										
	Wc	45	55	65	75	85	95	105	115	125	135	145
Mach	0.00	0.9638	0.9364	0.9454	0.9221	0.9056	0.9045	0.8906	0.8289	0.8072	0.7895	0.7606
	0.10	0.9590	0.9661	0.9399	0.9489	0.9134	0.9014	0.8651	0.8414	0.7948	0.7814	0.7808
	0.20	0.9790	0.9578	0.9761	0.9816	0.9639	0.9626	0.9092	0.9280	0.8760	0.8887	0.8363
	0.30	0.9790	0.9478	0.9462	0.9439	0.9709	0.9448	0.9256	0.9130	0.9246	0.8955	0.8924
	0.40	0.9790	0.9777	0.9860	0.9737	0.9412	0.9477	0.9633	0.9634	0.9407	0.9421	0.9134
	0.50	0.9790	0.9478	0.9860	0.9439	0.9511	0.9773	0.9438	0.9584	0.9211	0.9244	0.9165
	0.60	0.9590	0.9678	0.9661	0.9638	0.9412	0.9773	0.9438	0.9389	0.9233	0.9391	0.9340
	0.70	0.9690	0.9877	0.9860	0.9439	0.9511	0.9576	0.9536	0.9291	0.9525	0.9391	0.9154
	0.80	0.9690	0.9877	0.9562	0.9539	0.9610	0.9477	0.9634	0.9487	0.9622	0.9487	0.9154
	0.90	0.9790	0.9578	0.9462	0.9539	0.9610	0.9576	0.9536	0.9291	0.9233	0.9487	0.9443
	1.00	0.9590	0.9777	0.9661	0.9737	0.9511	0.9675	0.9733	0.9682	0.9525	0.9487	0.9443
	1.10	0.9436	0.9622	0.9506	0.9583	0.9555	0.9620	0.9676	0.9238	0.9373	0.9241	0.9294
	1.20	0.9584	0.9473	0.9653	0.9336	0.9602	0.9471	0.9430	0.9480	0.9420	0.9479	0.9149
	1.30	0.9672	0.9563	0.9545	0.9426	0.9206	0.9558	0.9229	0.9374	0.9125	0.8995	0.9330
	1.40	0.9312	0.9300	0.9380	0.9358	0.9235	0.9297	0.9164	0.9305	0.9153	0.8839	0.8890
	1.50	0.9070	0.9059	0.9229	0.9114	0.8902	0.8964	0.8833	0.8971	0.9006	0.8700	0.8748
	1.60	0.8589	0.8579	0.8923	0.8722	0.8518	0.8578	0.8808	0.8408	0.8355	0.8324	0.8633
	1.70	0.8315	0.8304	0.8290	0.8184	0.8504	0.8131	0.8438	0.8395	0.8089	0.7974	0.7936
	1.80	0.7912	0.7819	0.7970	0.7951	0.8011	0.7982	0.8029	0.7908	0.7777	0.7747	0.7712
	1.90	0.7626	0.7694	0.7448	0.7430	0.7409	0.7614	0.7581	0.7543	0.7344	0.7467	0.7431
	2.00	0.7084	0.7001	0.6916	0.6900	0.7170	0.6928	0.7042	0.6863	0.6891	0.6935	0.6762

APPENDIX B: A0/AC as a function of Mach and Mass Flow Rate

	Mass flow (kg/s)										
Wc	45	55	65	75	85	95	105	115	125	135	145
0.00	0.0000	0.0000	0.0000	0.0000	0.0000	0.0000	0.0000	0.0000	0.0000	0.0000	0.0000
0.10	0.7987	1.2068	1.5495	1.9753	2.2586	2.6275	2.8520	3.2184	3.3786	3.3815	3.5040
0.20	0.4107	0.6153	0.7939	1.0191	1.2257	1.3707	1.5580	1.7166	1.8377	1.9180	1.9908
0.30	0.2792	0.4183	0.5567	0.6799	0.8135	0.9727	1.0779	1.2085	1.3320	1.3827	1.4433
0.40	0.2182	0.3335	0.4349	0.5536	0.6423	0.7623	0.8674	0.9759	1.0481	1.0910	1.1309
0.50	0.1838	0.2811	0.3627	0.4618	0.5412	0.6357	0.7384	0.7931	0.9104	0.9301	0.9761
0.60	0.1596	0.2493	0.3217	0.3970	0.4950	0.5522	0.6284	0.7255	0.7847	0.8379	0.8553
0.70	0.1517	0.2273	0.3055	0.3657	0.4513	0.5140	0.6031	0.6546	0.7228	0.7481	0.7883
0.80	0.1424	0.2112	0.2811	0.3468	0.4282	0.4977	0.5664	0.6404	0.7000	0.7097	0.7401
0.90	0.1370	0.2052	0.2760	0.3406	0.4118	0.4886	0.5504	0.5972	0.6871	0.7186	0.7418
1.00	0.1400	0.2034	0.2707	0.3376	0.4124	0.4843	0.5400	0.6044	0.6811	0.6980	0.7203
1.10	0.1346	0.2081	0.2685	0.3348	0.4048	0.4804	0.5356	0.5994	0.6825	0.6850	0.7444
1.20	0.1383	0.2051	0.2759	0.3405	0.4116	0.4935	0.5616	0.6096	0.6801	0.7113	0.7493
1.30	0.1431	0.2166	0.2882	0.3484	0.4169	0.4846	0.5631	0.6238	0.7102	0.7204	0.7668
1.40	0.1500	0.2179	0.2930	0.3617	0.4374	0.5189	0.5726	0.6476	0.7224	0.7325	0.7717
1.50	0.1541	0.2310	0.3012	0.3833	0.4493	0.5116	0.6006	0.6722	0.7271	0.7843	0.8012
1.60	0.1584	0.2349	0.3159	0.3820	0.4618	0.5258	0.5984	0.6839	0.7395	0.7898	0.8319
1.70	0.1624	0.2383	0.3205	0.3915	0.4636	0.5389	0.6133	0.6937	0.7579	0.8178	0.8440
1.80	0.1645	0.2414	0.3248	0.4008	0.4845	0.5575	0.6345	0.7249	0.7922	0.8286	0.8729
1.90	0.1644	0.2464	0.3246	0.4176	0.4996	0.5749	0.6408	0.7398	0.7918	0.8456	0.8908
2.00	0.1658	0.2509	0.3375	0.4295	0.4931	0.5974	0.6661	0.7609	0.8401	0.8610	0.8792

APPENDIX C: Cdspill as a function of Mach and A0AC

Mach	0.40	Mach	0.50	Mach	0.60	Mach	0.70	Mach	0.80	Mach	0.85	Mach	0.90	Mach	0.95
A0AC	Cdspill	A0AC	Cdspill	A0AC	Cdspill	A0AC	Cdspill	A0AC	Cdspill	A0AC	Cdspill	A0AC	Cdspill	A0AC	Cdspill
1.0000	0.0000	1.0000	0.0000	0.9648	0.0000	0.8886	0.0000	0.8430	0.0000	0.8288	0.0000	0.8192	0.0000	0.8138	0.0000
0.9000	-0.0177	0.9000	-0.0247	0.9000	0.0035	0.8887	-0.0001	0.8430	0.0000	0.8288	0.0000	0.8192	0.0001	0.8138	0.0000
0.8000	-0.02394	0.8000	-0.03212	0.8000	-0.00649	0.8000	0.012051	0.8000	0.018025	0.8000	0.018437	0.8000	0.017776	0.8000	0.017716
0.7000	-0.0198	0.7000	-0.0266	0.7000	0.0024	0.7000	0.0248	0.7000	0.0348	0.7000	0.0383	0.7000	0.0401	0.7000	0.0427
0.6000	-0.0059	0.6000	-0.0076	0.6000	0.0271	0.6000	0.0569	0.6000	0.0725	0.6000	0.0771	0.6000	0.0831	0.6000	0.0895
0.5000	0.0176	0.5000	0.0226	0.5000	0.0656	0.5000	0.1045	0.5000	0.1247	0.5000	0.1348	0.5000	0.1424	0.5000	0.1476
0.4000	0.0853	0.4000	0.1012	0.4000	0.1524	0.4000	0.1634	0.4000	0.1935	0.4000	0.2050	0.4000	0.2103	0.4000	0.2224
0.3000	0.1873	0.3000	0.2107	0.3000	0.2828	0.3000	0.2931	0.3000	0.3026	0.3000	0.3174	0.3000	0.3296	0.3000	0.3074
0.2000	0.3223	0.2000	0.3513	0.2000	0.3879	0.2000	0.4167	0.2000	0.4438	0.2000	0.4579	0.2000	0.4631	0.2000	0.4035
0.1000	0.4781	0.1000	0.4651	0.1000	0.5087	0.1000	0.5285	0.1000	0.5564	0.1000	0.5823	0.1000	0.5915	0.1000	0.5053
0.0000	0.6138	0.0000	0.5985	0.0000	0.6388	0.0000	0.6758	0.0000	0.6980	0.0000	0.7129	0.0000	0.7352	0.0000	0.6275

Mach	1.05	Mach	1.20	Mach	1.40	Mach	1.60	Mach	1.80	Mach	2.00
A0AC	Cdspill	A0AC	Cdspill	A0AC	Cdspill	A0AC	Cdspill	A0AC	Cdspill	A0AC	Cdspill
0.8128	0.0000	0.8307	0.0000	0.8959	0.0000	0.9637	0.0000	1.0000	0.0000	1.0000	0.0000
0.8128	0.0000	0.8307	0.0000	0.8960	-0.0001	0.9000	0.0634	0.9000	0.0946	0.9000	0.1125
0.8000	0.0172	0.8000	0.0273	0.8000	0.0787	0.8000	0.1526	0.8000	0.2002	0.8000	0.2367
0.7000	0.0505	0.7000	0.0794	0.7000	0.1589	0.7000	0.2529	0.7000	0.3223	0.7000	0.3782
0.6000	0.1010	0.6000	0.1494	0.6000	0.2597	0.6000	0.3663	0.6000	0.4482	0.6000	0.5141
0.5000	0.1656	0.5000	0.2376	0.5000	0.3624	0.5000	0.4998	0.5000	0.5863	0.5000	0.6721
0.4000	0.2468	0.4000	0.3286	0.4000	0.4906	0.4000	0.6356	0.4000	0.7476	0.4000	0.8411
0.3000	0.3324	0.3000	0.4350	0.3000	0.6219	0.3000	0.7807	0.3000	0.8879	0.3000	1.0014
0.2000	0.4264	0.2000	0.5519	0.2000	0.7483	0.2000	0.9165	0.2000	1.0506	0.2000	1.1657
0.1000	0.5387	0.1000	0.6854	0.1000	0.8961	0.1000	1.0864	0.1000	1.2453	0.1000	1.3604
0.0000	0.6627	0.0000	0.8314	0.0000	1.0740	0.0000	1.2433	0.0000	1.4129	0.0000	1.5506

APPENDIX D: Afterbody Drag Coefficients as a function of Mach and NPR

15.86 **CD NOZZLE per air craft**

		Freestream Mach Number									
		0.4	0.6	0.8	0.9	1.05	1.2	1.4	1.6	1.8	2
NPR	1.5	0.22	0.25	0.30	0.36	0.48	0.42	0.37	0.32	0.29	0.22
	2	0.26	0.28	0.31	0.38	0.48	0.45	0.39	0.33	0.29	0.23
	3	0.28	0.30	0.32	0.40	0.55	0.49	0.40	0.36	0.31	0.25
	4	0.28	0.30	0.33	0.39	0.53	0.47	0.40	0.33	0.30	0.24
	5	0.28	0.29	0.31	0.38	0.50	0.44	0.37	0.32	0.30	0.24
	6	0.28	0.29	0.30	0.39	0.48	0.42	0.35	0.31	0.29	0.23
	7	0.29	0.30	0.30	0.39	0.45	0.40	0.33	0.29	0.27	0.22
	8	0.28	0.30	0.29	0.39	0.42	0.38	0.31	0.26	0.27	0.21
	9	0.29	0.29	0.30	0.39	0.40	0.36	0.28	0.23	0.24	0.19
	10	0.28	0.29	0.30	0.39	0.39	0.33	0.26	0.22	0.23	0.17
	11	0.29	0.28	0.30	0.39	0.38	0.32	0.24	0.20	0.20	0.15
	12	0.29	0.28	0.30	0.38	0.36	0.30	0.21	0.19	0.19	0.13

13.17 **CD NOZZLE per air craft**

		Freestream Mach Number									
		0.4	0.6	0.8	0.9	1.05	1.2	1.4	1.6	1.8	2
NPR	1.5	0.20	0.24	0.28	0.34	0.44	0.36	0.27	0.23	0.18	0.16
	2	0.23	0.26	0.29	0.35	0.43	0.37	0.28	0.24	0.20	0.17
	3	0.25	0.27	0.30	0.35	0.46	0.40	0.31	0.25	0.20	0.19
	4	0.22	0.27	0.31	0.36	0.44	0.39	0.30	0.23	0.20	0.18
	5	0.21	0.25	0.30	0.36	0.42	0.37	0.28	0.22	0.20	0.17
	6	0.20	0.24	0.29	0.36	0.43	0.35	0.26	0.21	0.18	0.17
	7	0.18	0.23	0.28	0.35	0.38	0.33	0.24	0.20	0.17	0.15
	8	0.16	0.22	0.28	0.35	0.37	0.30	0.22	0.18	0.16	0.14
	9	0.14	0.21	0.27	0.33	0.34	0.28	0.21	0.17	0.15	0.13
	10	0.13	0.20	0.28	0.33	0.30	0.26	0.19	0.15	0.14	0.13
	11	0.11	0.19	0.27	0.32	0.29	0.24	0.17	0.14	0.13	0.12
	12	0.09	0.18	0.27	0.32	0.26	0.21	0.16	0.12	0.12	0.10

9.59 **CD NOZZLE per air craft**

		Freestream Mach Number									
		0.4	0.6	0.8	0.9	1.05	1.2	1.4	1.6	1.8	2
NPR	1.5	0.20	0.23	0.25	0.29	0.26	0.22	0.18	0.14	0.15	0.14
	2	0.23	0.25	0.26	0.30	0.29	0.24	0.14	0.16	0.16	0.14
	3	0.23	0.25	0.27	0.30	0.32	0.28	0.21	0.17	0.17	0.15
	4	0.22	0.24	0.27	0.30	0.32	0.27	0.21	0.17	0.17	0.15
	5	0.22	0.23	0.26	0.29	0.30	0.26	0.19	0.16	0.16	0.15
	6	0.21	0.24	0.26	0.28	0.27	0.23	0.18	0.15	0.15	0.14
	7	0.20	0.22	0.26	0.26	0.22	0.20	0.17	0.14	0.14	0.13
	8	0.19	0.22	0.24	0.25	0.20	0.18	0.15	0.13	0.14	0.13
	9	0.18	0.21	0.24	0.24	0.19	0.16	0.14	0.13	0.13	0.12
	10	0.17	0.20	0.24	0.23	0.17	0.15	0.13	0.11	0.11	0.11
	11	0.16	0.20	0.23	0.21	0.16	0.14	0.11	0.10	0.10	0.10
	12	0.16	0.19	0.22	0.19	0.14	0.13	0.10	0.09	0.09	0.09

8.28 **CD NOZZLE per air craft**

Freestream Mach Number

		0.4	0.6	0.8	0.9	1.05	1.2	1.4	1.6	1.8	2
NPR	1.5	0.21	0.23	0.24	0.28	0.26	0.22	0.16	0.14	0.12	0.09
	2	0.22	0.24	0.26	0.28	0.28	0.23	0.18	0.15	0.12	0.10
	3	0.23	0.25	0.27	0.29	0.27	0.23	0.13	0.15	0.13	0.11
	4	0.23	0.24	0.25	0.28	0.25	0.22	0.17	0.14	0.12	0.11
	5	0.22	0.24	0.25	0.28	0.25	0.21	0.16	0.13	0.12	0.10
	6	0.21	0.23	0.25	0.26	0.22	0.18	0.14	0.12	0.11	0.09
	7	0.21	0.22	0.24	0.25	0.19	0.16	0.13	0.11	0.10	0.09
	8	0.20	0.22	0.24	0.24	0.17	0.15	0.12	0.10	0.09	0.08
	9	0.20	0.21	0.23	0.23	0.14	0.12	0.10	0.09	0.08	0.07
	10	0.19	0.21	0.22	0.21	0.12	0.11	0.08	0.08	0.07	0.06
	11	0.18	0.20	0.22	0.20	0.10	0.08	0.07	0.07	0.06	0.05
	12	0.18	0.19	0.21	0.19	0.07	0.06	0.05	0.05	0.05	0.04

0 **CD NOZZLE per air craft**

Freestream Mach Number

		0.4	0.6	0.8	0.9	1.05	1.2	1.4	1.6	1.8	2
NPR	1.5	0.22	0.22	0.21	0.21	0.01	0.01	0.01	0.01	0.01	0.01
	2	0.23	0.23	0.22	0.22	0.01	0.01	0.01	0.01	0.01	0.01
	3	0.24	0.23	0.23	0.22	0.02	0.02	0.02	0.01	0.01	0.01
	4	0.23	0.23	0.22	0.22	0.01	0.01	0.01	0.10	0.01	0.01
	5	0.22	0.23	0.22	0.21	0.01	0.01	0.01	0.01	0.01	0.01
	6	0.22	0.22	0.22	0.22	0.01	0.01	0.01	0.01	0.01	0.01
	7	0.21	0.22	0.21	0.21	0.01	0.01	0.01	0.01	0.01	0.01
	8	0.22	0.21	0.22	0.22	0.00	0.00	0.00	0.00	0.01	0.01
	9	0.21	0.21	0.21	0.22	0.00	0.00	0.00	0.00	0.00	0.00
	10	0.21	0.21	0.21	0.21	0.00	0.00	0.00	0.00	0.00	0.00
	11	0.20	0.21	0.21	0.21	0.00	0.00	0.00	0.00	0.00	0.00
	12	0.21	0.20	0.21	0.20	-0.01	-0.01	-0.01	0.00	0.00	0.00

APPENDIX E: Drag coefficient of the boattail at NPR = 2.5 for subsonic Mach values, Ball, W. H. (1972).

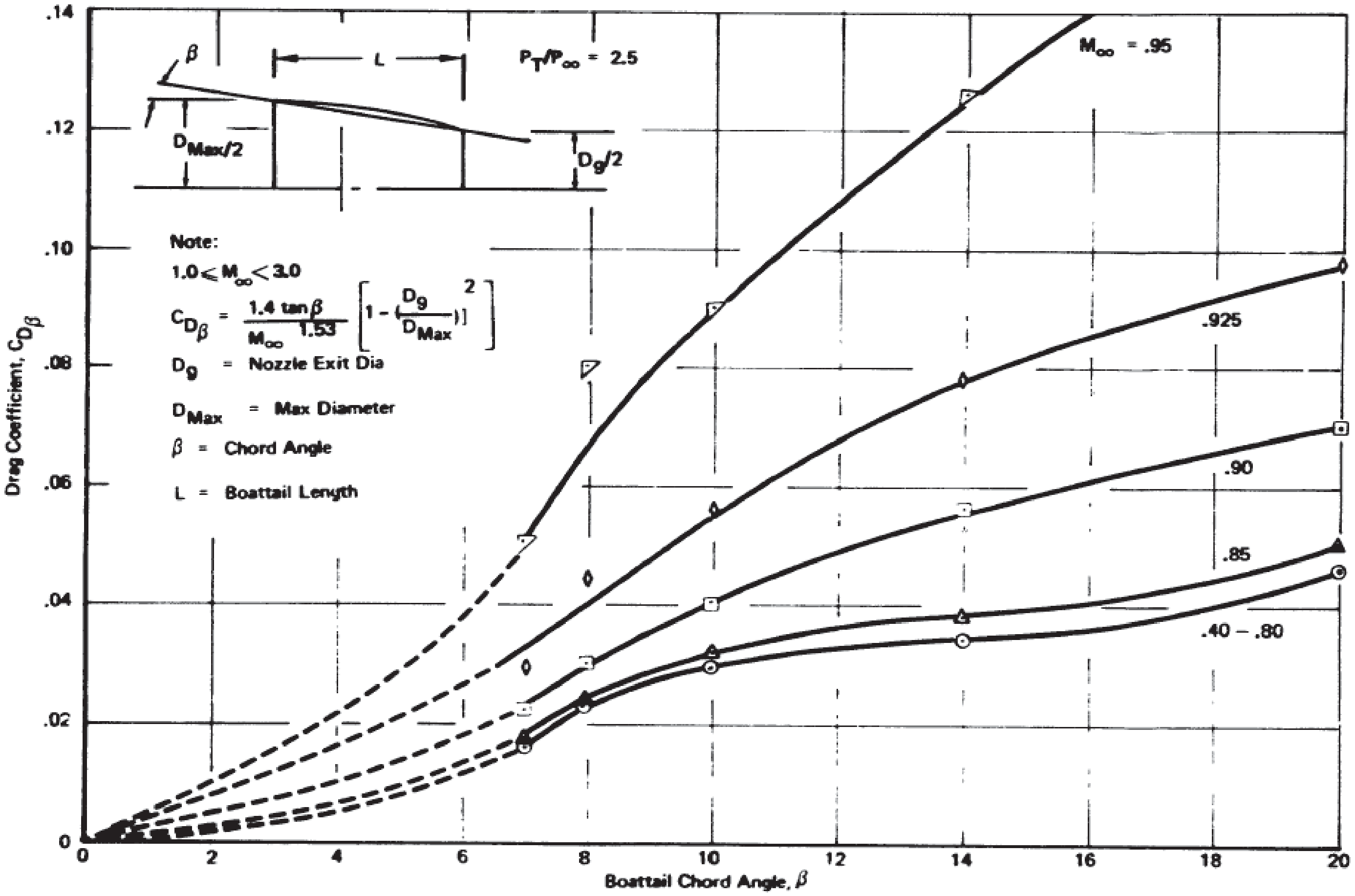

APPENDIX F: Correction for boattail drag when NPR ≠ 2.5 Ball, W. H. (1972).

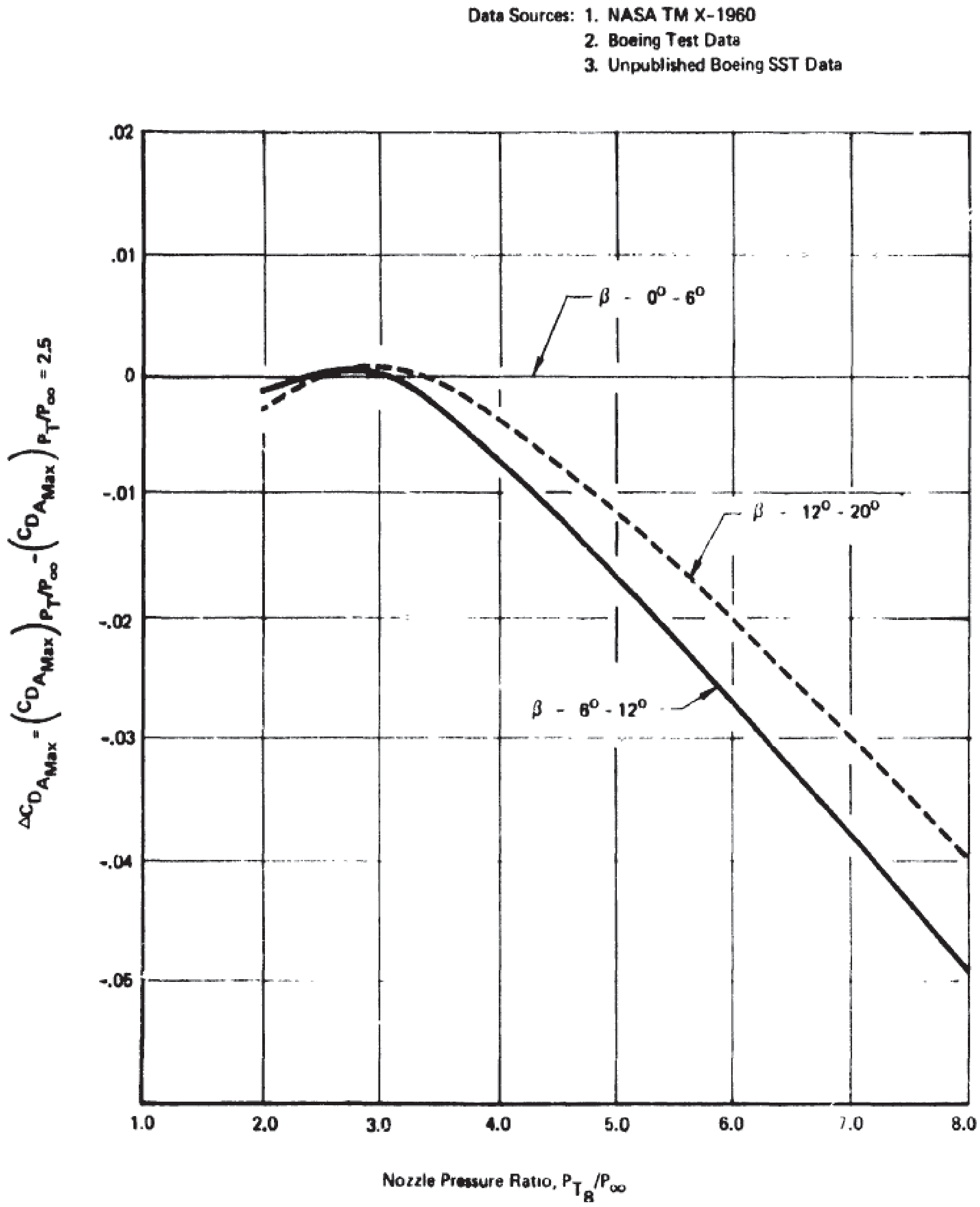

APPENDIX G: Correlation of circular nozzle base pressures at supersonic speeds, Ball, W. H. (1972).

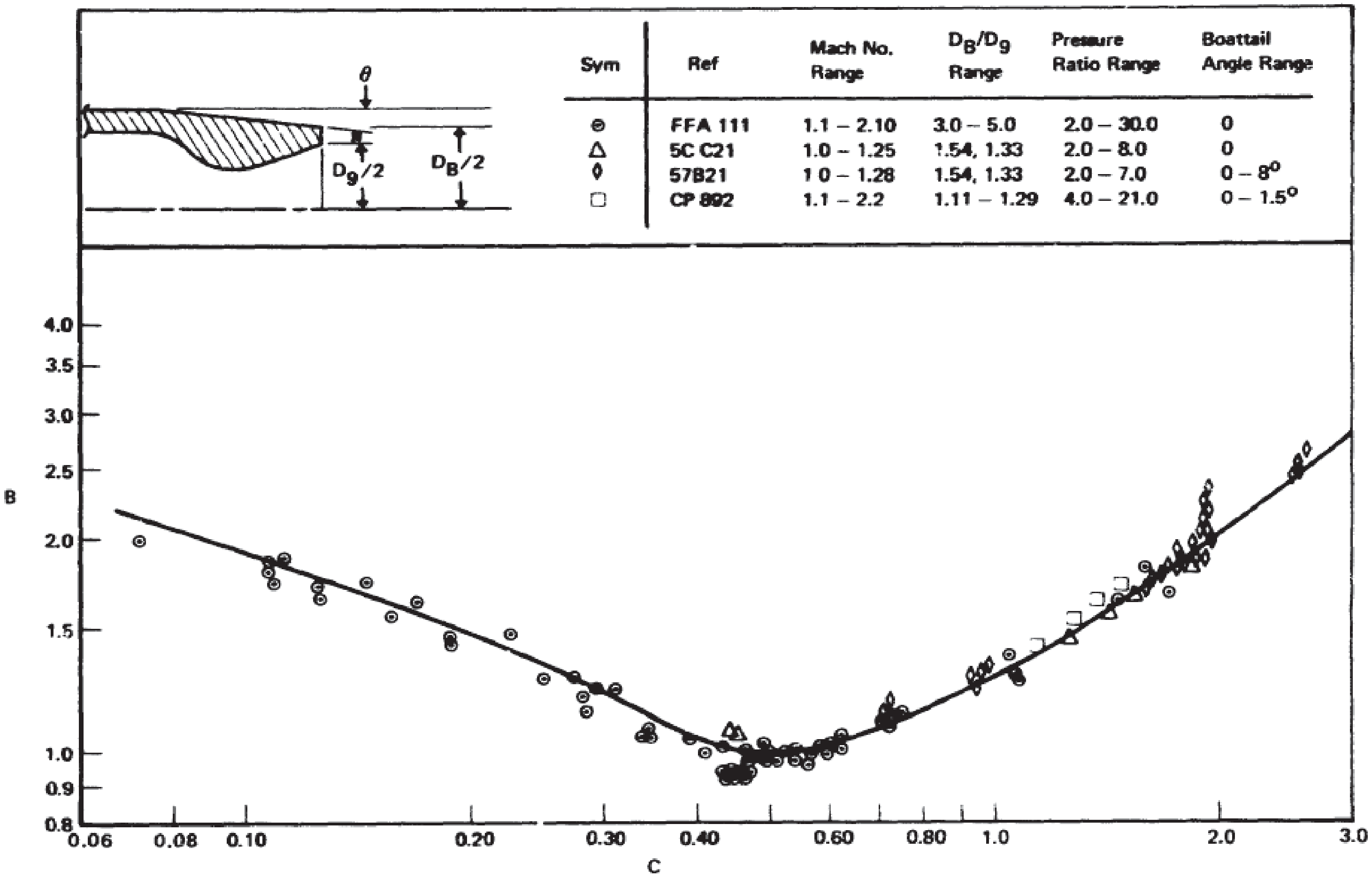

Sym	Ref	Mach No. Range	D_B/D_g Range	Pressure Ratio Range	Boattail Angle Range
⊙	FFA 111	1.1 – 2.10	3.0 – 5.0	2.0 – 30.0	0
Δ	5C C21	1.0 – 1.25	1.54, 1.33	2.0 – 8.0	0
◊	57B21	1 0 – 1.28	1.54, 1.33	2.0 – 7.0	0 – 8°
□	CP 892	1.1 – 2.2	1.11 – 1.29	4.0 – 21.0	0 – 1.5°

APPENDIX H: Ratio of reference base pressures, Ball, W. H. (1972).

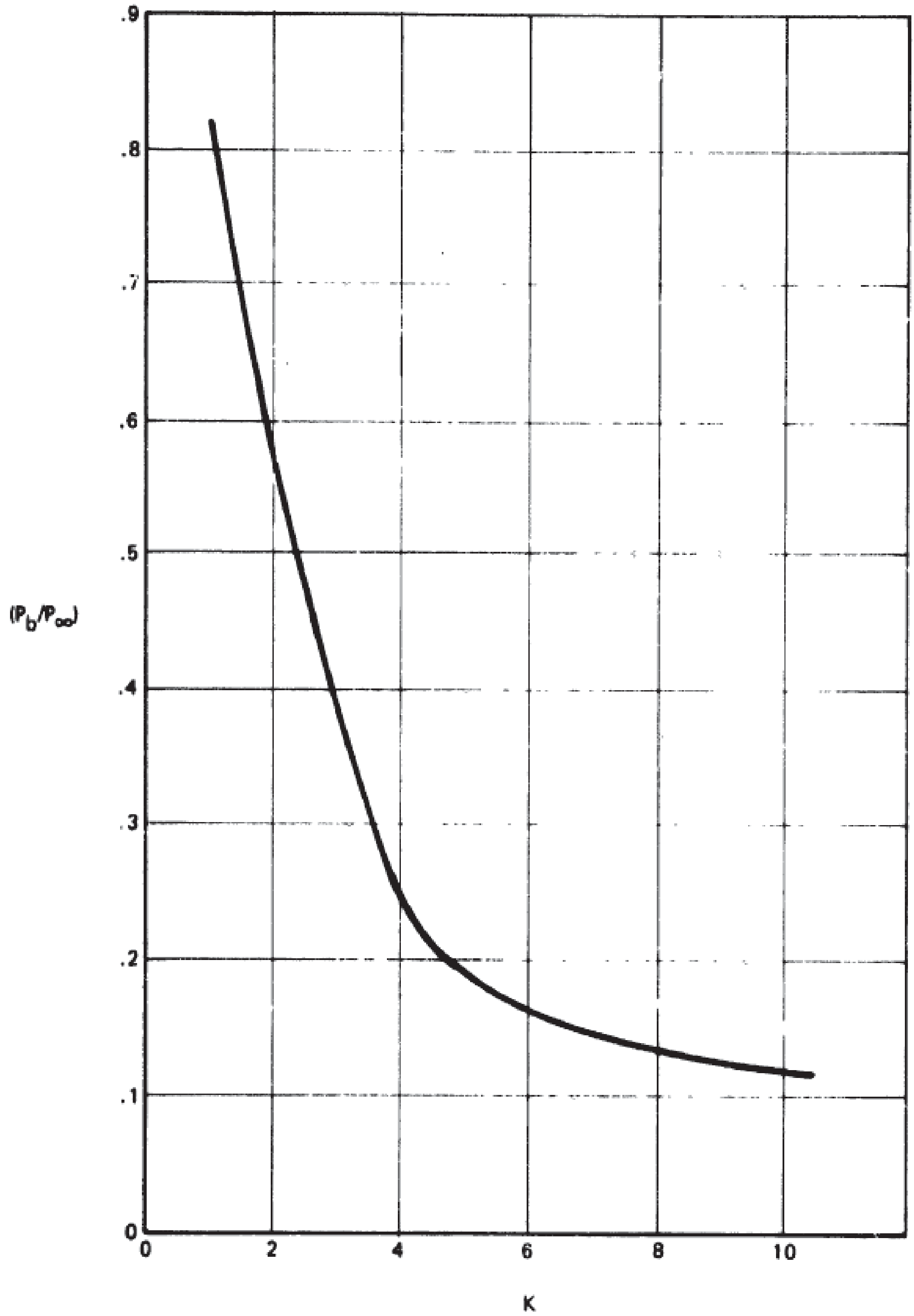

APPENDIX I: Drag coefficient for engine interference, Ball, W. H. (1972).

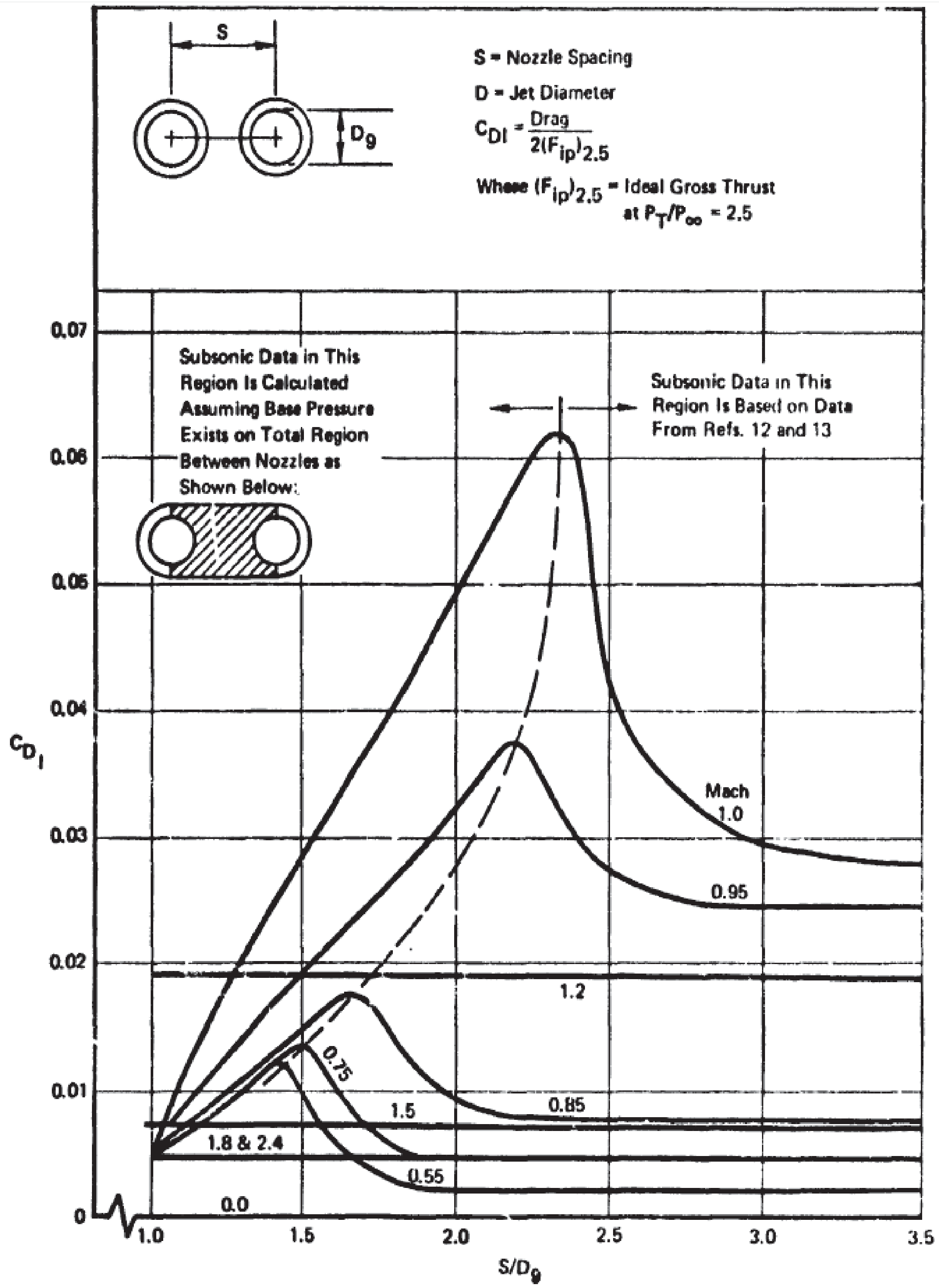

APPENDIX J: Spillage drag coefficient for A0AC ratio, J79 Engine, Ball, W. H. (1972).

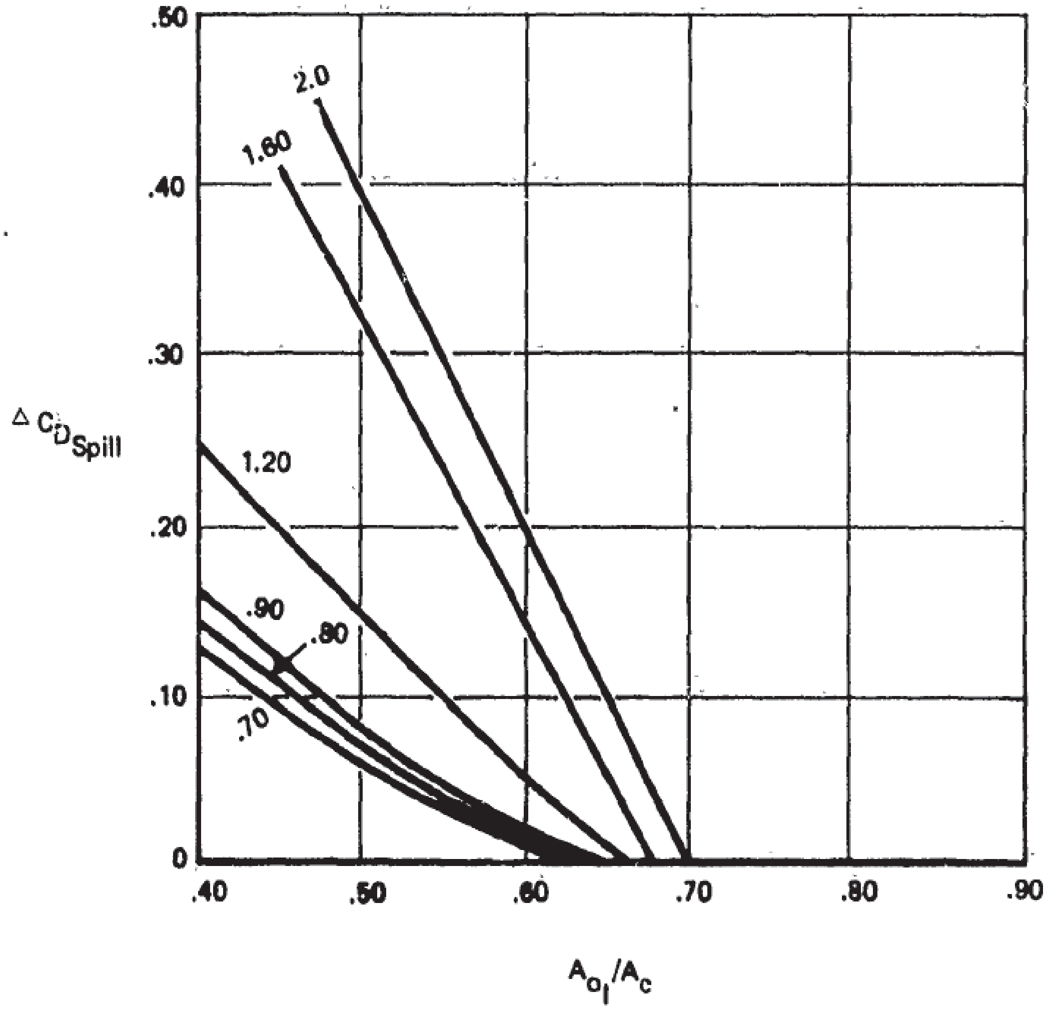

APPENDIX K: Spillage drag coefficient for A0AC ratio, Normal Shock Intake, Ball, W. H. (1972).

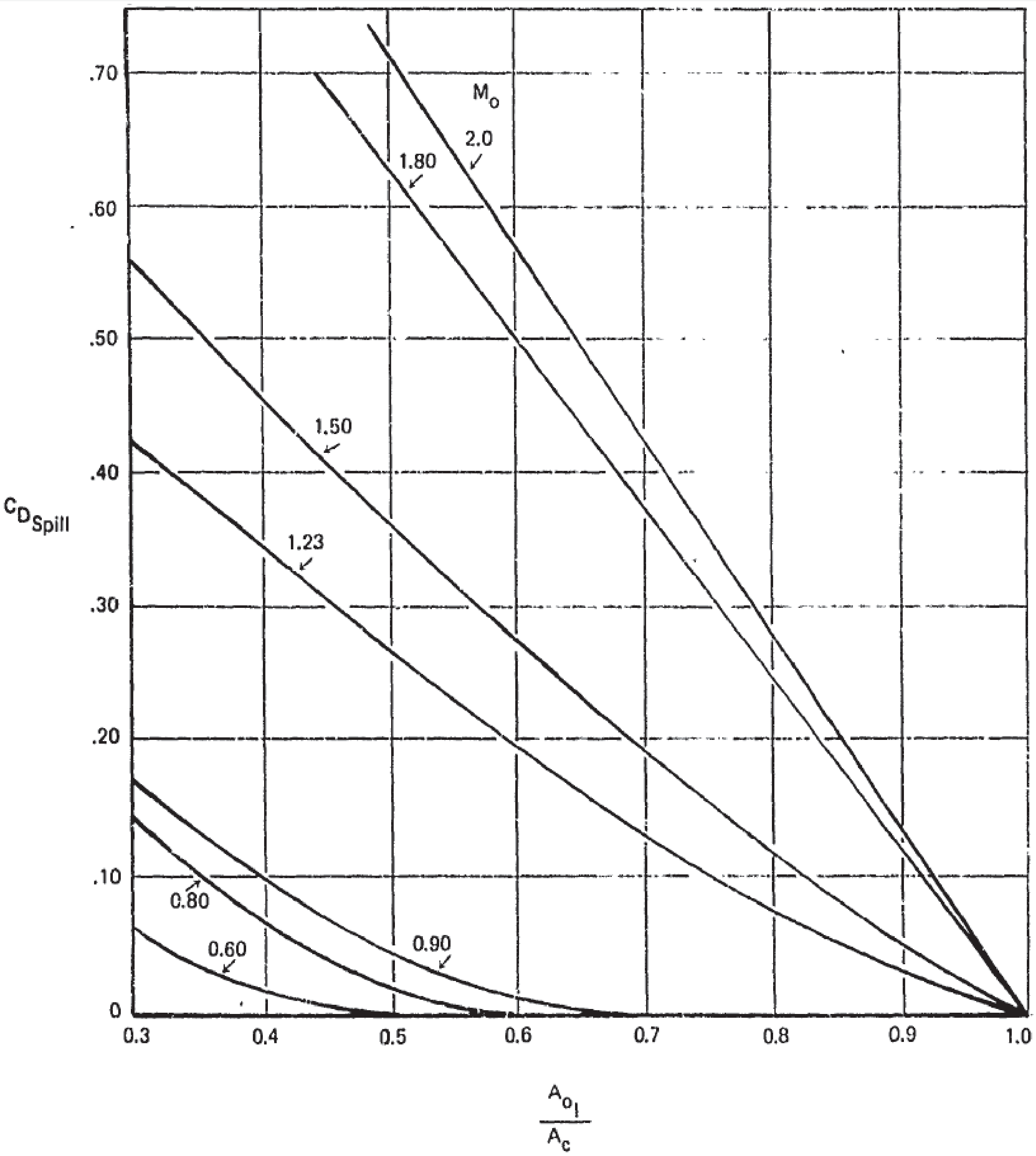

APPENDIX L: Spillage drag coefficient for A0AC ratio, Normal Shock Intake, Ball, W. H. (1972).

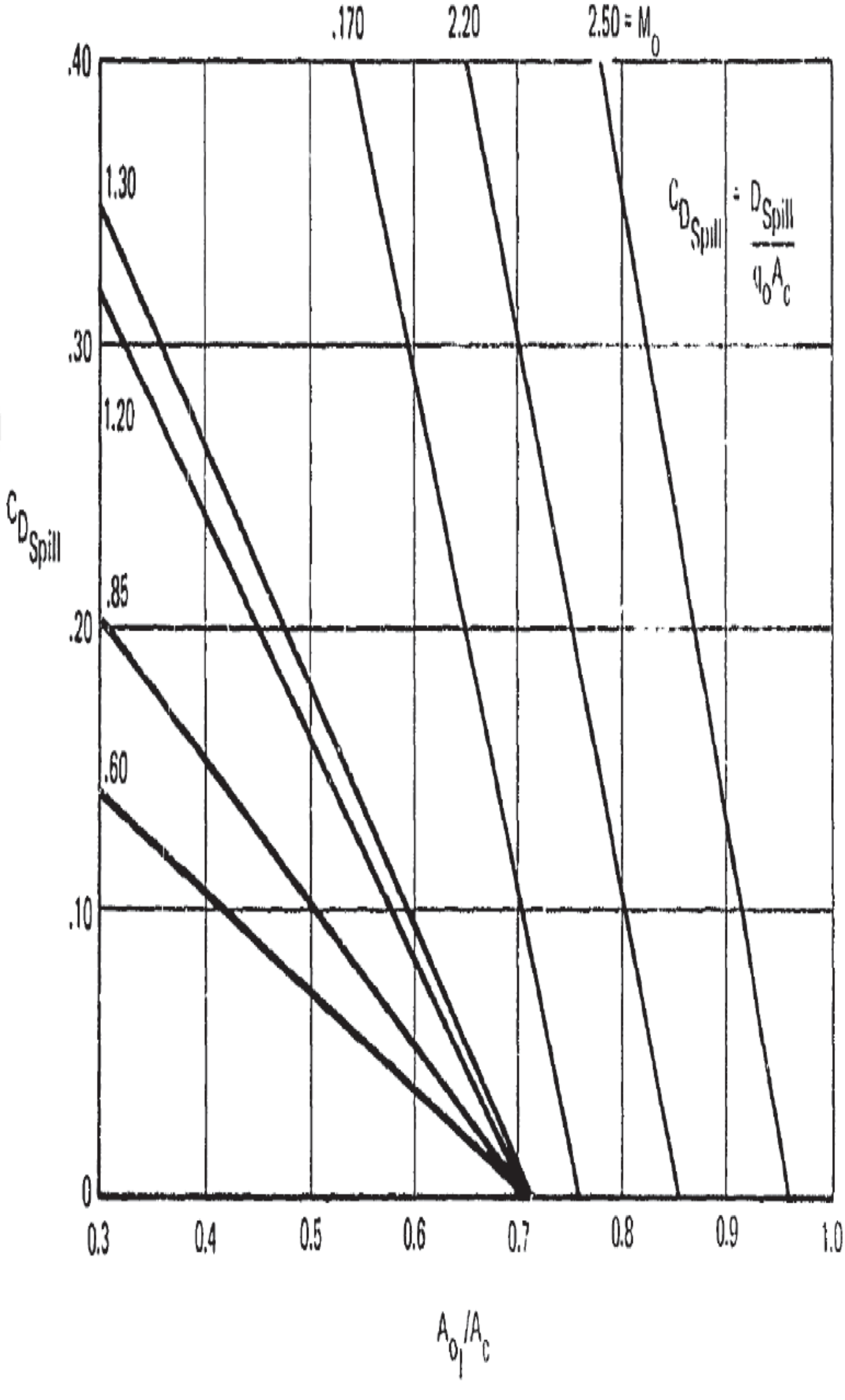

APPENDIX M: Bleed Mass Flow Ratio, External Compression Inlet, Intake, Ball, W. H. (1972).

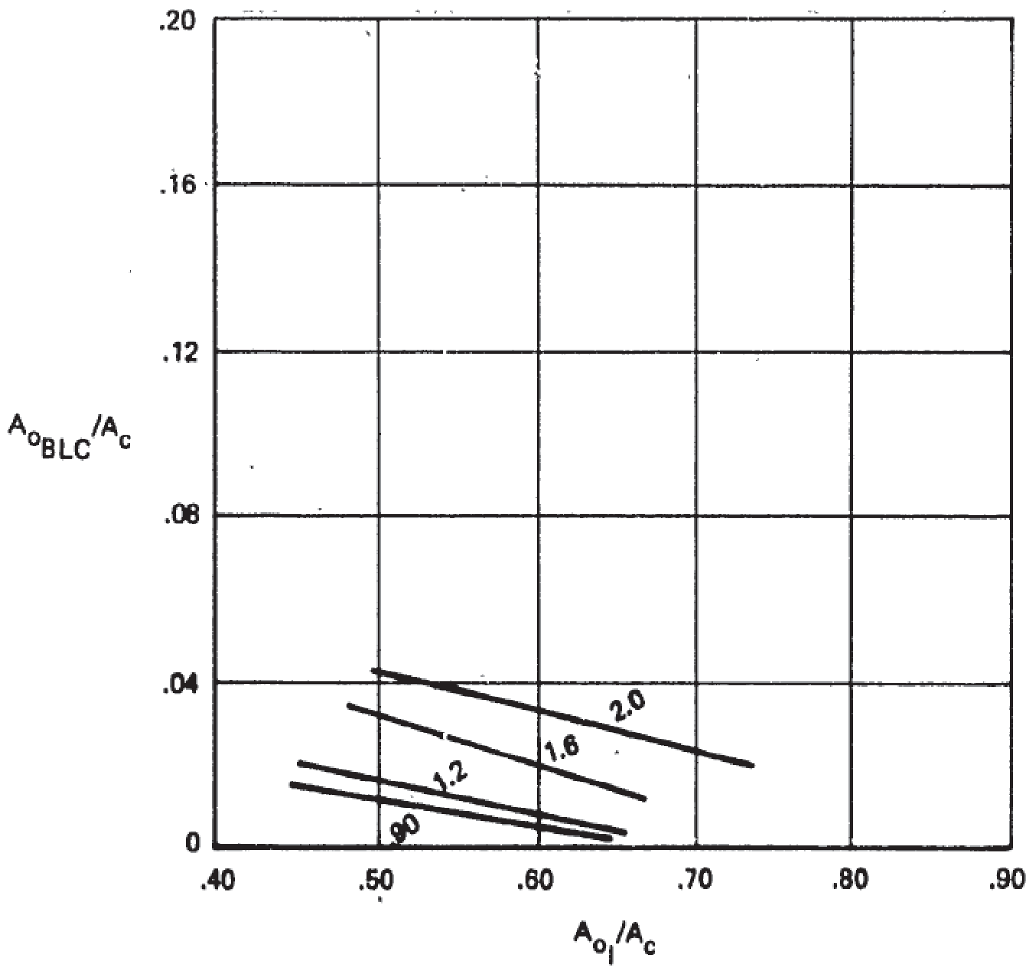

APPENDIX N: Bleed Mass Flow Ratio, J-79 Engine, Intake, Ball, W. H. (1972).

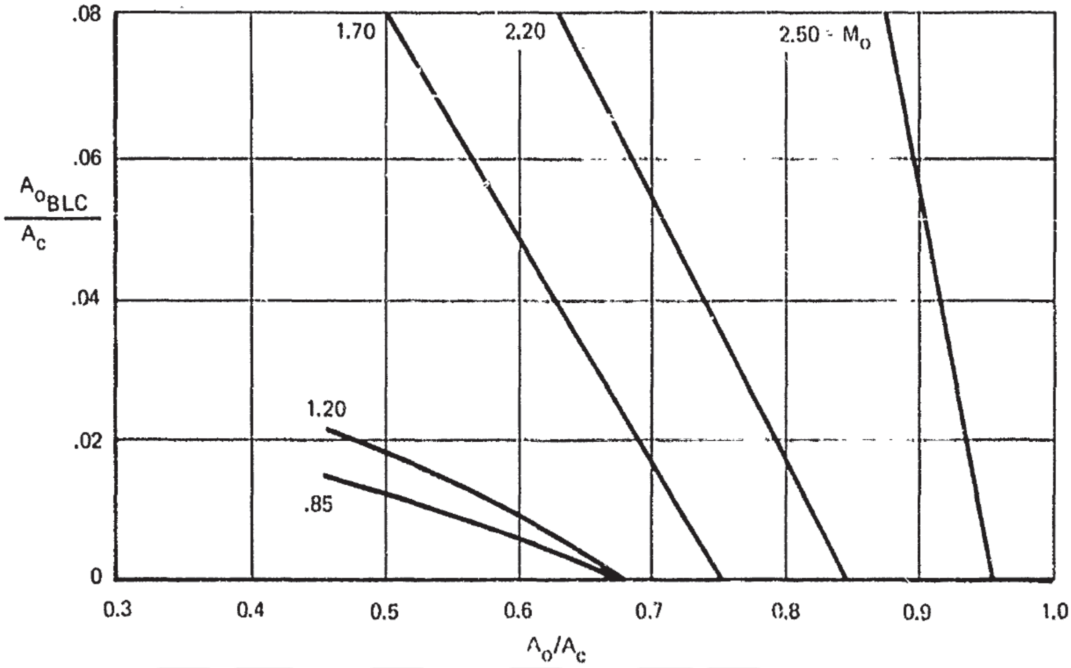

APPENDIX O: F15 Based Drag Assumption

```
def F15_Based_Drag(M, NPR, A9):
   import math
   import pandas as pd
   import scipy as sc
   import numpy as np

#%% Routine for Nozzle Drag Based on F-15 Aircraft

# The routine calculate ratio of drag and free stream
# dynamic pressure as a function of Mach, NPR and A9

#%% Phsical Parameters

# Nozzle Max Diameter, Knuckle Diameter

   dia = 1.180 #m
   area_nozzle = math.pi*dia*dia #nozzle knuckle area
   length_nozzle = 1.2 #m

#%% Limitations

   if A9 <= 0.25 or A9 >= 0.9:
      end

#%% Calculation

   D9 = math.sqrt((4*A9)/math.pi) #Nozzle exit diameter
   bt_angle = math.asin((dia-D9)/(2*length_nozzle))

   if bt_angle <= 0.0 or bt_angle >= 20.0:
      end

   F15_Based_Drag = pd.read_excel(open('nozzle_drag.xlsx','rb'))

   # 1st Col, case number
   # 2st Col, Mach number
   # 3rd Col, NPR
   # 4th Col, bt_angle = 15.86
   # 5th Col, bt_angle = 13.17
   # 6th Col, bt_angle = 9.59
   # 7th Col, bt_angle = 8.28
   # 8th Col, bt_angle = 0.0

   boat = np.array((15.86, 13.17, 9.59, 8.28, 0.0))

   columns = ['#','M', 'NPR', 'DQ1', 'DQ2', 'DQ3', 'DQ4', 'DQ5']
```

```
    DQ = pd.DataFrame(F15_Based_Drag, columns=columns)

    DQ['DQ1'] = sc.interpolate.griddata(F15_Based_Drag(:,2),...
                                         F15_Based_Drag(:,3),F15_Based_Drag(:,
4),Mach,NPR)
    DQ['DQ2'] = sc.interpolate.griddata(F15_Based_Drag(:,2),...
                                         F15_Based_Drag(:,3),F15_Based_Drag(:,
5),Mach,NPR)
    DQ['DQ3'] = sc.interpolate.griddata(F15_Based_Drag(:,2),...
                                         F15_Based_Drag(:,3),F15_Based_Drag(:,
6),Mach,NPR)
    DQ['DQ4'] = sc.interpolate.griddata(F15_Based_Drag(:,2),...
                                         F15_Based_Drag(:,3),F15_Based_Drag(:,
7),Mach,NPR)
    DQ['DQ5'] = sc.interpolate.griddata(F15_Based_Drag(:,2),...
                                         F15_Based_Drag(:,3),F15_Based_Drag(:,
8),Mach,NPR)

    DQ_total = sc.interpolate(boat, DQ,bt_angle)

    return DQ_total, bt_anle
```

APPENDIX P: F15 Based Drag Calculation

```
# -*- coding: utf-8 -*-
import math
import pandas as pd
import scipy as sc
import numpy as np


#%% INPUTS

Wc_max = 145.0 #Maximum Corrected Mass Flow Rate of Engine unit:
kg/s
F119_FanDia = 1045 #Fan Diameter unit: mm

Knuckle_Dia = 1.20 #max, knuckle diameter unit:m
AC = 0.775 # capture area unit: m2

#%% Engine Deck Output

deckoutput = pd.read_excel(open('enginedeck.xslx', 'rb))
Alt = deckoutput(:,1) #altitude unit:ft
MN = deckoutput(:,2) #Mach number
PLA = deckoutput(:,3) #Power Lever Angle
P_amb = deckoutput(:,5) #Ambient Pressure Static unit: kPa
P_amb_t = deckoutput(:,6) #Ambient Pressure Total unit: kPa
T_amb = deckoutput(:,5) #Ambient Temp Static unit: K
T_amb_t = deckoutput(:,6) #Ambient Temp Total unit: K
FG = deckoutput(:,9) #Gross Thrust unit: kN
FN = deckoutput(:,10) #Net Thrust unit: kN
W = deckoutput(:,11) #Air mass flow rate unit: kg/s
Wc = deckoutput(:,12) #Corrected Air mass flow rate unit: kg/s
SFC = deckoutput(:,13) #Specific Fuel Consumption unit: g/(s*kN)
Wfuel = deckoutput(:,14) #Fuel Mass flow rate g/s
A8 = deckoutput(:,32) #Nozzle Throat Area unit: m2
A9 = deckoutput(:,33) #Nozzle Exit Area unit: m2
PqP = deckoutput(:,34) #Pressure Recpvery P2/P0
NPR = deckoutput(:,35) #Nozzle Pressure Ratio

case_number = len(MN) #number of row

#%% Intake and Nozzle Tables
A0AC = pd.read_excel(open('caretintake.xslx', 'rb'), sheetname =
'A0AC' )
percentage = A0AC[2,2:10]
A0AC_MN = A0AC[3:13,1]

A0AC[:,1] = []
```

```
A0AC[1:2,:] = []

#Spill Table
Spill_Table = pd.read_excel(open('caretintake.xslx', 'rb'), sheet
name = 'Spill')
Spill_MN = Spill_Table[1,2:2:28]
Spill_A0AC = Spill_Table[3:13,1:2:27]
cd_spill = Spill_Table[3:13,1:2:28]

#Interpolation
MN_col = np.zeros((154,1))
for i in range(14):
   MN_col[(i-1)*11+1:(i-1)*11,:] = Spill_MN[i]

A0AC_col = np.zeros((154,1))
for i in range(14):
   A0AC_col[(i-1)*11+1:(i-1)*11,:] = Spill_A0AC[i]

cdSpill_col = np.zeros((154,1))
for i in range(14):
   cdSpill_col[(i-1)*11+1:(i-1)*11,:] = cd_spill[i]

G = sc.interpolate.rbf(MN_col,A0AC_col,cdSpill_col) #scattered in
terpolation

A0AC_col = zeros(len(MN),1)
Q0_col = zeros(len(MN),1)
cdSpill_col = zeros(len(MN),1)
Dspill_col = zeros(len(MN),1)
DQ_col = zeros(len(MN),1)
D_nozzle_col = zeros(len(MN),1)
NPF_col = zeros(len(MN),1)
boattail = zeros(len(MN),1)
Ref_Drag = F15_Based_Drag(MN,NPR,A9)

for i in range(case_number):
   A0AC_MN[i] = MN[i]
   A0AC_col[i] = sc.interpolate.rbf(Percentage, A0AC_MN, A0AC,...
                                    Wc[i]/Wc_max,A0AC_MN)

   Q0_col[i] = 0.5*1.4*P_amb[i]*(MN[i]*MN[i])
   Dspill_col[i] = cdSpill_col[i]*AC*Q0_col[i]
   cdnozzle = F15_Based_Drag(MN[i],NPR[i],A9[i])
   DQ_col[i] = cdnozzle[1]
   boattail[i] = cdnozzle[2]
   D_nozzle_col[i] = DQ_col[i]*Q0_col[i]*0.5
   NPF_col[i] = FN[i] - Dspill_col[i] - D_nozzle_col[i]
```

```
#%%Print out Net Propulsive Force and Drag Values

installed_deck = open('installed_engine_deck.txt', 'rb')

for i in range(case_number):
   print(installed_deck, Alt[i], MN[i], PLA[i], FG[i], FN[i], SFC
[i],...
                        Wfuel[i], Wc[i], NPR[i], A8[i], A9[i], NP
F_col[i],...
                        Q0_col[i], cdSpill_col[i], Dspill_col[i],
..
                        boattail[i], DQ_col[i], D_nozzle[i])
```

APPENDIX R: Spill Drag Calculation

```
# -*- coding: utf-8 -*-
import math

#SPILL DRAG CALCULATION

#%% INPUTS
M = 2.0 #Mach number
R_Air = 287.058 #Specific Gas Constant for Air unit: J/(kg*K)
gama = 1.4 #Heat capacity, 1.4 for clean air and 1.33 for burned
air
AC = 0.634 #Capture Area unit: m^2
Pamb = 23295 #Ambient Pressure unit: Pa
Pt = 101325 #Total Pressure unit: Pa
Tt = 288.15 #Total Temperature unit: K
PqP = 0.905 #Pressure Recovery P2/P0
W2_corr = 63.41 #Corrected air mass flow rate at engine face unit
: kg/s

#%% CALCULATION
QD = 0.5*Pamb*M**2
isent_coe = math.sqrt(gama/(1+(((gama-
1)/2)*(M)^2))**((gama+1)/(gama-1)))
A0 = ((math.sqrt(R_Air*Tt)*W2_corr)/((M)*Pt*isent_coe))*PqP
A0AC = A0/AC

A0BLCAC = 0.1 #Bleed Mass Flow and Area APPENDIX K-L or M
according to intake type

A0IAC = A0AC + A0BLCAC

cd_spill = 0.1 # Get data from APPENDI I or APPENDIX J
norm_cd = 0
extra_cd = 0

cd_spill_tot = cd_spill + norm_cd + extra_cd
Fspill = cd_spill_tot * QD * AC
```

APPENDIX S: Boattail Drag Calculation

```
# -*- coding: utf-8 -*-
import math

#BOATTAIL DRAG CALCULATION
#%% INPUTS
M = 0.6 #Mach number
D_knuckle = 1.200 #Knuckle diameter, max diameter unit:m
L_nozzle = 0.8 #Nozzle axial length, unit:m
s = 1.25 #Engine spacing unit:m

A8 = 0.45 #nozzle throat area, unit: m2
A9 = 0.62 #nozzle exit area, unit: m2

Pamb = 57182 #Ambient Pressure unit:Pa
NPR = 3.2 #Nozzle Pressure Ratio
base_area = 1.1 #Nozzle Base Area unit:m2
QD = 0.5* Pamb * M**2 #Dynamic Pressyre unit: Pa


A_knuckle = ((D_knuckle**2) * math.pi())/4
D9 = math.sqrt(4*A9 / math.pi())

bt_angle = (math.atan((D_knuckle-D9)/(2*L_nozzle)))*180/math.pi()

#Subsonic Case
Cd_bt_z = 0.1 #Zero flow base pressure vs diameter ratio
bt_grad = 0.02 #Rate of change of boat-
tail drag with base pressure-bottail ang
grad = 4 #Gradient of base-pressure increment
zero_jet = 0.5 #Gradient of base-pressure increment vs jet-
diameter ratio

Cp_diff = grad*((D9**2)/(base_area*D_knuckle)) #0.1 base thicknes
s
F_boattail = Cp_diff*QD*A_knuckle
```

APPENDIX T: Interference Drag Calculation

```
# -*- coding: utf-8 -*-
import math

#INTERFRENCE DRAG CALCULATION

M = 1.4
D_knuckle = 1.2 #Knuckle diameter, max diameter unit:m
s = 1.25 # engine spacing
A8 = 0.40 #Nozzle throat area #m2
A9 = 0.62 #Nozzle exit area #m2

Pamb = 23295 #Ambient Pressure unit:Pa
number_engine = 2 #number of engines
QD = 0.5* Pamb * M**2 #Dynamic Pressyre unit: Pa

A_knuckle = (math.pi()*D_knuckle**2)/4 #maximum area, knuckle are
a
D9 = math.sqrt(((4*D_knuckle)/math.pi)) # nozzle exit diameter un
it:m
sd_ratio = s/D9

data = 0.2 #cd interference data APPENDIX H
F_interfrence = (data*A8*Pamb*4.34)/((number_engine-
1)/(number_engine)
cd_interfrence = F_interfrence/(QD*A_knuckle)
```